HOW DOES COUPLED TROPOSPHERIC CHEMISTRY AFFECT CLIMATE? AN INVESTIGATION USING THE COMMUNITY EARTH SYSTEM MODEL VERSION 2

NOAH ALEXANDER STANTON

A DISSERTATION SUBMITTED TO

THE FACULTY OF GRADUATE STUDIES

IN PARTIAL FULFILMENT OF THE REQUIREMENTS

FOR THE DEGREE OF

MASTER'S OF SCIENCE

GRADUATE PROGRAM IN EARTH AND SPACE SCIENCES AND

ENGINEERING

YORK UNIVERSITY

TORONTO, ONTARIO

July 2022

Abstract

The depiction of tropospheric chemistry in climate models has greatly improved in recent years. The Community Earth System Model version 2 with Whole Atmosphere Community Climate Model version 6 (CESM2-WACCM6) has implemented fully-coupled tropospheric chemistry with 231 chemical species, an updated aerosol scheme, as well as a fully-coupled ocean. In addition to their effects on the chemical composition of the troposphere and stratosphere, these model improvements also affect climatological parameters like cloud radiative effect (CRE), surface temperature and sea level pressure. To further examine these impacts, 100-year preindustrial control simulations were run using the following two configurations 1) a "simplified" CESM2-WACCM6 configuration in which coupled chemistry is confined to the middle atmosphere, and 2) the standard CESM2-WACCM6 configuration with fully-coupled chemistry over all atmospheric levels. Differences of climatological mean parameters between the model configurations were analyzed. Regional differences in surface temperature and the CRE range between -5 K and 5 K and -10 W m^{-2} to 10 W m^{-2}, respectively. There are also significant differences in the number concentration of

ozone. Compared to the simplified CESM2-WACCM6 configuration, the standard CESM2-WACCM6 produces 1.5×10^{17} to 3.0×10^{17} molecules m^{-3} more ozone in the upper troposphere, an increase of 10-20%. The standard CESM2-WACCM6 also produces 1.5×10^{17} molecules m^{-3} (3%) more ozone in the southern polar stratosphere compared to simplified CESM2-WACCM6. These ozone changes do not appear to drive dynamical changes, rather they appear to be driven by dynamical changes that extend up from the troposphere. These dynamical changes include an equatorward shift of the mid-latitude jets and weakening of the Southern Hemisphere stratospheric polar vortex. The equatorward shifts of the jets are due to widespread tropospheric cooling which is partially due to increases in NOy, a component of which is organic nitrate. Decreases in the troposphere of primary organic matter aerosol (POM) and black carbon (BC), about -30% to -80% and -20% to -60% respectively, also contribute to tropospheric cooling. These changes in turn influence cloud distribution, precipitation patterns, and sea ice area.

Dedication and Acknowledgements

Dedication

I dedicate this work to my Oma. I was scared of all weather when I was young. I would not get out of the car at the beach if there was even just a small cumulus cloud. During one thunderstorm, my Oma placed a chair in front of our screen door and just stared out into the torrent. I could not understand why someone would do this, and asked her why she wasn't scared. She said, "It's beautiful Noah! Don't be afraid of it, enjoy it.". I kept those words with me ever since and it grew into a true love of working to understand weather and climate. I also dedicate this to my Opa, who at least recognized thunder was a little scary.

I also dedicate this to my parents, who have always pushed me to keep going with my educational pursuits. At their dinner parties, they'd allow me to warn their friends of the incoming Nor'easter or severe thunderstorm warning. They have always known to foster that interest, and I truly thank them for providing me an outlet to express this interest. I also dedicate this to my two sisters, Emma and Anna. They

have had to bare with many geek outs over winter storms.

Finally I dedicate this to my true love, Selina. She has been a constant support throughout my education, and pushed me to work harder. Her drive to be her best self has inspired me to keep pushing in my academic goals. I sincerely think that this process would be a lot harder without her, and she deserves many thanks.

Acknowledgements

I would like to sincerely thank all of the staff at York University, who have guided me in my academic journey. Jim Whiteway for providing me an opportunity to work with lasers. I got to combine two of my favourite passions, shooting lasers and observing weather! I also would like to thank John Moores for giving me a wonderful chance to view Earth from a different perspective with the DSCOVR satellite data. I also want to acknowledge the rest of the ESSE faculty who have been a part of my journey as a Bachelor's student and a Master's student.

A special acknowledgement is given to Rob McLaren who served on my supervisory committee. Rob provided helpful feedback throughout the synthesis of this research. The knowledge provided in the classes I took with Rob were invaluable in this research.

I thank Cora Young and Yongsheng Chen for serving on my thesis exam committee. Their feedback was crucial on how to best design my future research questions.

A massive thank you is also given to Neil Tandon, my supervisor. Since I started talking to Neil about my project he has always inspired me to keep working towards the pursuit of science. From starting up the climate model, to helping teach students, teaching me, and providing support during the thesis writing process, Neil has been a vital part of this project. I sincerely thank you again for your dedication to teaching and research!

I also want to thank my research group who has always been a big support throughout my project. You have been helpful with feedback and motivation. Jamie, Anas, Thabo, and Dev, thank you all! I do have to give a special thanks to Jamie in particular, who sat in on meetings and helped me bounce ideas around during this research.

I must also acknowledge the compute support given by the Digital Research Alliance of Canada (formerly Compute Canada). Compute time on their systems has been invaluable for this research.

The Community Earth System Model (CESM) project at NCAR has also been integral for this research, as it is the main tool used in this analysis. The CESM project is supported primarily by the National Science Foundation. I thank all the scientists, software engineers, and administrators who contributed to the development of CESM2.

I also acknowledge the support given by NSERC.

Contents

List of Figures

1 Introduction

1.1 History and Development of Climate Models

Weather and Climate models have been advancing exponentially throughout the 20th and 21st centuries with advances in computation. The first long-term numerical forecast was performed in 1956 with a two-layer quasi-geostrophic model, on just 5 Kb of memory and 10 Kb of external storage (Phillips, 1956). In 1969, Manabe et al. (1969) created the first "coupled" atmospheric-ocean general circulation model (GCM). This model simplified the Earth into three sections, equal parts ocean and land, and took 1100 hours for one integration period. The first climate model with a coupled atmosphere-ocean on realistic topography occurred in 1975, with about 300 years of output from 50 days of compute time (Manabe et al., 1975). The National Center for Atmospheric Research (NCAR) started the Community Climate Model (CCM) initiative in 1983, with the goal of providing an open-source climate model to researchers. NCAR recognized that climate models were becoming ever more specialized and required the expertise of scientists across multiple domains. By

1995, scientists were able to model the radiative forcing of sulfate aerosols compared to increased greenhouse gases (GHGs) and concluded that GHG forcing began to dominate over the sulfate aerosol forcing (Mitchell et al., 1995). In 2013, the Community Earth System Model (CESM) framework was laid out by NCAR to extend the previously mentioned CCM framework. CESM looked to model the whole Earth system by including biogeochemical cycles, atmospheric chemistry, the Greenland Ice sheet, and a number of other processes (Hurrell et al., 2013). The modularity and community-based approach of CESM, along with its extensive documentation and support, is why it was chosen for this research.

1.2 The Temperature Tendency Equation

The temperature tendency equation can be expressed with the following equation:

$$\left(\frac{\partial T}{\partial t}\right)_p = -u\frac{\partial T}{\partial x} - v\frac{\partial T}{\partial y} - \frac{\omega T}{\theta}\frac{\partial \theta}{\partial p} + Q \tag{1.1}$$

with Q being defined as the diabatic heating rate, T as temperature (K), p as pressure, potential temperature defined as $\theta = T(\frac{p_o}{p})^{(\frac{R}{C_p})}$, with R being the ideal gas constant and C_p being specfic heat capacity, and u & v defined as the East-West and North-South winds, respectively. Pressure velocity in vertical coordinates is $\omega = \frac{dp}{dt}$ (Kasahara, 1974). Performing the differentiation of $\frac{\partial \theta}{\partial p}$ eq. 1.1 becomes:

$$\underbrace{\left(\frac{\partial T}{\partial t}\right)_p}_{\text{temp. tendency}} = \underbrace{-u\frac{\partial T}{\partial x} - v\frac{\partial T}{\partial y}}_{\text{hor. advection}} \underbrace{-\omega\left(\frac{\partial T}{\partial p} - \frac{RT}{C_p p}\right)}_{\text{vert. advection}} + \underbrace{Q}_{\text{diabatic heating}} \tag{1.2}$$

The LHS represents the total temperature tendency. The first two terms on the RHS represent the temperature tendency due to horizontal advection. The third term on the RHS represents the temperature tendency due to vertical advection. The last term on the RHS is the temperature tendency due to diabatic heating. The advection terms can be considered the dynamical influence on temperature tendency. The diabatic heating term captures latent heating, conduction, and radiative temperature tendency (Holton, 2013).

1.3 Thermal Wind Balance

The geostrophic balance can be defined as the balance between the Coriolis force ($fV \equiv 2\overrightarrow{\Omega} \times \overrightarrow{V}$) and the pressure gradient force per unit mass ($-\frac{1}{\rho}\nabla p$), with ρ being density. These two terms relatively balance each other and we can approximate their balance in the geostrophic relationship:

$$fv \approx \frac{1}{\rho}\frac{\partial p}{\partial x}; \qquad fu \approx -\frac{1}{\rho}\frac{\partial p}{\partial y} \tag{1.3}$$

The geostrophic balance is considered a diagnostic equation as it cannot tell us about the time evolution of the velocity field, but rather in large-scale extratropical systems

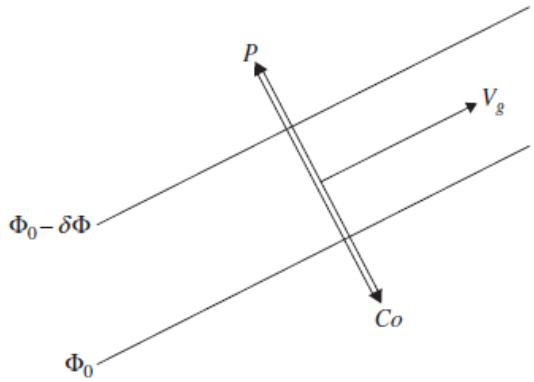

.

Figure 1.1: The geostrophic balance between the Coriolis force (C_o) and the pressure gradient force (p). (Φ_0) is a geopotential surface. (V_g) is the geostrophic wind (Holton, 2013)

it provides a connection between the pressure field and horizontal velocity. Figure 1.1 shows how the geostrophic balance results in geostrophic flow that is parallel to pressure surfaces (Holton, 2013).

In a system with a horizontal temperature gradient, the geostrophic wind will have vertical shear. Figure 1.2 shows how this vertical shear arises due to the sloping of isobaric surfaces, with respect to the x-axis. The thickness between two isobaric layers is proportional to the mean temperature of the layer. Warmer temperatures increase the thickness of a layer, while colder temperatures decrease the thickness of a layer. The thermal wind term is somewhat misleading as it is not a wind, but rather a description of the vertical shear in geostrophic wind caused by a temperature gradient. To derive the thermal wind equation it is easiest to define the geostrophic balance in isobaric coordinates:

$$v_g = \frac{1}{f}\frac{\partial \Phi}{\partial x} \qquad u_g = -\frac{1}{f}\frac{\partial \Phi}{\partial y} \tag{1.4}$$

Φ is the geopotential height, and g is the acceleration due to gravity. The hydrostatic equation can be modified by the ideal gas law as:

$$g\frac{\partial z}{\partial p} = \frac{\partial \Phi}{\partial p} = -\alpha = -\frac{RT}{p} \tag{1.5}$$

α is defined as the specific volume $\frac{V}{m}$, with V being volume and m being mass. Applying the hydrostatic equation and differentiating eq. 1.4 with respect to pressure we get the thermal wind equation (in vector form):

$$\frac{\partial \overrightarrow{V_g}}{\partial \ln p} = -\frac{R}{f}\overrightarrow{k} \times \nabla_p T \tag{1.6}$$

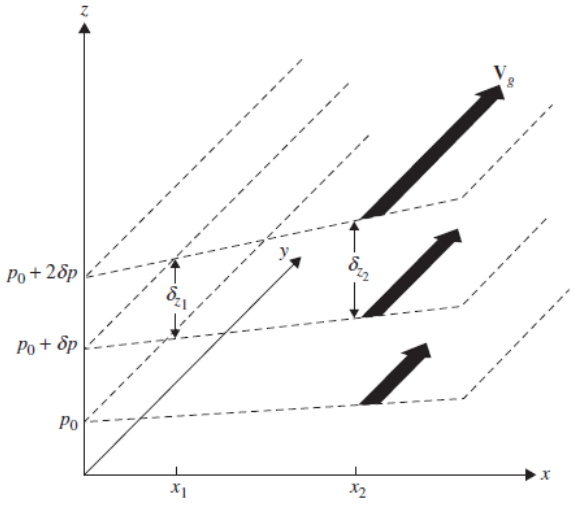

.

Figure 1.2: The relationship between vertical shear, horizontal temperature gradient, and geostrophic wind (Holton, 2013)

Integrating the hydrostatic equation vertically from p_0 to p_1 and substituting T with mean T of a layer, the result is the hypsometric equation:

$$\Phi_1 - \Phi_0 \equiv gZ_T = R\langle T\rangle \ln \frac{p_0}{p_1} \tag{1.7}$$

Z_T is the thickness between the layers p_0 and p_1 in geopotential meters. This indicates that the isolines of thickness are the same as the isotherms of mean temperature. Then eq. 1.6 can be re-written by integration:

$$\vec{V}_T = \frac{R}{f}\vec{k} \times \nabla\langle T\rangle ln\frac{p_0}{p_1} \tag{1.8}$$

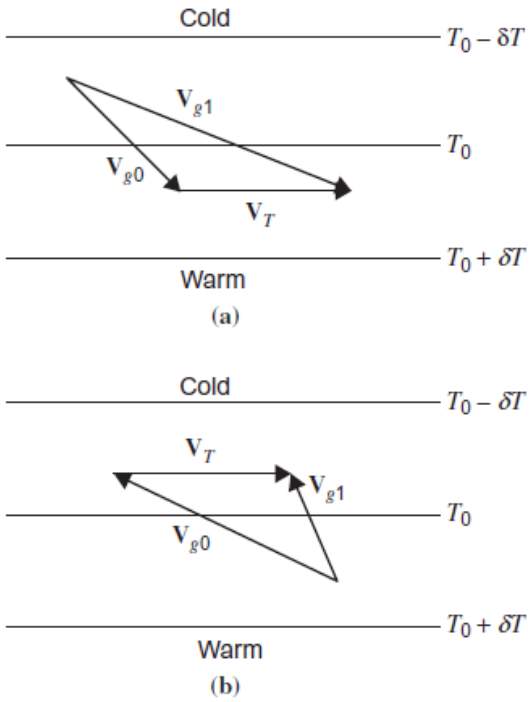

Figure 1.3: Relationship between turning of geostrophic wind and temperature advection in the Northern Hemisphere: (a) backing of wind with height - cold advection (b) veering of wind with height - warm advection (Holton, 2013).

Fig. 1.3 shows the predictive ability of the thermal wind equation. The following relationships are defined for the Northern Hemisphere. Fig 1.3a shows when winds are backing (counterclockwise rotation of winds with height), and indicates cold advection is occurring. Fig. 1.3b shows when winds are veering (clockwise rotation of winds with height), and indicates warm advection is occurring. The opposite relationship occurs in the Southern Hemisphere. This relationship allows for a reasonable estimate of temperature advection which can be assessed from radiosonde data (Holton, 2013).

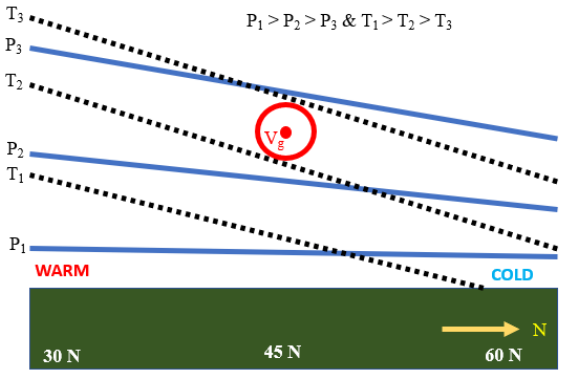

Figure 1.4: This figure shows the thermal wind relationship with isotherms and isobars. The blue lines represent isobars, while the dotted black lines indicate the isotherms. V_g is the geostrophic wind, and it is coming out of the page.

Fig. 1.4 shows the thermal wind with isotherms. The magnitude of V_g in the upper level is dependent on the gradient in temperature. If there is a stronger temperature gradient from the sub-tropics to the mid and upper latitudes $|V_g|$ will become stronger. Conversely, if a weaker temperature gradient exists from the sub-

tropics to the mid and upper latitudes $|V_g|$ will become weaker.

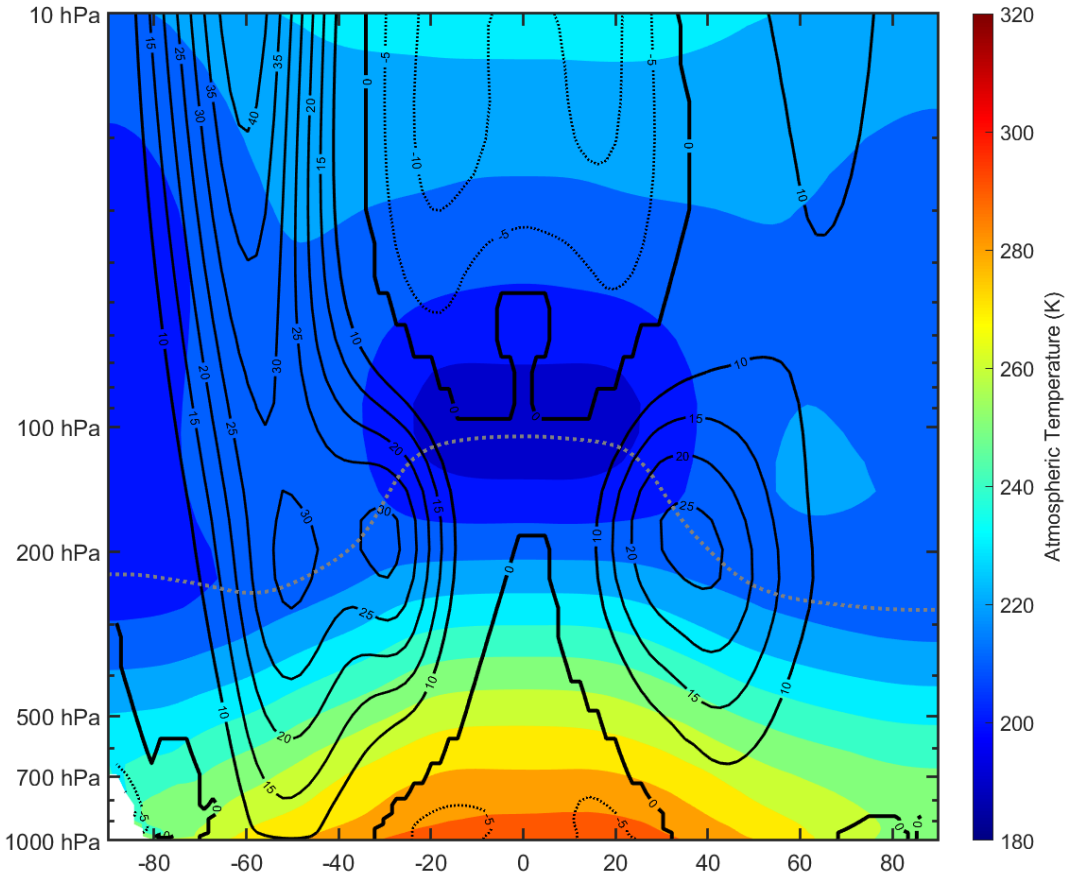

Figure 1.5: This figure shows how the meridional temperature gradient in the atmosphere results in mid-latitude and subtropical jets. The black lines represent zonal wind (m s^{-1}), while the coloured contours are atmospheric temperature (K).

Figure 1.5 shows the zonal average (100-yrs) of temperature and zonal wind for the simplified CESM2-WACCM6 climate model case. These two quantities were overlaid as they are intimately connected. As mentioned above, the strength of the meridional temperature gradient is what determines the magnitude of the geostrophic

wind. Fig. 1.5 shows the typical locations of the max magnitude in geostrophic wind, often called the jet streams. The max jet speeds are located at about 40°N, 30°S, and 55°S. These jets move depending on the season, but on average are located by the tropopause in these latitude bands. The gradient of temperature is somewhat uniform throughout most of the tropics until these latitude bands. From here to the poles, the meridional temperature gradient steepens significantly leading to the structure of jets present in fig. 1.5.

1.4 Global Precipitation Pattern Due to General Circulation

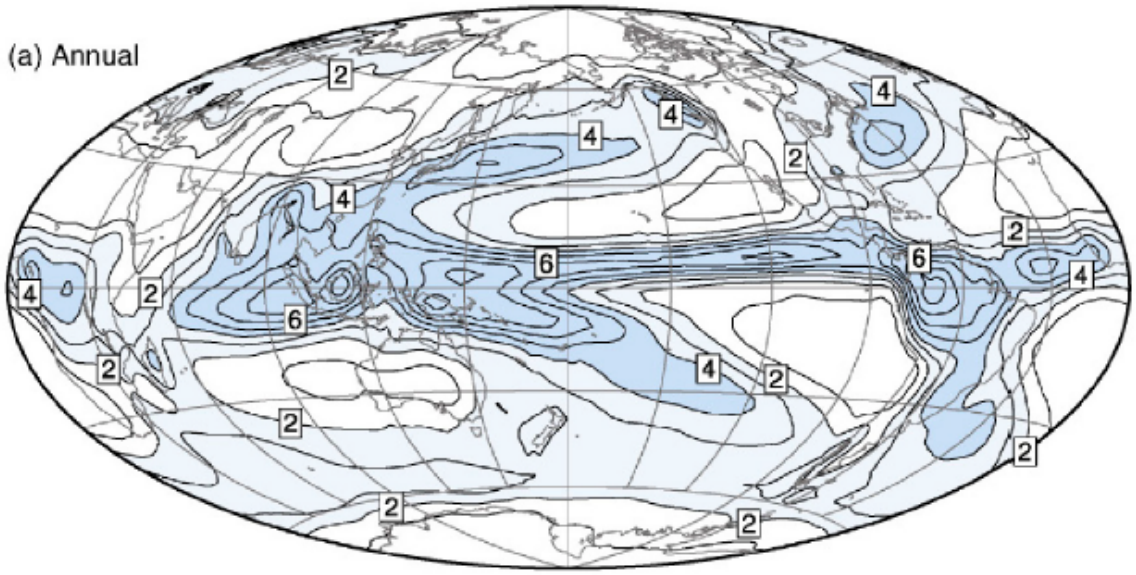

Figure 1.6: This figure shows the annual global precipitation pattern in mm day^{-1} (Hartmann, 2015).

Figure 1.6 shows the annual global precipitation pattern. The area with the most global precipitation is located near the equator in the Intertropical Convergence Zone (ITCZ). It is in this near equatorial latitude band where there is the convergence of the NH's and SH's Hadley Cells. This circulation structure is what drives most convection in the tropics. Precipitation decreases significantly approaching the poles due to the temperature dependence on the saturation vapour pressure. As the temperature gets colder towards the poles, the air cannot hold as much moisture.

The other pattern that is seen are the bands of low precipitation at 30°N and 30°S. These occur due to the descending branch of the Hadley cell and Ferrel cell. The moist air rising from the ITCZ is pushed poleward in the upper troposphere where it cools and dries out. Eventually, around the 30° mark in both hemispheres, this air begins to sink and warms adiabatically. This results in reduced precipitation for these regions, known as the subtropical dry bands. Both the ITCZ and these dry bands have seasonality associated with them.

Figure 1.7 shows the mean meridional mass stream function of Earth. This quantity can roughly show the latitude-pressure structure of Earth's circulation. The arrows on the figure show the direction of circulation around each cell. There is clockwise motion around red contours, and counter-clockwise motion around blue contours. In this figure the nearly 3-cell structure of general circulation is clearly visible. Rising motion in the ITCZ, near the equator is seen in fig. 1.7c. The descending motion in the subtropical dry latitude bands are also seen roughly around

30°N and

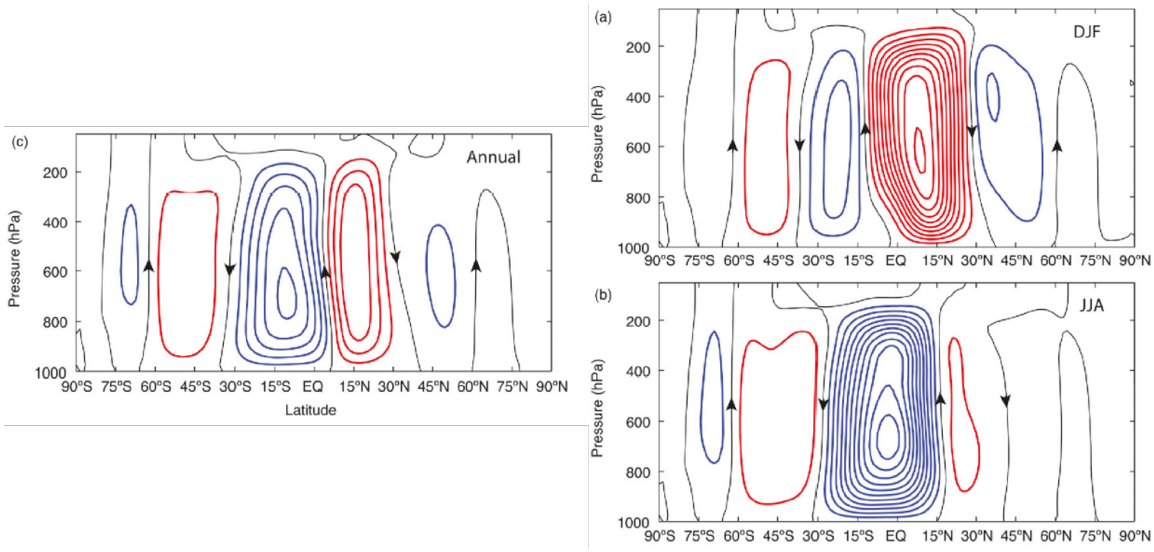

Figure 1.7: This figure shows the zonal cross-section of mean meridional mass stream function. a) DJF b) JJA c) Annual mean. The contour interval is 2×10^{10} kg s^{-1} (Hartmann, 2015).

30°S. Please note how the ITCZ and the subtropical bands shifts north during the NH summer (JJA fig. 1.7b) and south during the NH winter (DJF fig. 1.7a). Any changes to general circulation will result in a change in the mean meridional mass stream function, and therefore could modify where the ITCZ and subtropical dry bands are located (Hartmann, 2015).

1.5 Earth's Energy Balance

The vertical flux of energy from the sun to the surface is the one of the key parameters influencing Earth's climate. At the top of the atmosphere 100 W m^{-2} of shortwave is reflected back out to space, 75 W m^{-2} from clouds, aerosol, and gaseous

species in the atmosphere, along with another 25 W m^{-2} from the surface.

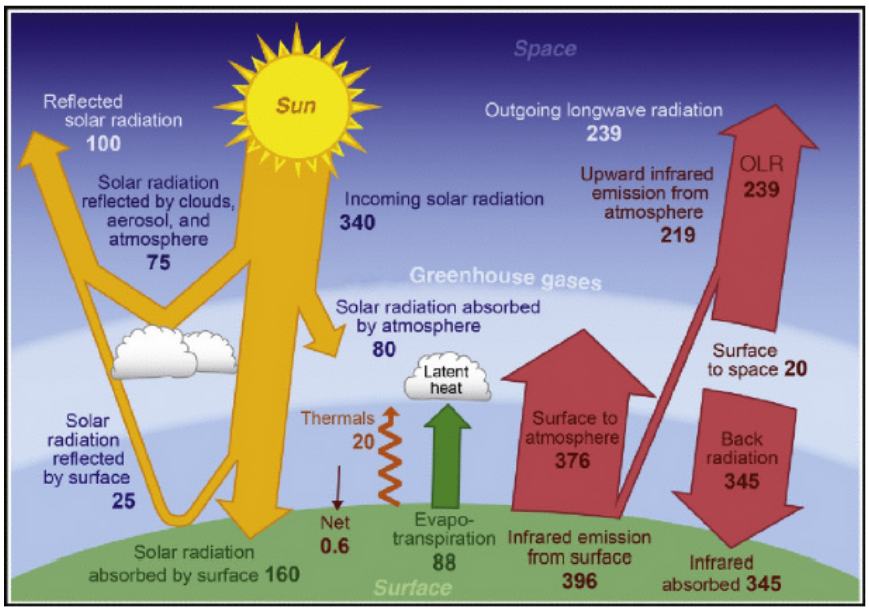

Figure 1.8: This figure shows the global radiative energy balance. Units are in Wm^{-2} (Hartmann, 2015).

The remaining shortwave solar radiation attenuates through the atmosphere, with some absorption due to the ozone layer, water vapour, and other constituents. About 80 W m^{-2} of shortwave is absorbed in the atmosphere. Still, a significant amount (340 - 180 W m^{-2}) = 160 W m^{-2}) of the shortwave radiation reaches the surface and is absorbed. The shortwave absorbed by the surface is then re-emitted as longwave radiation back out towards the atmosphere and space. However, the Earth's atmosphere is not nearly as transparent to longwave radiation as it is to shortwave radiation. This mainly is due to the greenhouse gases (GHGs) present in the atmosphere, with the major GHGs being H_2O, CO_2, CH_4, and N_2O. These GHGs absorb some of the outgoing longwave from the surface, and re-emit it back to the

Earth's surface.

Fig. 1.8 summarizes the total global radiative energy balance. The net energy balance at the top of the atmosphere is calculated as: Incoming solar (340 W m^{-2}) - Reflected solar (100 W m^{-2}) - Emitted terrestrial radiation (239 W m^{-2}) = Storage (0.6 W m^{-2}). The 0.6 W m^{-2} net energy is stored in the oceans, which are beginning to warm up due to human induced climate change (Hartmann, 2015). It can be seen that clouds, aerosols, and the atmosphere reflect about 75 W m^{-2} of incoming shortwave radiation back out to space. This suggests that any increases/decreases to aerosols and clouds has a significant impact on the amount of reflected solar radiation (Hartmann, 2015).

Any changes in aerosols and clouds will have a large impact on the reflected solar component of this energy balance. If there is a large influx of volcanic aerosols, for example, there is an increase in the reflected solar radiation. This reduces surface temperature. Conversely, increases in GHGs (like CO_2), will increase the trapped longwave radiation which results in an increase in the storage component of this balance. Most of the storage terms energy is absorbed in the oceans, this is why with human caused climate change the oceans are storing about 90 % of excess energy (Rhein et al., 2017).

1.5.1 Energy Balance at the Top of the Atmosphere

The net radiation absorbed at the top of the atmosphere can be described with the following equation from Hartmann (2015):

$$R_{TOA} = S_{TOA}(1 - \alpha) - OLR \tag{1.9}$$

R_{TOA} is the net radiation at the top of the atmosphere, S_{TOA} is the incoming solar radiation at the top of the atmosphere, α is the albedo (which includes both surface properties and cloud effects), and OLR is the outgoing longwave radiation at the top of the atmosphere. S_{TOA} changes are mainly due to the angle of incidence, and overall does not change due to human induced climate change. The average albedo of Earth is about 0.29, with the lowest albedo occurring in the tropical oceans, and the highest values (>0.60) occurring over snow and ice covered polar regions. Reductions in sea

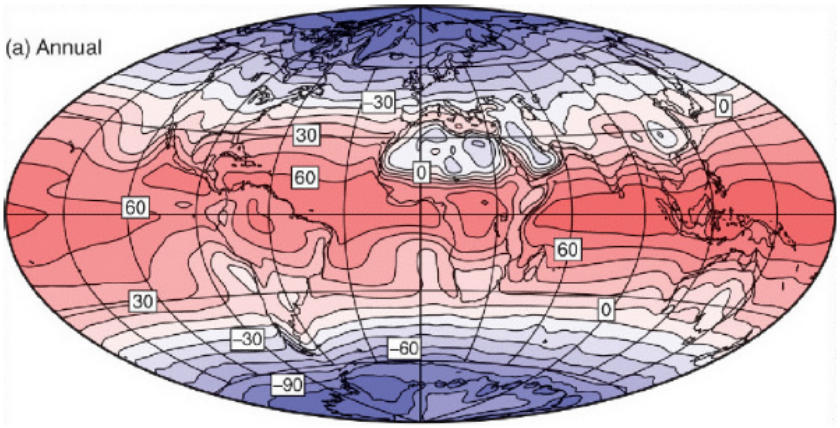

Figure 1.9: This figure shows the net radiation out of the top of the atmosphere. Units are in W m^{-2} (Hartmann, 2015).

ice and land ice can reduce the global albedo. The OLR is largely determined by the temperature of the object emitting the radiation. In desert regions, with fewer clouds and higher surface temperatures, there are higher values of OLR. In polar regions, where we see many clouds and lower temperatures, the are lower values of OLR.

Fig. 1.9 shows the net radiation out of the top of the atmosphere, on a latitude longitude map. There are positive values in the net radiation near the equator and tropics, with increasingly negative values towards the polar regions. This pattern occurs due to the excess absorption of shortwave radiation in the tropics, and excess outgoing longwave radiation in the polar regions. Fig. 1.10 shows the zonal average of fig. 1.9. It more clearly shows the latitudinal dependency for the net radiation pattern. There is positive net radiation roughly between 40°S to 40°N, and negative net radiation elsewhere. This latitudinal dependency is what gives rise to the poleward energy flux on Earth (Hartmann, 2015).

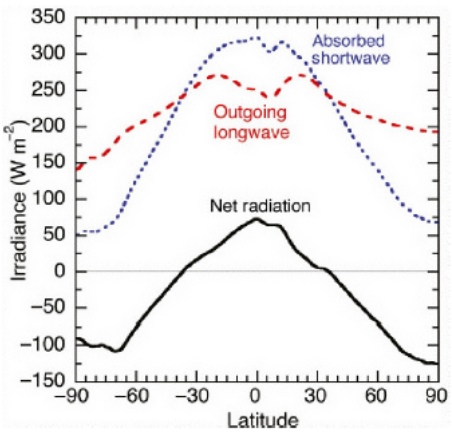

Figure 1.10: This figure shows the zonal average of net radiation out of the top of the atmosphere. Units are in W m^{-2} (Hartmann, 2015).

1.5.2 Poleward energy transport

The following equation describes the poleward flux of energy on Earth (Hartmann, 2015):

$$\frac{\partial \mathrm{E_{ao}}}{\partial \mathrm{t}} = \mathrm{R_{TOA}} - \Delta \mathrm{F_{ao}} \tag{1.10}$$

$\frac{\partial \mathrm{E_{ao}}}{\partial \mathrm{t}}$ is the time rate of change in energy at the top of the atmosphere, and $\Delta \mathrm{F_{ao}}$ is the divergence of the horizontal flux of energy in the atmosphere and oceans. $\frac{\partial E_{ao}}{\partial t}$ averaged over a year will end up being quite small, it can be assumed to be 0. This reduces Eq. 1.10 to:

$$\mathrm{R_{TOA}} = \Delta \mathrm{F_{ao}} \tag{1.11}$$

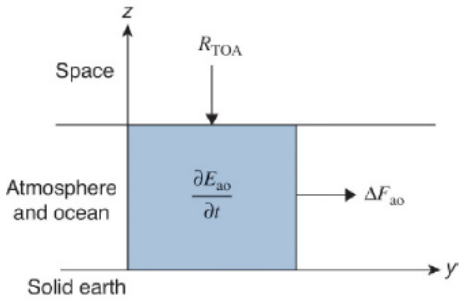

Figure 1.11: This figure shows how we can interpret Eq. 1.11 (Hartmann, 2015).

Fig. 1.11 shows how we can interpret eq. 1.11 in the climate system. The excess of net radiation, seen in fig. 1.10, is balanced by the divergence in the horizontal flux of energy. To quantify the amount of energy transported in a latitude belt integrate

the net radiation over a polar cap region using the following equation:

$$F(\Phi) = \int_{-\pi/2}^{\Phi} \int_{0}^{2\pi} R_{TOA} a^2 \cos\Phi \, d\lambda \, d\Phi \tag{1.12}$$

a is the mean radius of Earth, Φ is latitude, and λ is longitude. Fig. 1.12 shows the zonal plot of eq. 1.12. The peak poleward flux of energy occurs in the mid-latitudes, with a max of 5.8×10^{15} W of energy. In the equatorial regions, the poleward flux from the atmosphere and ocean are comparable. The atmosphere is responsible for most of the poleward transport outside of the equatorial latitudes (Hartmann, 2015).

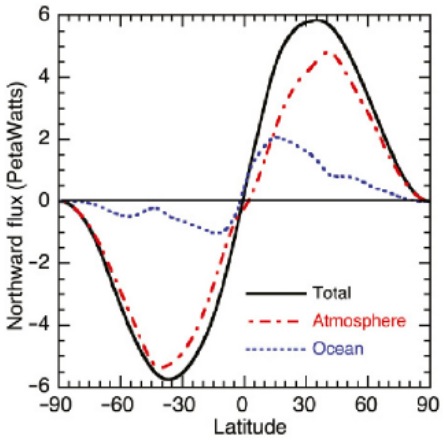

Figure 1.12: Eq. 1.12 when plotted shows the northward flux of energy from the atmosphere and ocean (Hartmann, 2015).

1.6 The "Two-stream" Approximation

In a radiative transfer model of Earth's atmosphere it can become difficult to discern how longwave emissions from various layers influence each other. The "two-stream" approximation helps to simplify the interpretation of the vertical structure of

longwave emissions. Frierson et al. (2006) describe a "gray" broadband approximation with no consideration of wavelength dependence within the longwave band. To start, the following radiative equations should be defined:

$$\frac{dU}{d\tau} = (U - B) \tag{1.13}$$

$$\frac{dD}{d\tau} = (B - D) \tag{1.14}$$

With U being the upward longwave radiation from the layer below, D as the downwelling longwave radiation from the layer above, τ is the optical depth, and B = σT^4 (Stefan-Boltzmann law). The boundary conditions are: $U[\tau(z = 0)] = \sigma T_s^4$ at the surface and $D(\tau = 0) = 0$ at the top of the atmosphere. The radiative source term for eq. 1.2 is:

$$Q_r = -\frac{1}{c_p \rho} \frac{\partial (U - D)}{\partial z} \tag{1.15}$$

ρ is density and c_p is specific heat capacity. Applying the chain rule, and noting that $\frac{d\tau}{dz} < 0$, eq. 1.15 can be written as:

$$Q_r = \frac{1}{c_p \rho} \left| \frac{d\tau}{dz} \right| \left(\frac{dU}{d\tau} - \frac{dD}{d\tau} \right) \tag{1.16}$$

Implementing equations 1.13 and 1.14, and subbing in B = σT^4 into eq. 1.16, the result is:

$$Q_r = \frac{1}{c_p \rho} \left| \frac{d\tau}{dz} \right| \left(U + D - 2\sigma T^4 \right) \tag{1.17}$$

T is the temperature of an atmospheric layer. U is dependent on the temperature of the layer below, with D being dependent on the temperature of the layer above.

The implication of eq. 1.17 is that the temperature of a given atmospheric layer is dependent on the incoming longwave emissions from the above and below layers along with the layer's longwave outgoing emission. Temperature changes due to longwave emissions near the surface are dominated by the D term. In the middle to upper troposphere, the combination of both the D and U terms are of roughly equal influence. While temperature changes in the stratosphere due to longwave emissions are dominated by the U term. This helps interpret results in sec. 3.2.

1.7 Aerosol Effects: Direct, Indirect, and Semi-direct

Aerosols' effects on climate are typically organized into 3 categories; Direct, Indirect, and Semi-Direct.

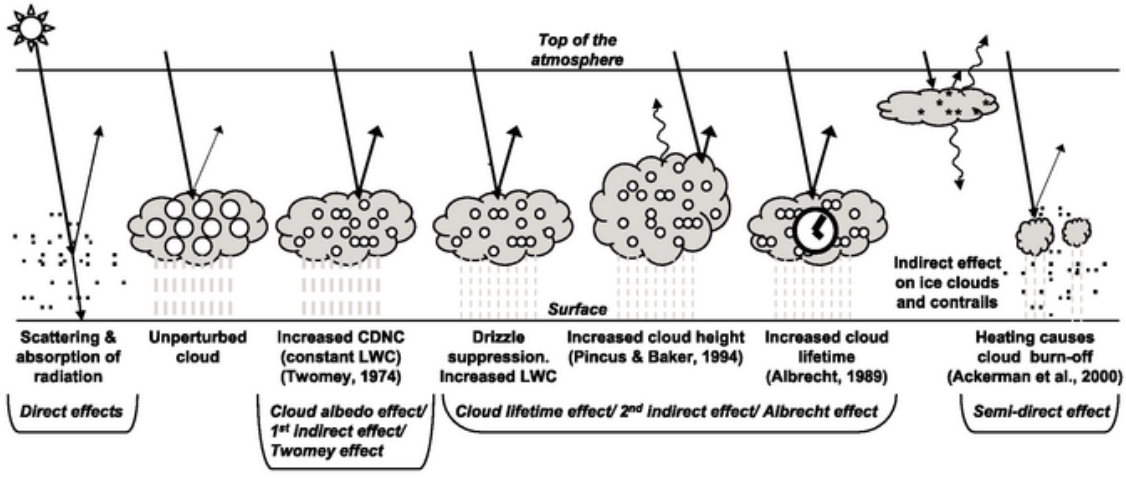

Figure 1.13: Direct, Indirect, & Semi-direct Effects: a description of the various aerosol effects described in IPCC AR4 report (Forster et al., 2007).

1.7.1 Direct Aerosol Effects

Direct effects of aerosols are how aerosols tend to scatter and absorb shortwave and longwave radiation in the atmosphere. Sulfate aerosol in the stratosphere, from volcanic eruptions, has the most pronounced cooling effect due to its efficient scattering diameter ($<$ 1 um) (Forster et al., 2007). Light-absorbing organic matter, also known as "brown carbon", might contribute as much as 20% of all carbonaceous aerosol direct forcing worldwide (Xie et al., 2017). Secondary Organic Aerosols (SOAs) form from volatile organic compounds (VOCs), with biogenic VOCs (BVOCs) constituting the majority, and can act as absorbing or scattering aerosols depending on their chemical aging.

1.7.2 Indirect Aerosol Effects

The aerosol indirect effects are how aerosols change the formation and precipitation efficiency of liquid, ice and mixed-phased clouds. These changes to cloud properties then have an indirect influence on radiative forcing (Penner et al., 2018). Fig. 1.13 summarizes the 1st and 2nd aerosol indirect effects.

Twomey (1974) describes the 1st indirect aerosol effect. If the liquid water content of a cloud is held constant, but there is an increase of cloud droplet number concentration (CDNC), the cloud can reflect more shortwave radiation back out to space. Twomey describes how increases in CDNC can occur in polluted air. This 1st

indirect effect changes the cloud albedo.

Cloud lifetime indirect effects are summarized in fig. 1.13. The drizzle suppression effect has been studied in polluted air, where particles tend to have a smaller effective radius. This smaller effective radius results in longer time periods for cloud droplets to grow into precipitation (Huang et al., 2019). This results in clouds having a longer lifetime, meaning the cloud can reflect more shortwave radiation over its lifetime. Pincus et al. (1994) investigated the influence of shipping emissions on low-level marine clouds. They found that the increase of cloud condensation nuclei (CCN) in the plumes resulted in increased cloud top heights, implying increased cloud thickness. This effect leads to more shortwave being reflected resulting in an increase in global albedo. Albrecht (1989) describes how increases in aerosol concentration over oceans may reduce precipitation, thereby increasing the lifetime of low-level marine clouds. This effect is very similar to the drizzle suppression effect, and results in an increase in global albedo. Fig. 1.13 describes one last indirect effect on ice clouds and contrails. These high clouds are optically thin and are transparent to much of the incoming shortwave radiation. They tend to trap outgoing longwave radiation from the surface. This results in a net warming effect. Contrails from airplanes seem to increase this effect, contributing to climate warming (Kärcher, 2018).

1.7.3 Semi-direct Aerosol Effects

The semi-direct effect was first defined by Ackerman et al. (2000) as an aerosol effect caused by absorbing aerosols, like black carbon and dust. These absorbing aerosols can heat up the air surrounding low clouds, burning them off. In their simulations they found that cloud coverage over the Indian Ocean during the monsoon can be reduced by almost 50% due to the cloud burning effect. Though, other studies suggest that the semi-direct effect is not always a positive radiative forcing.

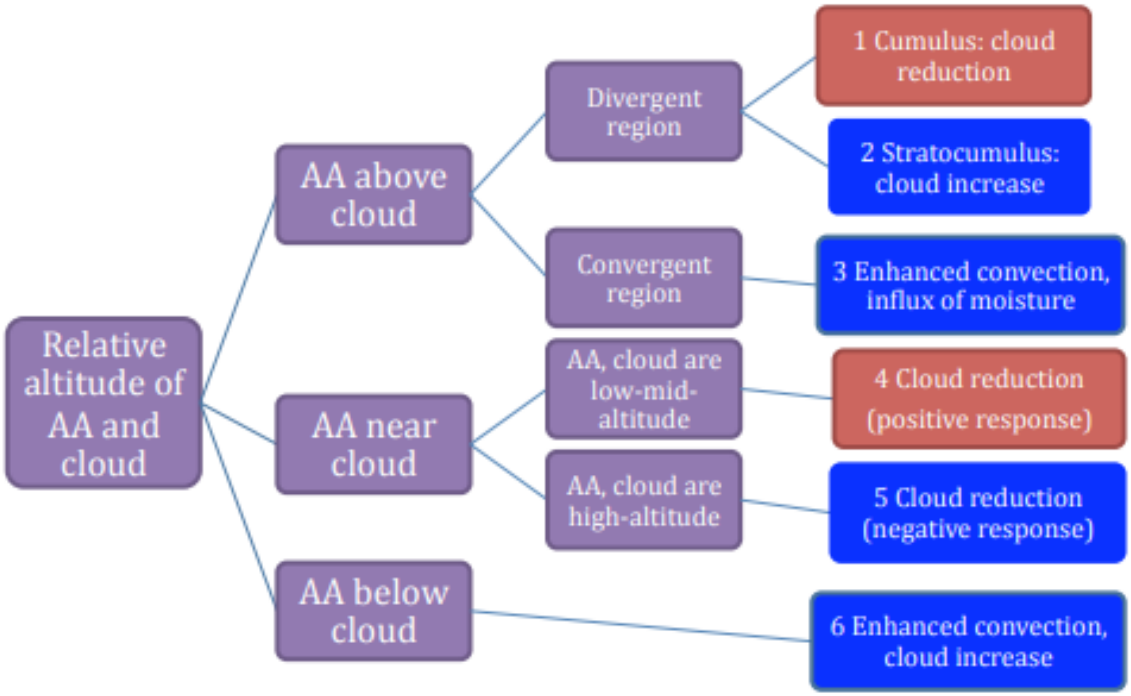

Figure 1.14: A framework for defining the radiative forcing effects due to the semi-direct effects of absorbing aerosols (AA) (Koch et al., 2010).

The positive and negative feedbacks from the semi-direct effects of absorbing aerosols are seen in fig. 1.14. Koch et al. (2010) suggests that depending on what

altitude, proximity to the cloud, divergence regime, and/or cloud type the AAs affect they can either have a positive or negative radiative forcing. From fig. 1.14 it is seen that the positive forcings occur due to cumulus cloud reduction and low-mid-altitude cloud reduction. Reduced high altitude cloud due to AAs is a negative feedback, along with stratocumulus cloud increases, and enhanced convection. The enhanced convection can either be due to an increase of AAs above the cloud in a convergence zone, or due to an increase of AA below the cloud.

1.7.4 Cloud Condensation Nuclei and Hygroscopicity

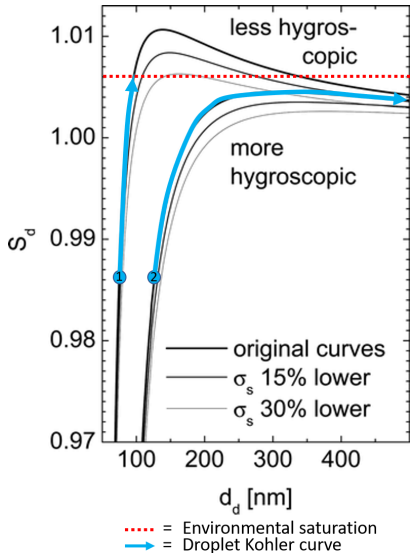

Figure 1.15: Influence of hygroscopicity on CCN saturation and diameter. The value of the y-axis can be interpreted as the supersaturation vapour pressure, ie the (actual vapour pressure)/(saturation vapour pressure at a given temperature). The x-axis is the diameter of the particle. The dashed red line indicates the ambient supersaturation or environmental saturation. (1) represents the less hygroscopic CCN (2) represents the more hygroscopic CCN (Wex et al., 2008).

Figure 1.15 shows there is a critical supersaturation (S_d) for any given aerosol. If aerosol 2 (more hygroscopic) starts at some initial size, fig. 1.15 shows it will be able to saturate below supersaturation and will continue to grow in diameter (potential cloud droplet). If the ambient supersaturation is below the Sc or critical supersaturation, like aerosol 1 (less hygroscopic), the droplet will stop growing. These types of nearly saturated aerosols are considered haze drops and contribute to smoggy days in the summer. Though, haze particles can still form from more hygroscopic aerosol. Conversely, aerosol 1 (less hygroscopic) can still eventually become cloud droplets if the ambient saturation moves above the Kohler curve. Overall, aerosols that are more hygroscopic will saturate at lower ambient supersaturations than particles that are less hygroscopic (Wex et al., 2008). The specificity of hygroscopicity for various aerosols in climate aerosol models still needs further improvement.

1.8 Biogenic Volatile Organic Compounds, Secondary Organic Aerosols, and Tropospheric Ozone production

1.8.1 Biogenic Volatile Organic Compounds (BVOCs)

BVOCs are an important precursor to SOAs. BVOC annual emissions are estimated to be about 1000 Tg per year (Guenther et al., 2012). Isoprene (535 Tg

yr^{-1}) represents about half of all annual BVOC emissions, and predominantly comes from broadleaf deciduous trees. Monoterpenes and Sesquiterpenes make up much of the remaining portion of BVOCs. Monoterpenes are predominantly emitted from Conifers (Mahilang et al., 2021). There are estimated to be nearly ten thousand to over a million different organic compounds in the atmosphere (Guenther et al., 2012). The species' specificity of BVOC emissions means there are regionally specific BVOC emissions, leading to great spatial variation in BVOC composition. VOCs and BVOCs are oxidized in the atmosphere by several different chemical species, like the hydroxyl, nitrate, and chlorine radicals, and ozone.

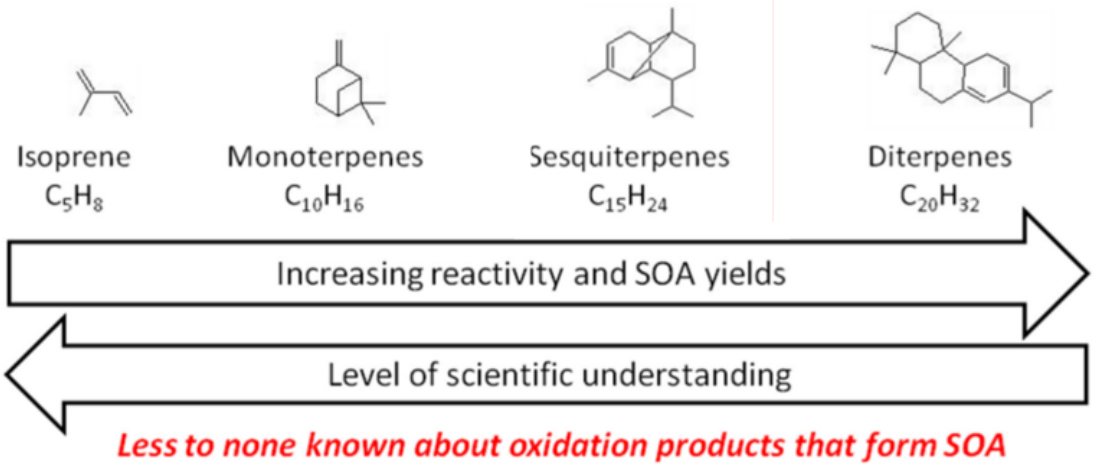

Figure 1.16: BVOC reactivity and structures (Goldstein et al., 2020).

Fig. 1.16 shows the various structures of BVOCs, along with their reactivity. Isoprene, generally one of the most studied BVOC, is the least reactive. Diterpenes, generally the least studied, have higher reactivity and SOA yields. Diterpenes are not nearly as ubiquitous as isoprenes and monoterpenes (Goldstein et al., 2020).

Typically the reactions with BVOCs are initiated at the double-bonds of these organic structures.

1.8.2 Secondary Organic Aerosols (SOAs), Tropospheric Ozone formation

The oxidization of BVOC/VOCs in the atmosphere leads to the production of SOAs. Biogenic SOAs make up the majority of SOA loading with 88 TgC yr^{-1} compared to 17 TgC yr^{-1} from anthropogenic SOA. This means about 84% of the global SOA loading is biogenically sourced (Srivastava et al., 2022).

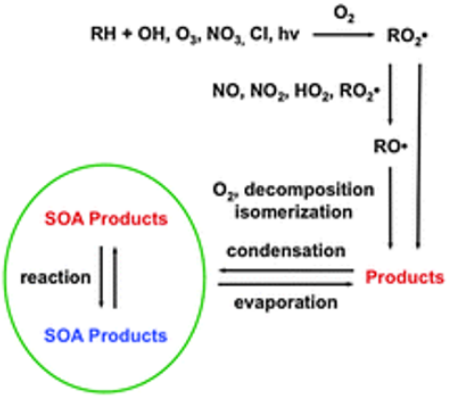

Figure 1.17: BVOC oxidation which leads to SOA formation (Ziemann et al., 2012).

The oxidation reactions are typically initiated at a double-bond in the VOC, creating peroxy radicals. In fig. 1.17 this step is seen in the RH + OH, ozone, etc. These peroxy radicals can then react more through further oxidation reactions (HO_2, RO_2, NO_3, etc.) These products can then decompose or isomerize (Schwantes et al., 2015; Srivastava et al., 2022). In the troposphere, BVOC/VOC reactions with NO_X

efficiently produce ozone when the ratio of VOC/NO_X is between 4/1 to 15/1, with the peak production of ozone occurring at a VOC/NO_X ratio of 8/1 (Finlayson-Pitts et al., 1993). The important reaction for ozone formation from VOCs is: (TR1) $RO_2 + NO \rightarrow RO + NO_2$. The subsequent reactions lead to ozone production: (TR2) $NO_2 + hv \rightarrow NO + O$, (TR3) $O + O_2 \rightarrow O_3$. NO_X emissions come from natural and anthropogenic sources, with the latter increasing from < 1 Tg NO_2 yr^{-1} in 1850 to 125 Tg NO_2 yr^{-1} in 2000 (Hoesly et al., 2018). This process of ozone production, along with some minor contributions from stratospheric transport into the troposphere, are the primary O_3 sources in the troposphere (Finlayson-Pitts et al., 1999).

1.8.3 Organic nitrate aerosols

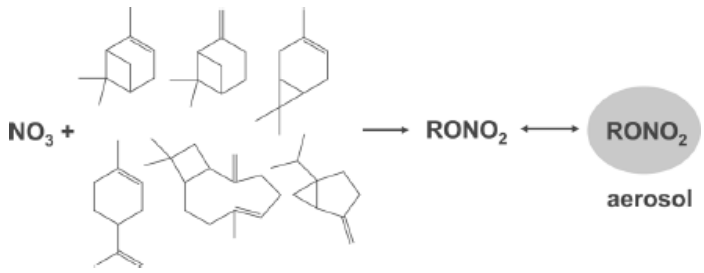

Figure 1.18: Simplified organic nitrate formation from BVOC, and organic nitrate aerosol (subset of SOAs) (Fry et al., 2014).

Figure 1.18 shows a simplified diagram of the formation of organic nitrate ($RONO_2$) from nitrate and BVOC. Organic nitrate contributes to the formation of SOA, especially at nighttime due to the "vampire" radical NO_3. $[NO_3]$ is significantly higher at nighttime due to the lack of photolysis and reduced NO sink. Isoprene-NO_3 oxidation

products have a small SOA yield (4-24%) compared to monoterpene/sesquiterpene-NO_3 oxidation products (Fry et al., 2014).

Xu et al. (2015a), Xu et al. (2015b) took measurements during the Southern Oxidant and Aerosol Study (SOAS), using a High-Resolution Time-of-Flight Aerosol Mass Spectrometer (HR-ToF-AMS), in the southeastern USA. They found that organic nitrate functional groups amounted to roughly 5-12% of organic aerosol mass. In this study, isoprene was more abundant than monoterpenes and sequisterpenes due to the location in the SE USA. Ayres et al. (2015), from the same SOAS data, performed a measurement constrained nighttime model and calculated a molar yield of 23-44% for organic nitrate aerosol (predominately formed from monoterpenes in the nocturnal boundary layer). They also observed that about 30-45 % of total nitrogen (NO_Y) budget came from particle-phase organic nitrates.

Organic nitrate in the particle-phase appears to contribute significantly to the total organic aerosol mass, with a greater yield in the summer. Higher concentrations of particle-phase organic nitrates are found in polluted regions with a NO_X source compared to remote regions. The inclusion of NO_3-BVOC reactions increases SOA yields in Europe by 50-70%. A humid climate contributes to a short-lifetime of organic nitrate particulate when there is sufficient BVOC and NO_X. This short-lifetime is one reason why observational studies have underestimated organic nitrate's influence on SOA formation (Ng et al., 2017).

The radiative effect of organic nitrate aerosol depends on a number of factors.

Brown carbon (BrC), a component of SOA with humic-like substances, organic nitrates, and organosulfate species, is known to lead to increased shortwave absorption in the troposphere. BrC is found in association with primary and secondary organic carbon. BrC is distinct from black carbon (BC) due to its optical properties, namely that BrC has a spectral-dependent absorption smoothly increasing from shorter visible wavelengths to the UV (Ng et al., 2017). BC absorbs strongly across the whole solar spectrum (Liu et al., 2015). BrC leads to about 0.04 to 0.11 W m^{-2} warming at the top of the atmosphere, but at the surface results in a reduction of -0.06 to -0.14 W m^{-2} (Feng et al., 2013). The hygroscopocity of organic aerosol, predominately formed from BVOC-NO_3 reactions, was lower than other types of organic aerosol (Cerully et al., 2015). This suggests that nighttime organic aerosol (from monoterpene reactions) may act less efficiently as CCN compared to other types of organic aerosol (Ng et al., 2017). This inefficiency does not necessarily result in less cloud formation, as increased CCN availability in a sufficiently saturated parcel of air will still lead to cloud formation. There is evidence that polluted thunderstorms lead to more precipitation due to increased scavenging of these smaller SOA and other aerosol (Liu et al., 2019).

1.9 Ozone Formation and Transport in the Stratosphere

Ozone in the stratosphere is a vital chemical component for life on Earth. Ozone efficiently absorbs UV-A and UV-B wavelengths of light, preventing it from reaching the surface. This absorption of shortwave radiation acts to heat up the stratosphere. This is the reason why above the tropopause temperatures increase with height. The maximum density of ozone, of 5×10^{18} molecule m^{-3}, occurs around 25-30 km above the surface. Peak ozone concentration happens at this altitude due to the Chapman mechanism.

1.9.1 Chapman Mechanism

Ozone formation is regulated by the following reactions:

(SR1 - slow)	$O_2 + hv \rightarrow O + O$	($\lambda < 240$ nm)
(SR2 - fast)	$O + O_2 + M \rightarrow O_3 + M$	
(SR3a - fast)	$O_3 + hv \rightarrow O_2 + O(^1D)$	($\lambda < 320$ nm)
(SR3b - fast)	$O(^1D) + M \rightarrow O + M$	
(SR4 - slow)	$O_3 + O \rightarrow 2O_2$	

The two most important reactions, because they are the slow reactions and constrain

the reaction rate, are the SR1 and SR4 reactions. This is why the maximum ozone density occurs between 20-30 km, as at this altitude there is a balance between the vertical production of O atoms and the availability of O_2 (decreases with height) (Finlayson-Pitts et al., 1999).

Another reaction that occurs with $O(^1D)$, though at a much slower rate is:

$$\text{(SR5)} \qquad O(^1D) + H_2O \rightarrow 2OH$$

This competes with (SR3b), the production of $O(^3P)$, and is fairly ineffective in the stratosphere due to the low availability of water. However, it becomes an important reaction in the production of hydroxyl that contributes to the HOx catalytic loss cycle (Finlayson-Pitts et al., 1999).

1.9.2 HOx Catalytic Cycle

(SR5) initiates the destruction of O_3 and the following reactions propagate it:

$$\begin{aligned}
\text{(SR5 - Initiation)} \qquad & O(^1D) + H_2O \rightarrow 2OH \\
\text{(SR6 - Propagation)} \qquad & \mathbf{OH} + O_3 \rightarrow O_2 + HO_2 \\
\text{(SR7 - Propagation)} \qquad & HO_2 + O_3 \rightarrow 2O_2 + \mathbf{OH} \\
\text{(SR6 + SR7 - Catalytic Loss)} \qquad & 2O_3 \rightarrow 3O_2 \\
\text{(SR8 - Termination)} \qquad & OH + HO_2 \rightarrow H_2O + O_2
\end{aligned}$$

Reactions SR5 through SR8 complete a catalytic loss cycle. SR5 inititates the chain reaction, by creating a pool of hydroxyl radicals in the stratosphere. Then SR6 destroys ozone while producing HO_2, which can then further destroy ozone via SR7. SR7 then replenishes the OH molecule and it can then contribute to SR6 reactions again. The **OH** bolded, in SR6 & SR7, is to highlight how the OH is regenerated in this catalytic cycle. This process can occur 10^6 to 10^7 times. Eventually, SR8 terminates this cycle producing water and oxygen. This partially contributes to the destruction of O_3 (Finlayson-Pitts et al., 1999).

1.9.3 NOx catalytic cycle

Another contributor to ozone destruction is the NO_X catalytic cycle. NO_X = NO + NO_2 and leads to ozone destruction with the following reactions:

$$\text{(SR9 - propagation)} \qquad \mathbf{NO} + O_3 \rightarrow NO_2 + O_2$$

$$\text{(SR10 - propagation)} \qquad NO_2 + O \rightarrow \mathbf{NO} + O_2$$

$$\text{(SR9 + SR10 - Catalytic Loss)} \qquad O + O_3 \rightarrow 2O_2$$

$$\text{(SR11 - O(}^3\text{P) production)} \qquad NO_2 + h\nu \rightarrow NO + O$$

$$\text{(SR2 - Chapman)} \qquad O + O_2 + M \rightarrow O_3 + M + \text{heat}$$

$$\text{(SR12 - Termination)} \qquad NO_2 + OH + M \rightarrow HNO_3 + M$$

It should first be noted that the net reaction of SR9, SR11, and SR2 gives a "null cycle" (ie. hv $\rightarrow$ heat). Though, SR10 competes with SR11, so some NO_2 consumes

O. The net of SR9 and SR10 produces the catalytic loss cycle, again the important "recycled" NO is bold in these reactions. SR12 is a daytime termination step for this loss cycle. HNO_3 acts as a reservoir species for NO_X.

The following reactions become important for the nighttime loss of NO_X and act as reservoir species until the sun rise. These reactions are the same as in the troposphere:

(SR13)	$NO_2 + O_3 \rightarrow NO_3 + O_2$
(SR14 - N_2O_5 reservoir)	$NO_3 + NO_2 + M \rightarrow N_2O_5 + M$
(SR15)	$NO_3 + hv \rightarrow NO_2 + O$
(thermal reaction)	$N_2O_5 \rightarrow NO_3 + NO_2$
(SR16)	$HNO_3 + hv \rightarrow NO_2 + OH$
(SR17)	$HNO_3 + OH \rightarrow NO_3 + H_2O$
(SR18)	$N_2O_5 + hv \rightarrow NO_3 + NO_2$
(SR19)	$N_2O + O(^1D) \rightarrow 2NO$

SR13 and SR14 show the temporary loss of NO_X during the night. The products act as NO_X reservoirs until sunrise, when SR15, SR16, the thermal reaction, and SR18 occur due to photolysis and daytime heating. SR17 can also release more NO_3, which then can be converted into NO_2, and occurs only when OH is produced in the daytime. Another important classification to make is NO_Y = NO_X + reservoirs = NO + NO_2 + NO_3 + N_2O_5 + HNO_3 + organic nitrates + etc (Finlayson-Pitts et al.,

1999).

1.9.4 CLOx catalytic cycle

The ClO_X cycle became an important area of study with the discovery of the ozone hole and CFC catalyzed ozone destruction. CFCs contribute to ozone destruction because they have a long lifetime in the stratosphere and provide atomic chlorine radicals for ozone destruction (Molina et al., 1974). These discoveries were vital in creating the Montreal Protocol, and reducing CFC emissions. In the context of this study, because emissions are fixed to the year 1850 C.E., CFC emissions are not contributing to the pool of Cl. Instead, natural emissions of halogens (all of which react similarly to Cl) largely come from methyl bromide and methyl chloride emissions from oceanic sources, terrestrial plants and fungi, biomass burning, etc. (Rhew et al., 2000). The following reactions show how these methyl halogens can result in ozone destruction, Cl will be used in the reactions but similar reactions occur with bromide species:

$$\text{(SR20 - release of Cl radicals)} \qquad \text{R-Cl} + \text{hv} \rightarrow \text{R} + \mathbf{Cl}$$

$$\text{(SR21 - ozone destruction)} \qquad \mathbf{Cl} + O_3 \rightarrow ClO + O_2$$

$$\text{(SR22 - Cl replenishment)} \qquad ClO + O \rightarrow \mathbf{Cl} + O_2$$

$$\text{(SR21 + SR22 - net)} \qquad O_3 + O \rightarrow 2O_2$$

Similarly as the other catalytic destruction cycles, Cl is replenished up to 10^6 times. These reactions then terminate in the following way:

(SR23 - termination) $\mathrm{Cl + RH\ (e.g.\ VOC) \rightarrow HCl + R}$

(SR24 - termination) $\mathrm{ClO + NO_2 + M \rightarrow ClONO_2}$

SR23 and SR24 act as termination reactions for the $\mathrm{ClO_X}$ destruction cycle, and the reservoir species (HCl & $\mathrm{ClONO_2}$) can either be transported to the troposphere through wet or dry deposition, or contribute back to the pool of $\mathrm{ClO_X}$ with the following reactions:

(SR25 - Cl release) $\mathrm{HCl + OH \rightarrow H_2O + Cl}$

(SR26 - Cl release) $\mathrm{ClONO_2 + hv \rightarrow NO_3 + Cl}$

There is also an interaction between $\mathrm{NO_X}$ and ClO that can contribute to ozone destruction in the following way:

(SR27) $\mathrm{ClO + NO \rightarrow Cl + NO_2}$

(SR28) $\mathrm{Cl + O_3 \rightarrow ClO + O_2}$

(SR27 + SR28 - net) $\mathrm{O_3 + NO \rightarrow NO_2 + O_2}$

The net of SR27 and SR28 leads to further ozone destruction. These reactions of $\mathrm{ClO_X}$ catalyzed ozone destruction are highly dependent on the time of the year and largely are important in the polar regions (especially in the Southern Hemisphere) (Finlayson-Pitts et al., 1999).

1.9.5 Polar Stratospheric Clouds (PSCs)

Polar stratospheric clouds (PSCs) occur near the poles, with them forming more preferentially in the Southern Hemisphere. The altitude of PSCs is typically between 15 to 25 km, which can be seen in fig 1.14. They can be composed of stratospheric sulfuric acid aerosol (SSA, H_2SO_4-H_2O), supercooled ternary solution (STS, H_2SO_4-HNO_3-H_2O), nitric acid trihydrate (NAT, $HNO_3 \cdot 2H_2O$), other HNO_3 or H_2SO_4 hydrates, H_2O ice, or any mixture of these aerosols (Tritscher et al., 2021). HNO_3 partitioned in the condensed phase, HNO_3 Nitric Acid Trihydrate (NAT) or STS droplets contributes to the destruction of ozone via heterogeneous reactions occurring on PSCs. (Höpfner et al. (2006)).

These heterogeneous reactions are as follows:

(SR32 - heterogenous)	$HCl_{(s)} + ClONO_{2(g)} \rightarrow Cl_2 + HNO_{3(s)}$	
(SR33 - photolysis)	$Cl_2 + hv \rightarrow 2Cl$	$(\lambda < 500nm)$
(SR28 - ozone destruction)	$Cl + O_3 \rightarrow ClO + O_2$	

The release of Cl_2 then feeds back into the ClO_X destruction feedback with SR28. These heterogeneous reactions occur most efficiently in the frigid stratospheric air. Paying attention to SR32, HNO_3 can stay present in the PSC, leading to lower levels of NO_X in the gas-phase. This gas partitioning results in a reduced reaction rate of SR24 (the $ClONO_2$ termination reaction), leading to a preference for the destructive

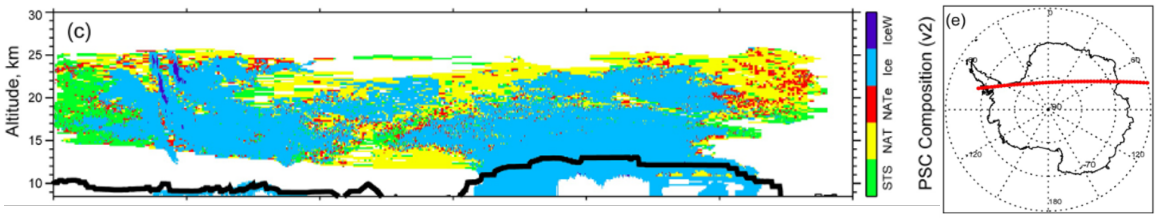

Figure 1.19: Transect from the CALIPSO orbiter mission from July 17th, 2008. The c panel is the PSC chemical composition, with the e panel showing the orbit of CALIPSO (Tritscher et al., 2021).

propagation reactions (Finlayson-Pitts et al., 1999). PSCs are a stratospheric cloud that occurs most often in the winter time, and are far more common over the South Pole. They are very sensitive to temperature changes, only forming in temperatures below 197 K.

Fig. 1.19 shows the spatial structure and chemical composition of polar stratospheric clouds over Antarctica taken over a day. It's seen that a majority of the PSCs in this transect are ice aerosols, as opposed to NAT, STS, and NATe. It would appear that the NAT type PSCs typically form in the coldest regions of the stratosphere (Tritscher et al., 2021). PSCs can be further organized into two types; Type 1 PSCs: <1um aerosols, HNO_3 rich, forming in temperatures below 195 K & Type 2 PSCs: 10 um to 1 mm aerosols, H_2O-HNO_3 hydrates, forming in temperatures below 190 K. The type 2 PSC have the fastest heterogeneous reaction rates (Finlayson-Pitts et al., 1999).

1.9.6 Brewer-Dobson Circulation

The Brewer-Dobson Circulation (BDC) is a global stratospheric general circulation that transports air from the tropical troposphere and stratosphere to the polar stratosphere. Dobson (1956) confirmed the existence of this circulation via water vapour measurements. The BDC influence on ozone is to move ozone from the tropics to the polar stratosphere. This is why measurements of total ozone, seen in fig. 1.20, are higher over the poles compared to the tropics. The seasonality of the

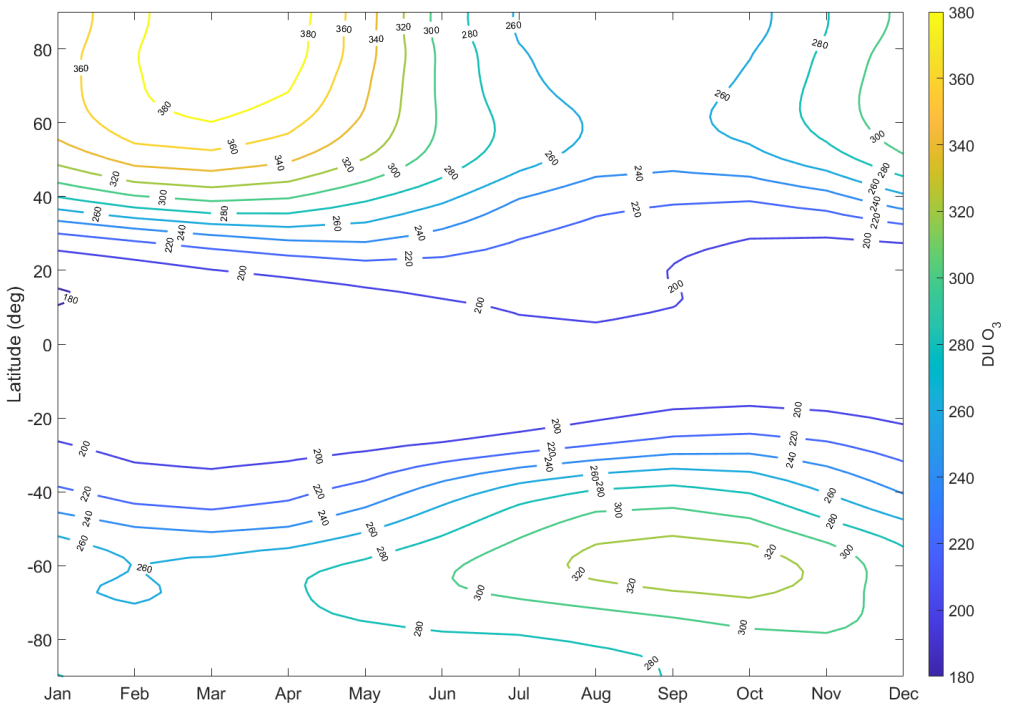

Figure 1.20: Total Ozone Column (in DU) from a 30-year climate simulation with CESM2-WACCM6 BWma1850. The contour interval is 20 DU. The y-axis is latitude (deg) while the x-axis is the month.

BDC is seen in fig. 1.20, with the Northern Hemisphere having elevated ozone in the northern winter, and the Southern Hemisphere having elevated ozone in the southern winter.

The following equation, described by Andrews et al. (1978), is the residual-mean-circulation in a "Transformed Eulerian-Mean (TEM)" form:

$$\overline{v}^* = \overline{v} - \rho_0^{-1} \frac{\partial}{\partial z} \left(\frac{\rho_0 \overline{v'\theta'}}{\overline{\theta}_z} \right) = -\frac{1}{\rho_0 \cos\phi} \frac{\partial \Psi}{\partial z} \tag{1.18}$$

Ψ is as mass-stream function and ϕ is latitude. Calculating Ψ allows for a way of quantifying the BDC. This equation accounts for the often strong cancellation between mean and eddy heat transport. Under the assumption of quasi-geostrophic flow with nonacceleration conditions, this calculation is an adequate measure of diabatic circulation (Butchart, 2014).

1.10 Ozone feedbacks between its chemistry and dynamics/transport

Ozone increases can be a consequence or a cause for stratospheric warming. This is why it takes careful analysis of model output to determine which factors result in increased ozone. In warming temperatures, heterogeneous reactions on PSCs occur

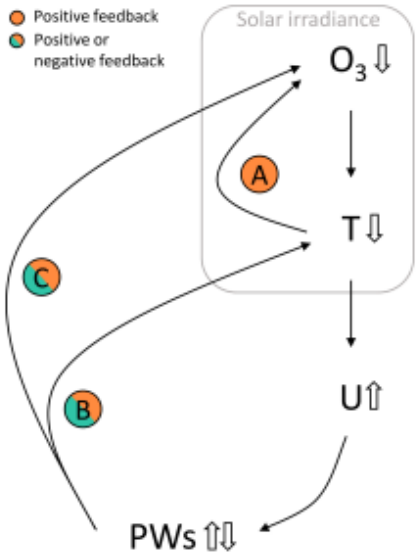

Figure 1.21: Ozone feedback between ozone chemistry and dynamics/transport (Haase et al., 2019).

less frequently resulting in less ozone destruction. In cooler temperatures, the opposite is true, leading to more ozone destruction.

Haase et al. (2019) present figure 1.21 as an example of what happens when a negative anomaly of ozone occurs. A reduction in ozone will result in a reduction in temperature, favouring ozone destruction. This would act to increase the strength of the polar night jet (U). If background westerlies are strong this can lead to a decrease of planetary wave propagation (PWs). This results in a less disturbed polar vortex, with coupled cooling of the polar vortex. Less ozone transport into the polar vortex occurs, further amplifying ozone reduction.

Now imagine if the background westerlies were reduced by some outside forcing, along with the polar night jet. This results in an increase of PWs, leading to a more disturbed polar vortex, coupled to a warming of this vortex. This would result

in more transport of ozone into the polar vortex (and hence lower stratosphere from increased descent), and increases of ozone on an annual basis. It is therefore important to identify which mechanism is the initial driver of change in the southern polar stratosphere (SPS). In this study, it will be seen in sec. 3.2 that the ozone response is due to changes in the zonal wind which are not driven by increases ozone. Rather, these changes to zonal wind are driven by temperature changes in the troposphere.

2 | Methods

2.1 The Community Earth System Model (CESM2)

CESM2 was picked as the model because it is open source and has extensive documentation and support. CESM2 consists of 7 components: land, river runoff, surface waves, ocean, land ice, sea ice, and the atmosphere. All of these components are coupled with the CIME5 coupler (Danabasoglu et al., 2020). The output data for this study came from the atmosphere component and can either be the Community Atmospheric Model (CAM6) or the Whole Atmosphere Community Climate Model 6 (WACCM6). In this study, the WACCM6 was picked as the atmospheric model component. Hereafter, we refer to CESM2 with the WACCM6 atmospheric component as CESM2-WACCM6.

2.1.1 The Whole Atmosphere Community Climate Model (WACCM6)

WACCM6 captures a large number of atmospheric chemical pathways all the way from Earth's surface up to the lower thermosphere. There are 70 model levels,

with a model top at an atmospheric pressure of 4.5×10^{-6} hPa (at around 130 km). The WACCM6 vertical level structure is set up in a hybrid sigma coordinate system. The WACCM6 has 231 prognostic chemical species with numerous chemical pathways for the whole atmosphere, with detailed modelling of SOAs. WACCM6 also uses the Modal Aerosol Model (MAM4), which is able to capture complex aerosol-cloud interactions (Danabasoglu et al., 2020). All of these properties make WACCM6 especially powerful when studying cloud-aerosol processes. WACCM6 also has a fully coupled ocean, which until recently has been computationally prohibitive. Now with modern computing, we are able to run both fully-coupled ocean and fully-coupled tropospheric chemistry. This allows investigation of questions related to tropospheric chemistry's impact on climate without having to prescribe sea surface temperatures.

2.1.2 CESM2-WACCM6 model configurations and analysis

Case Name	**Atmospheric Chemistry**	**Quasi-Biennial Oscilliation (QBO)**
BW1850	Full Atmosphere	QBO prescribed
BWma1850	Middle Atmosphere	QBO prescribed

Table 1: CESM2-WACCM6 configurations used in this study

The BW1850 case (full atmospheric chemistry WACCM6 case) and the BWma1850 ("simple" case) both have the quasi-biennial oscillation (QBO) winds prescribed to avoid possible confounding effects due to QBO differences. The QBO is a lower stratospheric wind variation that occurs over the tropics in 28-month cycles.

The compset for BWma1850 is BWma1850.f19_g17, and the compset for BW1850 is BW1850.f19_g17. A compset defines the physics, microphysics, chemistry, etc. that is included in the model. The f19_g17 indicates simulations were on a 1.9°× 2.5° lat-lon grid. The cases were run over 100-years. The BW1850 case has full atmosphere chemistry and was used as the comparison model. The BW1850 case implements the troposphere, stratosphere, mesosphere, and lower thermosphere (TSMLT) chemistry set. The BWma1850 uses the middle atmosphere, mesosphere, and lower troposphere (MAMLT) chemistry set. The chemistry set used in MAMLT is nearly identical to the chemistry set present in WACCM4, with two additions of $O^+(^2D)$ and $O^+(^2P)$ (Gettelman et al., 2019). WACCM6 implements the following chemical interactions: 231 solution species, 583 chemical reactions broken into 150 photolysis reactions, 403 gas-phase reactions, 13 tropospheric heterogeneous reactions, and 17 stratospheric heteorogenous reactions (Gettelman et al., 2019). Both of these configurations are control runs with human emissions fixed to pre-industrial levels (1850 C.E.). The motivation behind comparing these two cases is that we can isolate how tropospheric chemistry affects global atmospheric parameters by looking at the mean difference between the WACCM6 full chemistry case (hereafter referred to "BW1850") and the "simple" case with coupled chemistry confined to the middle atmosphere (hereafter referred to as "BWma1850").

One notable chemical species that is not included in either chemistry set is nitrous acid (HONO). HONO can photolyze via the following reaction: (TR4)

HONO + hv $\rightarrow$ OH + NO ($\lambda < 400$ nm). This chemical species contributes to the formation of hydroxyl radicals. HONO reactions are particularly relevant in polluted urban areas where concentrations can be up to a few parts per billion. Primary anthropogenic sources come from combustion processes, while primary natural emissions come from soil microbial activity and biocrusts. Secondary sources (chemically produced in the atmosphere/surface), are from gas-phase homogeneous reactions of NO and OH during the daytime or heterogeneous reactions with NO_2 at the surface (Kramer et al., 2020). The exclusion of HONO, especially in simulations of future climate, may impact the budget of OH. A parameterization of HONO processes is needed for these chemistry sets.

The annual means, calculation seen in eq. 2.1, were calculated by averaging over 100-years of output. Then mean differences, defined as BW1850 − BWma1850, were taken between the two simulations. The mean differences were then further analyzed to determine if those differences were statistically significant. Mean differences were taken as spatial averages and zonal averages. These latitude-longitude averages can be taken as:

$$\overline{X_{\lambda,\phi}} = \frac{1}{t_f - t_0} \int_{t_0}^{t_f} X(\lambda, \phi, t)\, dt \tag{2.1}$$

X can be any 2-D variable in a time series, with t in months. λ is the longitude and ϕ is the latitude. A few 2-D variables were averaged over all longitudes and made into 1-D zonal averages. The other zonal averages can be described with the following

equation:

$$\overline{X_{\phi,\sigma}} = \frac{1}{\lambda_f - \lambda_0} \int_{\lambda_0}^{\lambda_f} \frac{1}{t_f - t_0} \int_{t_0}^{t_f} X(\lambda, \phi, \sigma, t)\, dt\, d\lambda \tag{2.2}$$

Here X is any 3-D variable in a time series. σ is the vertical model level.

The statistical significance test involved two steps: First, the independent samples in each dataset were identified, and then a two-tailed t-test was performed on these samples. For each timeseries at each location, independent samples were identified using the 1-lag autocorrelation technique described by Bretherton et al. (1999). The null hypothesis assumes that the sample mean differences are normally distributed around 0 (ie. the two means of each dataset are the same). The lower bound and upper bounds of this distribution are the "tails", with an α-value representing the boundaries of the null hypothesis ($\frac{\alpha}{2}$ for each tail). If the mean differences fall in the tails of the distribution the null hypothesis is rejected and there are statistically significant differences in the means (Ott et al., 2015). The alpha value for this research is 0.05, representing a 95% confidence level. These regions with statistically significant differences in means will be considered "regions of interest" and will be the starting point for further research.

In the zonal mean section (3.2) all figures, except (fig. 3.17), include the BWma1850 climatology of the tropopause pressure level. This was calculated with eq. 2.2, but with the 2-D (+ time) variable of tropopause pressure. Tropopause climatology provides a delineation between the troposphere and stratosphere, and only varies from the BW1850 tropopause climatology by at most 3 hPa.

2.1.3 1850 Emissions Inventory

GHGs in the model come from the CMIP6 specified mixing ratios. CMIP6 emissions data also dictates anthropogenic reactive gases and aerosols (Gettelman et al., 2019). Biogenic emissions are taken from the MEGANv2.1 emissions dataset (Guenther et al., 2012). NO_X emissions from lightning are interactively generated (about $3-4$ TgN yr^{-1}). External forcings in both simulations are held fixed to 1850 levels.

Surface emissions (land and ocean) of CO_2 are held fixed at 284.7 ppmv, but CO_2 is transported and explicitly solved in the atmosphere in both configurations. BVOC and VOC emissions are fixed to 1850 concentrations. M (third-body molecule) and N_2 are held fixed in the atmosphere in both configurations. The following species are fixed at the lower boundary of the atmosphere model in both configurations: CCl_4, CF_2ClBr, CF_3Br, CFC-11, CFC-113, CFC-12, CH_3Br, CH_3CCl_3, CH_3Cl, CH_4, CO_2, H_2, HCFC-22, N_2O, CFC-114, CFC-115, HCFC-141b, HCFC-142b, CH_2Br_2, $CHBr_3$, H-2402, OCS, and CFC-11 eq. BW1850 also has SF_6 fixed at the lower boundary.

The historical GHG and other reactive gas species inventory is sourced from the Climate Model Intercomparison Project 6 (CMIP6) historical simulations. The historical simulations did not provide a formal uncertainty analysis, but rather state minimum uncertainties derived by other researchers. For example, the concentration of CO_2 for 1850 (284.7 ppmv) has a minimum uncertainty of 1.2 ppm variability. Please refer to Meinshausen et al. (2017) to get a detailed explanation of these his-

torical simulations.

2.1.4 Modal Aerosol Model 4 (MAM4)

Fig 2.1 shows the MAM4 aerosol modes and different tracers associated with them. The aerosol variables are: sulfate aerosol, sea salt aerosol, SOA, black carbon aerosol, primary organic matter aerosol (POM), and soil dust. Number concentration of each mode is also output.

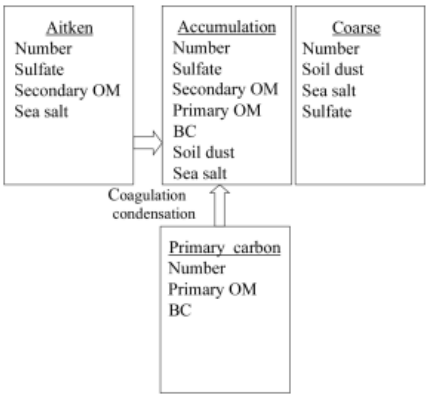

Figure 2.1: MAM4 aerosol modes and tracers (Liu et al., 2016).

Fig 2.1 shows us the 4 aerosol modes; Accumulation (a1/c1), Aitken (a2/c2), Coarse (a3/c3), and Primary Carbon (a4/c4) modes. "a" refers to aerosol in dry air, while "c" refers to aerosol in cloud. In order to calculate the sum of a particular aerosol one must sum over all aerosol modes and dry versus wet aerosol bins. Fig 2.2 shows the relative abundance and size of these various aerosol modes. MAM4 looked to improve on MAM3 by implementing a primary carbon bin on top of the other three modes. This was to explicitly treat the microphysical aging of primary carbonaceous

aerosols. Primary organic matter (POM) and black carbon (BC), that are emitted, are first placed in the primary carbon mode. In order for POM/BC to move from the primary carbon mode into the accumulation mode it must have either 8 monolayers of sulfate, or the same amount of SOA (same volume weighted hygroscopicity as the 8 layers of sulfate). POM and BC are given a hygroscopocity (κ) of 0. POM typically only has this hygroscopocity when it is freshly emitted from fossil fuels (Liu et al., 2016). When POM is emitted from biomass sources the κ is closer to 0.06-0.30 (Liu et al., 2010). This is likely an area in MAM4 that needs to be improved.

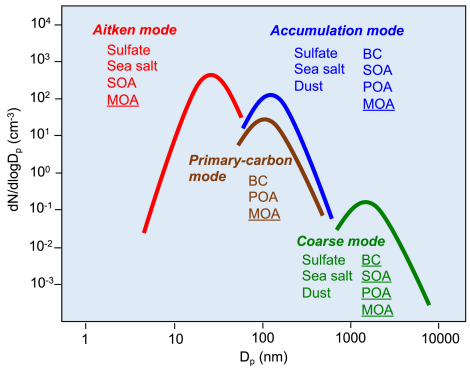

Figure 2.2: MAM4 aerosol modes relative abundance versus diameter. (Wang et al. (2020))

The tropospheric heteorogenous reactions occur with the following 4 aerosol modes; sulfate, BC, POM, and SOA. Stratospheric heteorogenous reactions work with the following 3 aerosol modes; sulfate, NAT, and water-ice.

The optical properties of BrC in MAM4 has been captured through the POM and BC emissions in the model. Brown et al. (2018) used the BC-to-OA ratio, OA being the total organic aerosol, to determine the BrC refractive index. OA would

include POM, BC, and SOA. The components of BrC in MAM4 are distributed across a number of model variables. While BrC concentration was not calculated for this work, it will be assessed in the future.

2.1.5 1-D Volatile Basis Set (VBS)

Hodzic et al. (2016) describe the modified 1-D volatile basis set (VBS) implemented in WACCM6. The original base SOA model configuration, used in BWma1850, is a simple volatile basis set with 4 oxidation bins for oxygenated semi-volatile organic compounds, and 2 additional bins for SOA aged from anthropogenic precursors and gas-phase oxidized volatile organic compounds (OVOCs). A rate constant is given for the chemical aging of anthropogenic oxidation intermediates by OH. The biogenic precursors in the model are not artificially aged.

The new modified VBS, implemented in the BW1850 case, informs its SOA formation mechanisms (the oxidation curve) from the Statistical Oxidation Model (SOM) first described by Cappa et al. (2012). The SOM implements improved SOA yields that account for wall-losses in chamber studies. SOM prognoses the multi-generational chemistry of SOAs, with fragmentation and functionalization being included. Functionalization is how the model adds chemical functional groups to an SOA, while fragmentation is how the model removes functional groups from existing SOA. All of these improvements have led to a more accurate depiction of SOA chemistry in the WACCM6 configuration (Hodzic et al., 2016).

Hodzic et al. (2016) compared their modelling results to in situ ground, airplane, and satellite observations. From these results they saw an improved depiction of SOA formation and SOA removal. Specifically, production rates of SOA increased by 3.9 times from the basic VBS, and the efficiency of sinks improving by 3.6 times than the base VBS. This resulted in a more realistic depiction of SOA distribution, more SOA near the surface, with decreased SOA present in the upper troposphere.

3 | Results and discussion

3.1 Spatial structure of tropospheric chemistry effect

What are the effects of coupled tropospheric chemistry on key climate characteristics, such as temperature, clouds, precipitation and winds? The atmosphere was once thought to be essentially chemically neutral until the 1970s when Molina et al. (1974) described the impact of CFC emissions on stratospheric ozone. Models have advanced, and can now capture large sets of organic chemistry. Coupled tropospheric chemistry models are able to have interactive chemistry between these organics with other atmospheric constituents including aerosols (like, sulfate aerosol, salt, dust, etc.). Changes in these aerosols, as mentioned in sec. 1.7, result in a number of direct, indirect and semi-direct effects. These effects are intimately related to surface temperature, cloud changes, precipitation and winds. These atmospheric changes are then further coupled to ocean geochemistry, dynamics, and radiative balance. In

CESM2-WACCM6, there are 5 more components all of which interact leading to complex feedbacks which in turn influence the previously mentioned surface temperature, cloud changes, precipitation and winds. Visualizing the spatial distribution of these parameters provides an insight into the global impacts of this coupled chemistry on climate.

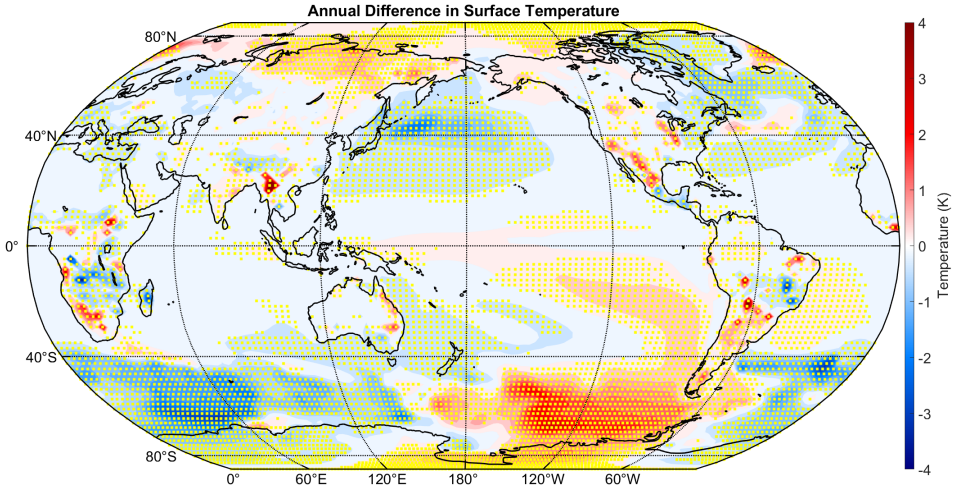

Figure 3.1: Annual mean difference (BW1850 - BWma1850) in surface temperature (K) - Yellow dots indicates regions where there is a statistically significant mean difference.

Figure 3.1 depicts the mean difference in the surface temperature, with reds indicating increases in surface temperature and blues indicating decreases in surface temperature. Surface temperature represents the total effect of various sources and sinks of energy. There are a number of factors that can change the surface temperature in a region, such as cloud cover, surface reflectivity (albedo) and temperature advection.

In the Southern Ocean (between New Zealand and the Southern tip of South America) there are increases of surface temperature of about 2 to 3 K. There is moderate cooling (1 to 2 K) in the Southern Ocean between the tip of South America

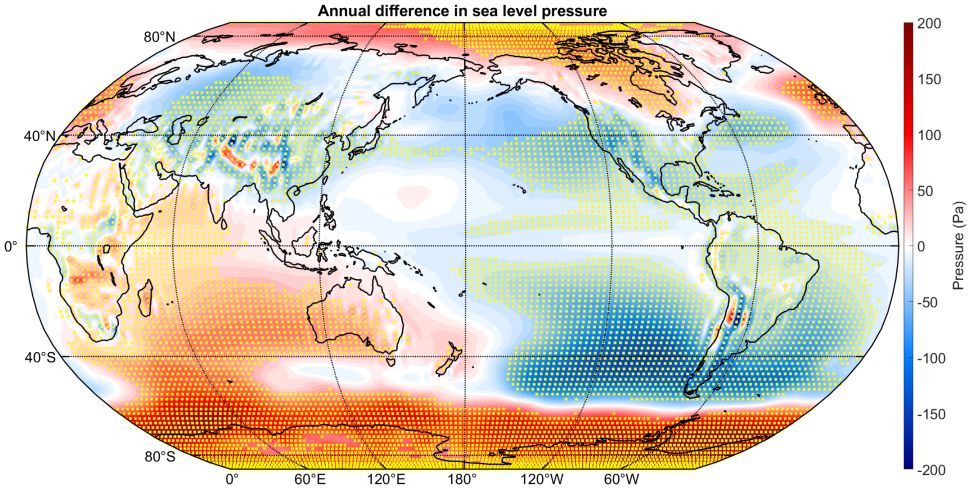

(a)

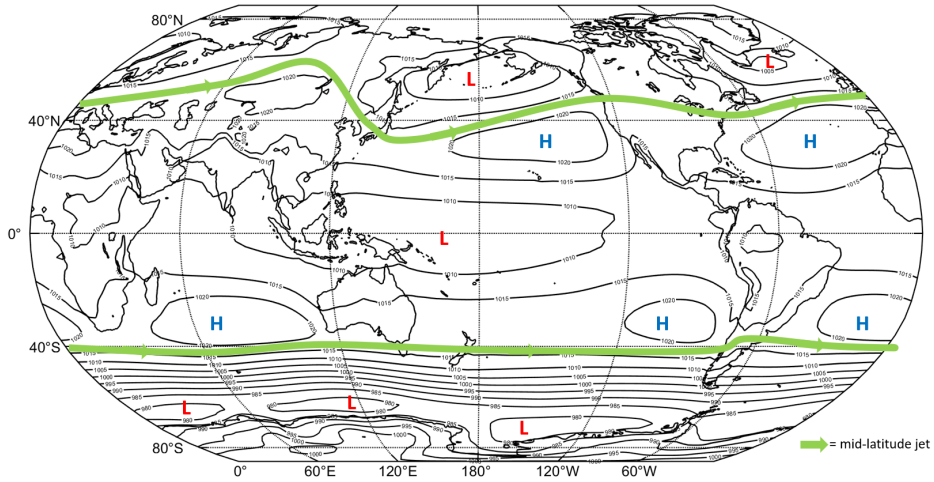

(b)

Figure 3.2: (a) Sea level pressure (Pa) mean difference (BW1850 - BWma1850) and (b) BWma1850 climatology - Yellow dots indicate regions where there is a statistically significant mean difference.

eastward to Australia. In the NH, off the coast of Japan, there is moderate cooling (0.5 to 1.5 K). Another key influence on regional climate is the change in wind, which can be partially captured through the changes in sea level pressure.

Changes in SLP can help indicate regions in which we see the influence of dynamical changes. Figure 3.2a is the mean difference in sea level pressure (SLP), given in units of Pa. Blues indicate decreases in the SLP, while reds indicate increases in the SLP. In the mid-latitudes, in regions where there is an increase in SLP there is more upper-level convergence and descent occurring. In regions where there is a decrease in SLP, there is more upper-level divergence and ascent occurring. Figure 3.2b shows the BWma1850 climatology of sea level pressure along with the approximate location of the mid-latitude jets (in green). Figure 3.2a can be interpreted in terms of geostrophic balance and the climatology in figure 3.2b. In accordance with geostrophic balance, the midlatitude jets form between the boundary of the polar low and subtropical high.

In the Southern Hemisphere between New Zealand eastward to the prime meridian, there is a weakening of the polar low and the subtropical high. These changes indicate a weakening of the meridional pressure gradient with an associated weakening and equatorward shift of the midlatitude jets. In the Southern Hemisphere between New Zealand westward to close to the meridian, there is a weakening of the polar low and a strengthening of the subtropical high. In the Northern Hemisphere, there is a weakening of the subtropical high and the polar low. This also indicates a

weakening and equatorward shift of the midlatitude jets.

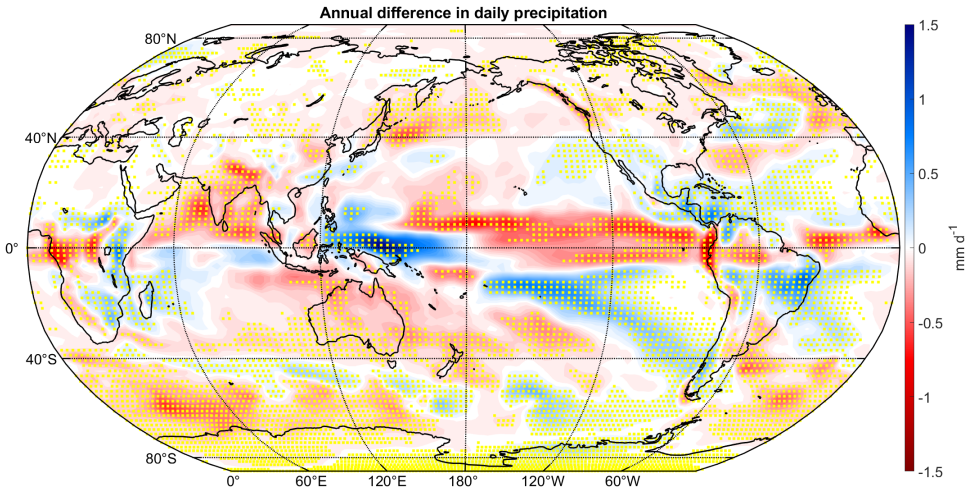

Figure 3.3: Annual mean difference (BW1850 - BWma1850) in daily precipitation (mm d^{-1}) - Yellow dots indicates regions where there is a statistically significant mean difference.

Global precipitation changes are connected to changes in general circulation, and therefore storm track regions. Figure 3.3 is the mean difference of daily precipitation, with blues indicating increases in precipitation and reds indicating decreases in precipitation.

There are significant differences in precipitation around the ITCZ. Just north of the Maritime Continent, there are increases in precipitation of up to 1.5 mm d^{-1}. In the Eastern Equatorial Pacific, there are moderate decreases in precipitation between 0.5 to 1.25 mm d^{-1}. This band of decreased precipitation loosely extends through the Amazon Forest and to Equatorial Africa. The precipitation response indicates a strengthening of the Walker circulation. There are decreases in precipitation in the

equatorial Eastern Pacific, with increases in the equatorial Western Pacific.

The Southern Ocean shows slight increases (up to 0.5 mm d^{-1}) in precipitation between 180° and 60°W. The changes north of the Antarctic sea ice can be related to figure 3.2a, where there is a decrease in the sub-tropical high and associated equatorward shift leading to more ascent. However, in this region over the sea ice, where SLP increases, there is an increased latent heat flux from warming (seen in fig. 3.1) and sea ice melt. The Southern Ocean between 120°E westward to 60°W shows moderate decreases in precipitation (0.1 to 0.75 mm d^{-1}). These changes can be related to figure 3.2a, where we see an increase in SLP, with which we expect anomalous descent. As well, cooling in this region due to increased cloud cover reduces evaporation and hence precipitation.

In the South Pacific, roughly from Samoa to southern Chile, there is a band of increased precipitation up to 0.75 mm d^{-1}. This can be related to an increase in ascent as figure 3.2a shows a decrease in SLP. Decreases in precipitation are seen over the Indian subcontinent, and are associated with increased descent based on figure 3.2a. There is a region of slightly increased precipitation (up to 0.25 mm d^{-1}) in the southwestern Indian Ocean. In the Northern Hemisphere, decreases in precipitation between 0.1 to 0.75 mm d^{-1} occur in the mid-latitudes. Looking off the eastern coast of Japan, there is a decrease in precipitation, associated with increased cloud cover and cooling which is expected to reduce latent heat fluxes in this region.

Straying from the pattern of decreased precipitation in the Northern Hemi-

sphere, increases (0.1 to 0.25 mm d^{-1}) in precipitation occur from Hawaii through the to Rocky Mountains. This can be related to figure 3.2a, where there is a decrease in SLP in this area. There is also a region of precipitation increase (up to 0.5

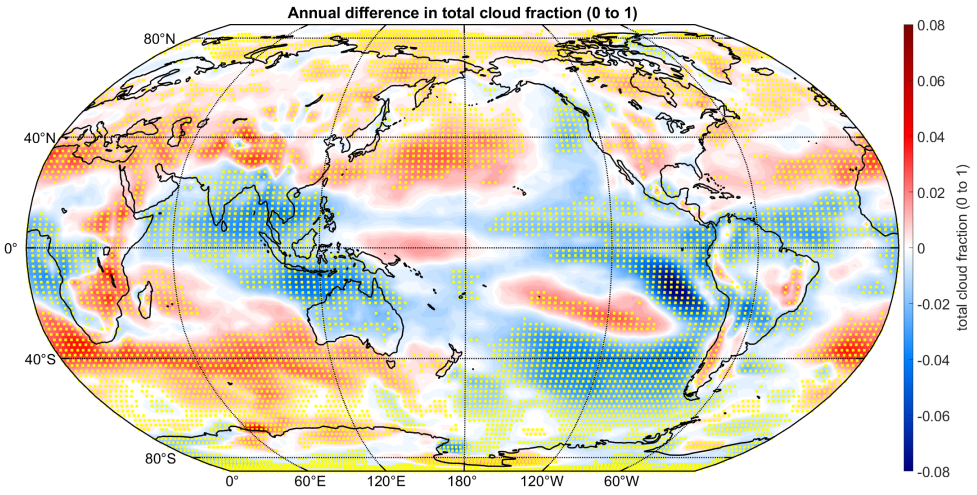

(a)

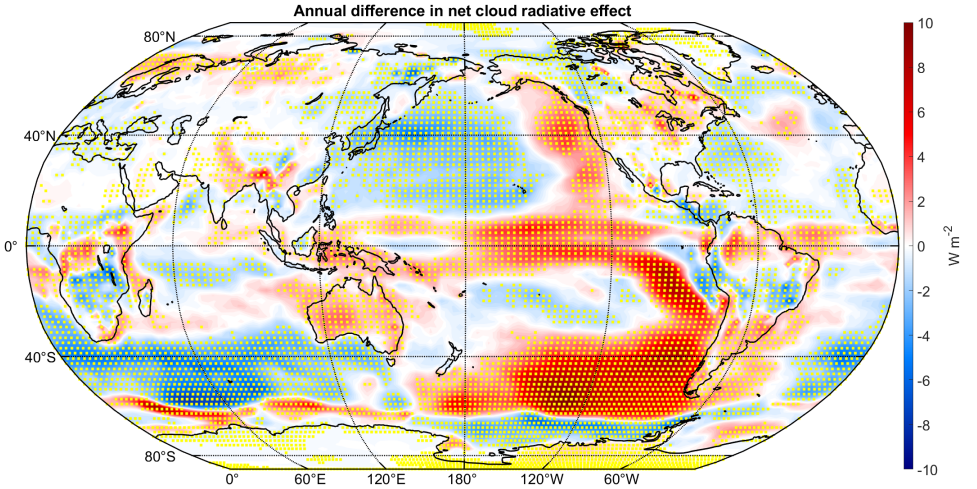

(b)

Figure 3.4: (a) Total cloud fraction and (b) net cloud radiative effect mean differences (BW1850 - BWma1850) - Yellow indicates areas with statistically significant mean differences.

mm d^{-1}) off the coast of Nova Scotia extending into the Grand Banks and the North Atlantic. Again, looking back to figure 3.2a there is a decrease in SLP indicating more ascent is occurring here.

The change in cloud microphysics due to increased organic aerosol can influence the efficiency of precipitation. Liu et al. (2019) suggest that changes due to increased aerosol results in a non-monotonic response on precipitation in convective clouds. Using a model with increasing aerosol concentrations, 1.25×10^{8} particles m^{-3} - pristine, 1×10^{9} particles m^{-3} - polluted, and 1×10^{10} particles m^{-3} - extremely polluted clouds, they found that polluted convective clouds produced the highest rain yield. Extremely polluted clouds produced the least rain yield, and pristine clouds fell in between. This response to aerosol loading may help explain some of the differences in cloud and precipitation distribution.

Changes in cloud fraction and net CRE have a significant influence on the surface energy budget, and hence temperature. Figure 3.4a is the mean difference in total cloud fraction. Figure 3.4b is the mean difference in net cloud radiative effect (net CRE), given in units of W m^{-2}. Blues indicate decreases in the total cloud fraction & net CRE, while reds indicate increases. The net CRE is the sum of the longwave cloud effect and the shortwave cloud effect. Positive values indicate regions where the net CRE contributes to warming, while negative values indicate regions where the net CRE contributes to cooling. Changes in the total cloud fraction are intimately related to net CRE changes. Total cloud fraction does not differentiate the

altitude of clouds. Low clouds (optically thick) contribute to negative CRE, while high clouds (optically thin) contribute to positive CRE. If there is an increase/decrease in total cloud fraction in a region where clouds are typically at a high altitude (deserts), this will contribute to a positive/negative change in the net CRE. If there is an increase/decrease in total cloud fraction in a region where clouds are typically at a lower altitude (oceans), this will contribute to a negative/positive change in the net CRE (Hartmann, 2015).

The Southern Ocean between 0° longitude moving east to 150°E, shows moderate (up to 0.04) increases in the total cloud fraction. In this same region, there are decreases in the net CRE up to -8 W m^{-2}. The Southern Ocean, between 180° and 60°W, shows a moderate (up to 0.04) decrease in the total cloud fraction. In this same region, there are increases in the net CRE of about 2 to 8 W m^{-2}. Relating these changes to figure 3.2a, there is an equatorward shift of the midlatitude jet which contribute to these changes in total cloud fraction and the net CRE. These cloud changes relate to figure 3.1, where there are decreases in the total cloud fraction and increases in the net CRE. This occurs due to sea ice melting without any change in cloud cover. While no sea ice results are presented in this study, the output of this field was assessed. Sea ice area in this region decreases. Low clouds go from having almost no effect on surface temperature to having a substantial cooling effect, i.e. a negative change in CRE.

Significant bands of decreased total cloud fraction are seen in the tropics and

subtropics. One area of decrease which is larger in this band, about 0.06 to 0.08 in total cloud fraction, occurs off the coast of Peru and Chile. There is an associated increase in the net CRE of about 8 to 10 W m^{-2}. Once again it would appear these changes are caused by changes in circulation. The equatorward shift of the jet moved this region into the subtropical dry band, with an enhancement from the orographic effect.

In the NH north of the subtropical band, there are increases in cloud fraction (up to 0.04) throughout up to the North Pole. From Japan to Hawaii up to the Aleutian islands there is a decrease in the net CRE of up to 5 W m^{-2}. To a lesser extent, there is the same pattern off the east coast of North America. This area is associated with a decrease in surface temperature, seen in figure 3.1. The changes to cloud cover can largely be attributed to the SLP changes we see in figure 3.2a; weakening of the subtropical high and increase of the polar low. The northwestern Pacific Ocean has decreases in total cloud fraction of about 0.02. There is an associated increase in the net CRE of about 4 W m^{-2}. Over the North pole, there is slight warming (up to 0.25 K) with no clear mechanism for this warming other than the increase in SLP.

Compared to CRE changes over land, changes in the net CRE over the ocean seem to more directly relate to surface temperature changes. SLP changes do play a role in cloud changes, but do not describe the full picture. As mentioned in sec. 1.7, changes in CCN are also modifying clouds. Further mechanisms for these changes will be discussed in section 3.2.

3.2 Zonal-mean structure of tropospheric chemistry effect

While observing the spatial differences provides a global picture of the impacts of coupled tropospheric chemistry, it hides the changes in the vertical structure of the

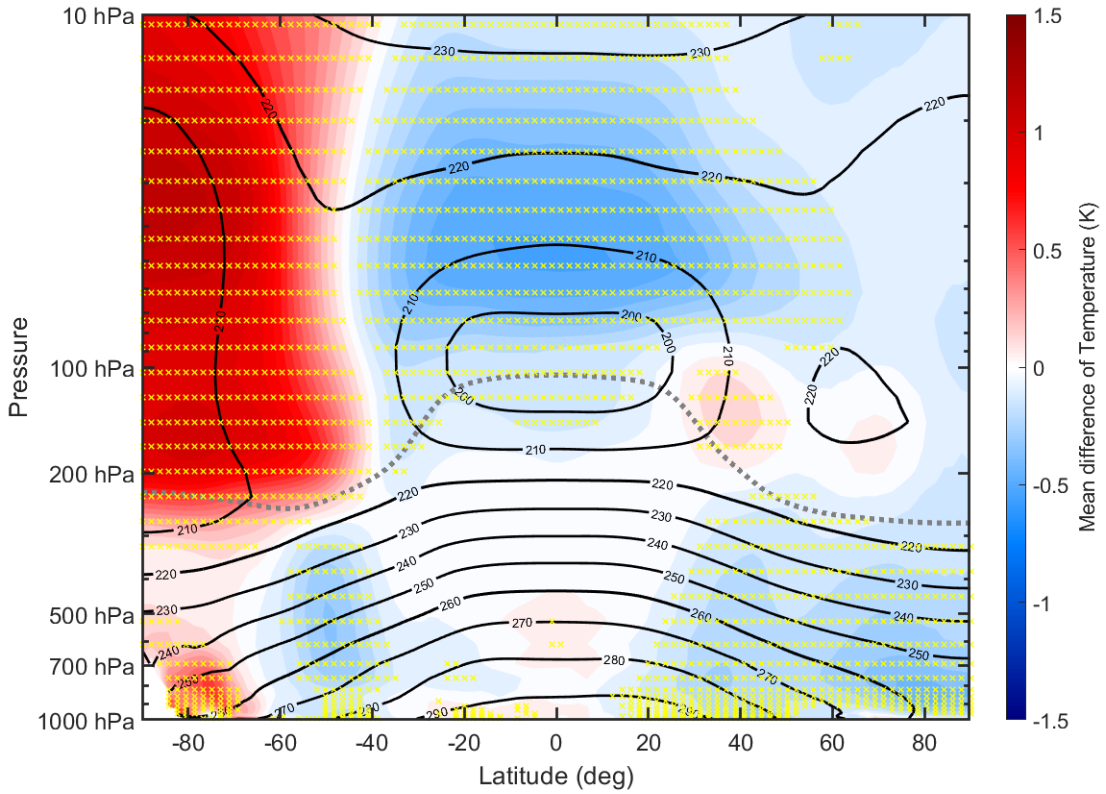

Figure 3.5: Annual mean difference (BW1850 - BWma1850) in atmospheric temperature (K) - The black contours indicate the BWma1850 climatology of air temperature (K), with a contour interval of 10 K. Yellow indicates areas with statistically significant differences. The gray dotted line represents the BWma1850 climatology of the tropopause.

atmosphere. A vertical visual provides a connection between changes seen in the ver-

tical to changes seen in Sec. 3.1. The coupling in this study largely impacts changes in aerosol. The impacts of coupled tropospheric chemistry results in significant changes to the vertical structure of temperature, winds, cloud distribution, etc. To physically interpret these results, it is best to focus on a zonal average structure of the response to coupled tropospheric chemistry.

Figure 3.5 depicts the mean difference of atmospheric temperature, with reds indicating increases in temperature and blues indicating decreases in temperature. There are decreases in temperature throughout most of the Northern Hemisphere, a slight increase in the tropical troposphere (which is not statistically significant) and subtropical stratosphere with a larger decrease in temperature in the tropical stratosphere. In the SH troposphere, there are increasing temperatures in the high latitudes and decreasing temperatures in the midlatitudes. If the meridional temperature gradient decreases an associated weakening of the polar vortex can be expected. In the SH, the meridional temperature gradient is decreasing due to warming near the poles. This does not occur in the NH.

The largest difference in temperature is in the Southern Polar Stratosphere (SPS) (90°S to 45°S), with temperature increases of 1 to 1.5 K. In the Southern Polar Troposphere temperature increases by 0.25 to 0.75 K in the latitude range of 90°S to 60°S. Between 60°S to 40°S in the troposphere, there is a decrease in temperature of about 0.25 K. There is a slight region of increased temperature (0.1 K) in the tropical mid-troposphere between 20°S to 20°N. Around 40°N in the lower stratosphere, there

is an increase of temperature by about 0.1 to 0.25 K. The drivers behind this change need to be further investigated. There is a broad region of decreased temperatures (0.25 to 0.75 K) in the troposphere between 20°N to 90°N. In the stratosphere between 40°S to 40°N, there is a broad region of decreased temperature of 0.1 to 1 K. This region of decreased temperature appears to be due primarily to anomalous dynamical cooling, see figure 3.6.

Figure 3.5 shows significant cooling throughout the troposphere, except in the tropics and Antarctica. Chen et al. (2013) have shown that the jet response to a nearly uniform warming of the troposphere results in a poleward shift. Specifically, they found "a fast poleward shift of the midlatitude eddy-driven winds and the edge of the Hadley cell and a slow equatorward contraction of the upward branch of the Hadley cell and ITCZ". They attribute this result to a reduced midtropospheric Lagrangian potential vorticity (PV) gradient. The tropospheric cooling occurring in this experiment is not nearly as uniform, instead having a sharpening of the temperature gradient equatorward (in NH and SH) in the midlatitudes and a weakening of the temperature gradient poleward in the SH (south of 50°S). In this experiment the localized temperature changes modify the overall tropospheric response. Even with these differences from Chen et al. (2013), these results can be compared qualitatively having the opposite result and mechanisms. Tropospheric cooling can be expected to result in equatorward shifts of the jets, but is modified due to localized temperature changes. This equatorward shift is further reinforced by the warming near Antarctica

as described by Butler et al. (2010).

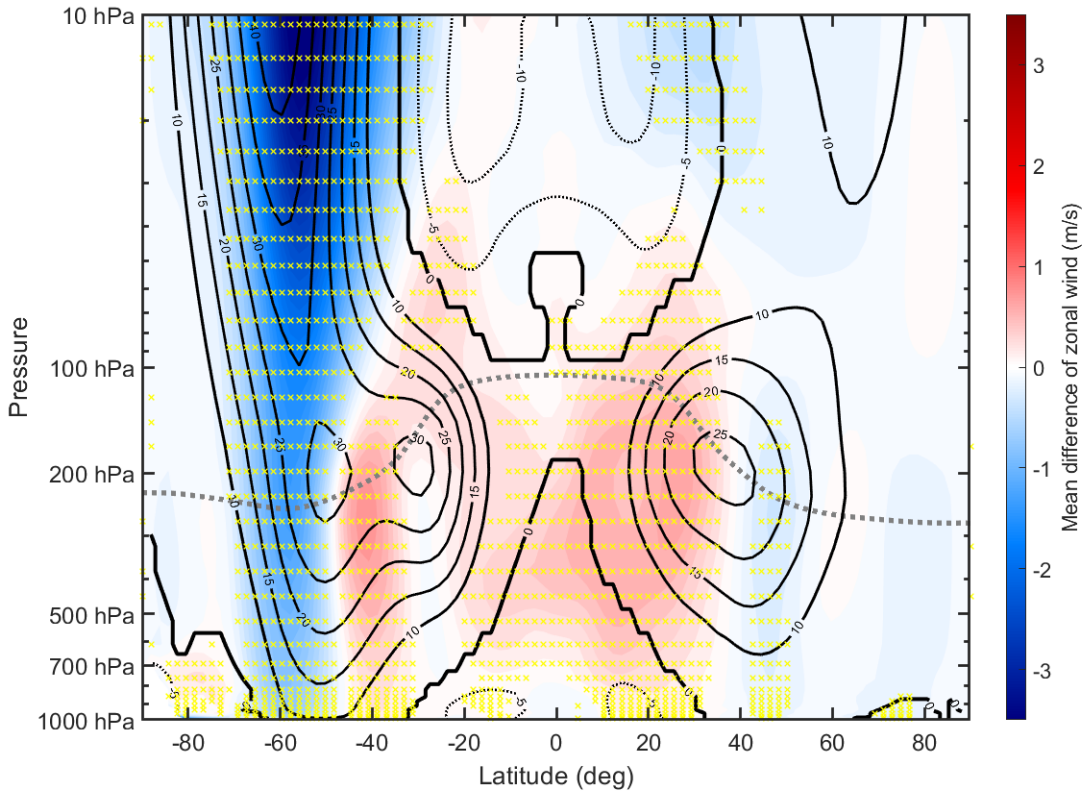

Figure 3.6: Annual mean difference (BW1850 - BWma1850) in zonal wind (m s^{-1}) - The black contours indicate the BWma1850 climatology of Zonal wind (m s^{-1}), contour interval 5 m s^{-1}. Yellow indicates areas with statistically significant differences. The gray dotted line represents the BWma1850 climatology of the tropopause.

Changes in large scale dynamics play a key role in shaping the climate response to coupled tropospheric chemistry, as seen from figure 3.2. Figure 3.6 depicts the mean difference of zonal wind, with reds indicating increases in zonal wind and blues indicating decreases in zonal wind. When the meridional temperature gradient decrease, like in the SH, a weakening of the polar vortex is expected. When zonal wind decreases more descent is expected. With the decrease in zonal wind, there

appears to be changes in baroclinic instability. This is because changes in baroclinic instability relate to changes in negative and positive vorticity advection (NVA/PVA). Areas of NVA/PVA in the NH/SH are associated with surface-level high pressure development, with areas of PVA/NVA in the NH/SH associated with surface-level low pressure development (Holton, 2013). In the SH, decreases in zonal wind result in changes in baroclinic instability (reduced baroclinicity) that increase PVA in the SH.

Between 70°S and 50°S, zonal wind decreases by about 0.5 m s^{-1} at the surface to about 3.5 m s^{-1} in the SPS. These changes in zonal wind result from temperature changes in the troposphere.

An increase (0.5 m s^{-1}) in zonal wind occurs between 45°S and 35°S from the surface to 200 hPa. This region of increase to the north of the jet max, along with the previously mentioned decrease south of the jet max, indicates an equatorward shift in the midlatitude jet.

Between 20°S and 40°N from the surface to the lower stratosphere, there is a broad region of increase in zonal wind. Within this region, between the equator and 40° N, there is a moderate increase in zonal wind (0.5 to 1.5 m s^{-1}). From 40°N to the North Pole and throughout the troposphere and stratosphere, there is a minor decrease in zonal wind (0.1 to 0.5 m s^{-1}). There is not the same stratospheric polar vortex weakening in the NH compared to the SH. This helps explain why the Northern Polar Stratosphere (NPS) does not have the same dynamical warming as

the SPS. This dipole change in wind once again indicates an equatorward shift of the

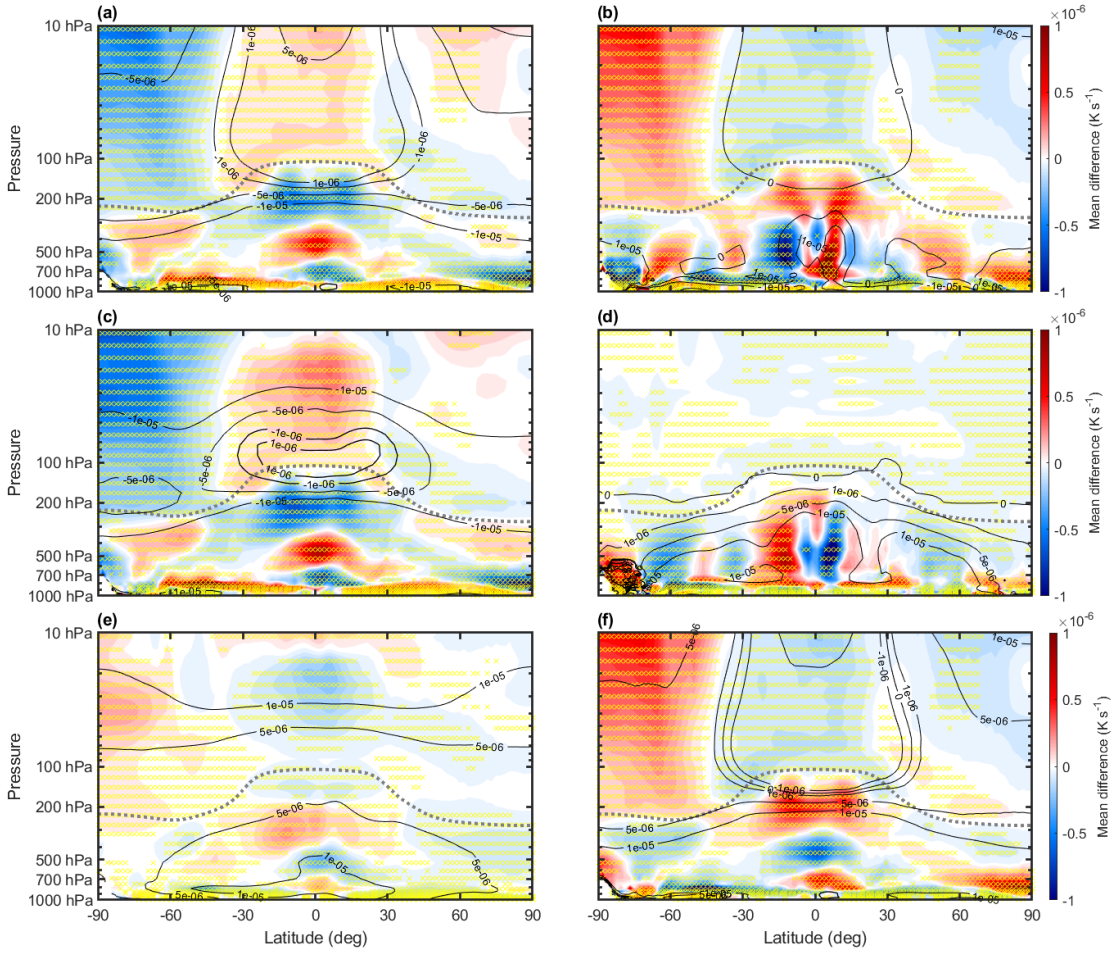

Figure 3.7: Annual mean difference (BW1850 - BWma1850) in heating/cooling rates (K s^{-1}) - Yellow dots indicate areas with statistically significant differences. The gray dotted line represents the BWma1850 climatology of the tropopause. The black contours indicate the BWma1850 climatology. Panel (a) is radiative heating, with climatology contours -5×10^{-6}, -1×10^{-6}, 1×10^{-6}, 5×10^{-6} K s^{-1}. Panel (b) is dynamical heating, with climatology contours $-1 \times 10^{-5}, 0$, 1×10^{-5} K s^{-1}. Panel (c) is longwave cooling, with climatology contours $-1 \times 10^{-5}, -5 \times 10^{-6}$, -1×10^{-6}, 1×10^{-6} K s^{-1}. Panel (d) is latent heating, with climatology contours 0, 1×10^{-6}, 5×10^{-6}, 1×10^{-5} K s^{-1}. Panel (e) is shortwave heating, with climatology contours 5×10^{-6}, 1×10^{-5} K s^{-1}. Panel (f) is dynamical + latent heating, with climatology contours -5×10^{-6}, $-1 \times 10^{-6}, 0$, 1×10^{-6}, 5×10^{-6}, 1×10^{-5} K s^{-1}.

midlatitude jet. Such an equatorward shift was also apparent in the SLP changes discussed previously (Fig. 3.2).

Figure 3.7a depicts the mean difference in radiative heating, with reds indicating increases in radiative heating and blues indicating decreases in radiative heating. The radiative heating rate is calculated by summing the longwave cooling rate (figure 3.7c) and shortwave heating rate (figure 3.7e). Many of the changes in fig. 3.7a are dominated by the changes in longwave cooling (fig. 3.7c). These quantities are a portion of the Q term in the temperature tendency equation (eq. 1.2.). Figure 3.7c shows the mean difference in the longwave cooling rate, with reds indicating increases in longwave cooling and blues indicating decreases in longwave cooling. Figure 3.7e shows the mean difference in the shortwave heating rate, with reds indicating increases in shortwave heating and blues indicating decreases in shortwave heating. All of the climatological values of radiative heating are negative in most of the troposphere (diabatic cooling). This means any positive change in the troposphere shows a decrease in radiative cooling and negative changes in the troposphere show an increase in radiative cooling.

Figure 3.7b depicts the mean difference in dynamical heating. Blues indicate regions where the dynamical heating terms are decreasing, while the reds indicate regions where the dynamical terms are increasing. This quantity corresponds to the advective terms in the thermodynamic tendency equation (eq. 1.2).

Figure 3.7d shows the mean difference in latent heating. Blues indicate re-

gions where latent heating is decreasing, while reds indicate regions where latent heating is increasing. When evaporation or melting occurs, it cools the surrounding atmosphere. When condensation or freezing occurs, it heats the surrounding atmosphere. As there is very little water in the stratosphere, the changes in latent heating are mainly confined to the troposphere.

Figure 3.7f depicts the mean difference in dynamical heating and latent heating combined. Blues indicate regions of decrease, while reds indicate regions of increase. The combination of figures 3.7b and 3.7d is what is shown in fig. 3.7f. The dynamical terms are the sum of the horizontal and vertical advection terms in eq. 1.2. The terms "adiabatic" and "dynamical" are synonymous, although adiabatic sometimes (but not in this analysis) is understood to refer only to the vertical advection term. Figure 3.7f, the dynamical + latent heating, is nearly equal and opposite to fig. 3.7a, the radiative heating.

In the SPS there is a region of increased longwave cooling, which is balanced by dynamical heating changes (fig. 3.7b). The increase longwave cooling in the SPS can be compared to fig. 3.7b and 3.7e to show that the warming trend seen there is largely due to dynamical warming (up to 2×10^{-6} K s^{-1}) as opposed to an increase in ozone absorption. Keeble et al. (2014) provide evidence that when stratospheric ozone is modified directly, temperature changes in the lower stratosphere are mainly due to shortwave heating. The shortwave heating (due to ozone absorption) in the SPS, is an order of magnitude less than the dynamical warming. This indicates the

increase in atmospheric temperature seen in this region is primarily a consequence of dynamical changes originating from the troposphere. The changes in ozone barely modify the warming in this region.

In the Antarctic troposphere, between the South pole and 75 °S, there is dynamical cooling. This is counteracted by latent heating (fig. 3.7d), which may be a result of a small positive cloud feedback which requires further investigation.

In the lower troposphere there are large decreases in radiative cooling from between 60°S to 5°S and 10°N to near the North Pole. This is associated with a decrease in dynamical heating. Here there are decreases in longwave cooling in the lower troposphere. Such changes are expected with cooling in the lower troposphere. The reduction in longwave cooling nearly balances the reduction in dynamical heating here. Roughly in this same layer, increases in latent heating (3.7e) occur, implying more condensation is occurring.

In the tropical mid-troposphere, we see decreases in the radiative cooling rate between 600 hPa and 350 hPa. This is paired with increases in the tropical upper troposphere. The pattern of shortwave warming and cooling in the tropical troposphere is being further investigated, but may be related to the increase in SOA. Minor increases in radiative heating are seen in the tropical stratosphere, and decreases in radiative cooling are seen in the SPS. These changes are almost entirely explained in longwave (figure 3.7c) heating. The longwave cooling decreases in the tropical stratosphere do not overpower the shortwave warming decreases that occur in this

region.

Between 30 °S and 10 °S, in the tropical troposphere there are increases in latent heating (fig. 3.7d). These are counteracted by dynamical cooling, between 400 hPa and 700 hPa, seen in fig. 3.7f. In this region, between 400 hPa up to the tropopause, latent heating and dynamical warming lead to combined warming seen

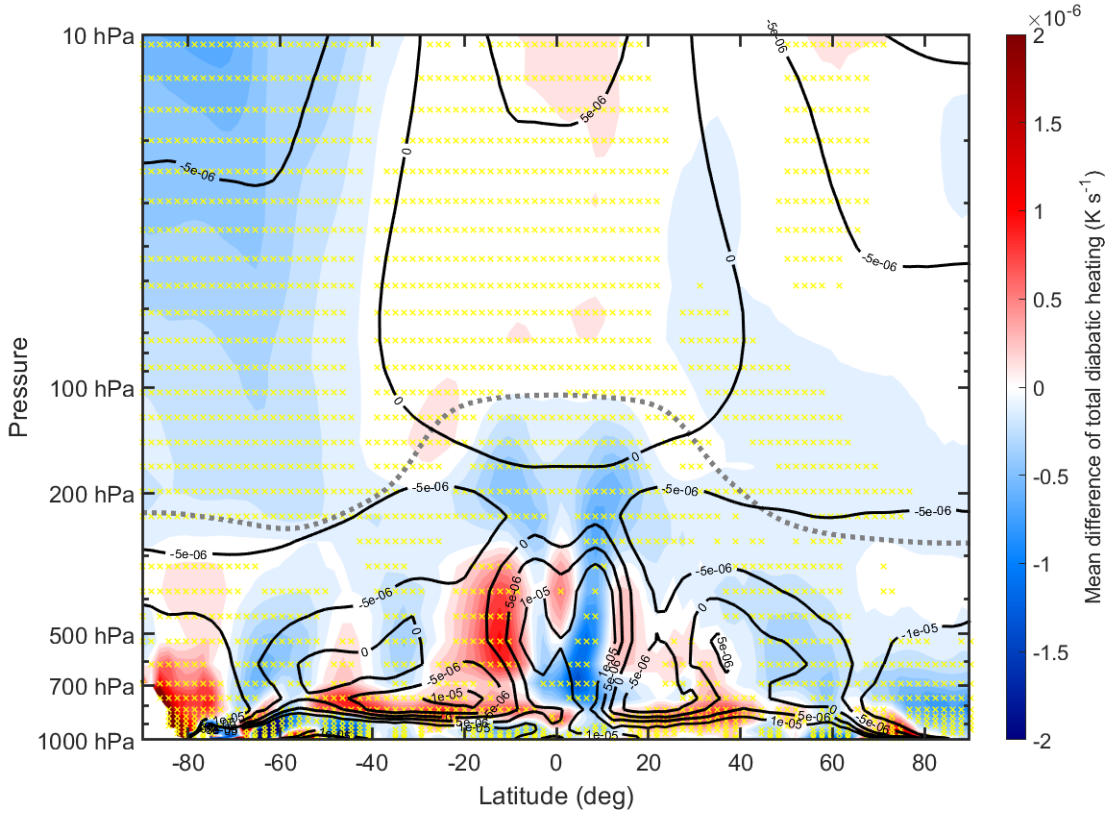

Figure 3.8: Annual mean difference (BW1850 - BWma1850) in total diabatic heating (K s^{-1}) - The black contours indicate the BWma1850 climatology of total diabatic heating (K s^{-1}), contours of -1×10^{-5}, -5×10^{-6}, 0, 1×10^{-6}, 5×10^{-6}, 1×10^{-5} K s^{-1}. Yellow dots indicates areas with statistically significant differences. The gray dotted line represents the BWma1850 climatology of the tropopause.

in figure 3.7f.

There is a large increase, up to 1×10^{-6} W m^{-2}, in radiative cooling in the NH troposphere starting at 500 hPa and increasing to near the surface at the North Pole. This appears to be one driver in the hemispheric difference in tropospheric atmospheric temperature, see figure 3.5. These changes appear to arise from the increase in dynamical heating in this region. This relates to the increase in SLP (fig.

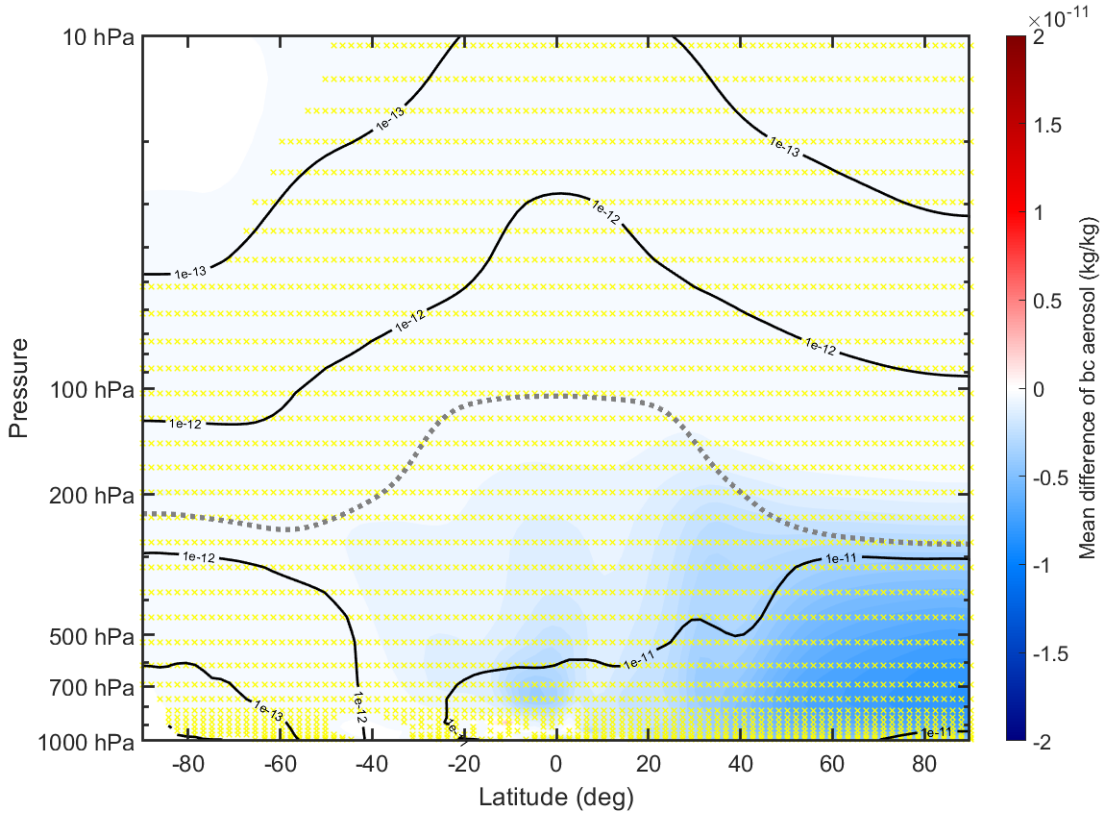

Figure 3.9: Annual mean difference (BW1850 - BWma1850) in black carbon aerosol (BC) (kg kg^{-1}) - The black contours indicate the BWma1850 climatology of BC, with contours 1×10^{-11}, 1×10^{-12}, and 1×10^{-13} kg kg^{-1}. Yellow dots indicates areas with statistically significant differences. The gray dotted line respresents the BWma1850 climatology of the tropopause.

3.2) with an associated anomalous descent and adiabatic warming.

Figure 3.8 depicts the mean difference in the total diabatic heating with latent heating included, with reds indicating increases in total diabatic heating and blues indicating decreases in total diabatic heating. The total diabatic heating rate is calculated by summing the shortwave, longwave, and latent heating rates. This represents the total Q term in the temperature tendency equation (eq. 1.2).

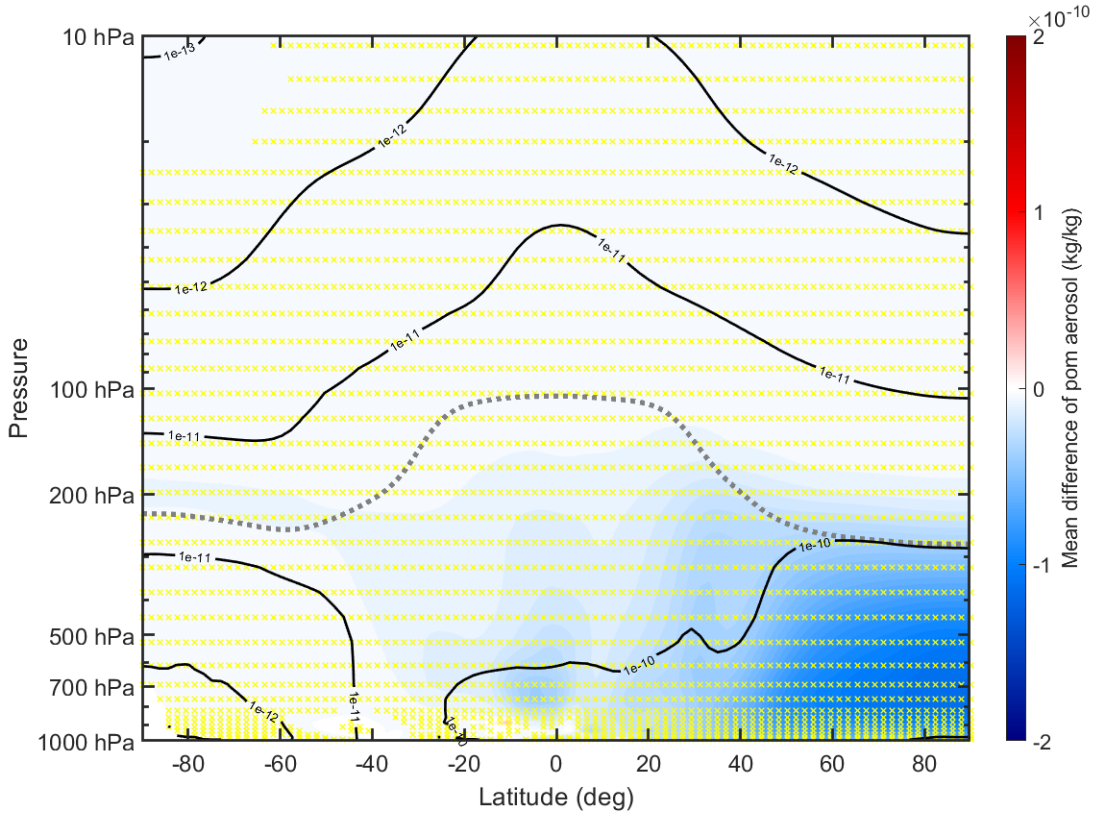

Figure 3.10: Annual mean difference (BW1850 - BWma1850) in primary organic matter aerosol (POM) (kg kg^{-1}) - The black contours indicate the BWma1850 climatology of POM, with contours 1×10^{-11}, 1×10^{-12}, *and* $\times 10^{-13}$ $kg\ kg^{-1}$. Yellow dots indicates areas with statistically significant differences. The gray dotted line represents the BWma1850 climatology of the tropopause.

The changes in total diabatic heating largely mirror the changes seen in the

longwave heating in the lower troposphere (below 700 hPa). The influence of latent heating is most pronounced nearby the ITCZ. Increases in total diabatic heating between 20°S and 10°S, present from 700 hPa to 300 hPa, largely arise from latent heating. In this same altitude band, between 10°S and 10°N decreases in latent heating are the biggest influence on the total diabatic heating rate. In the upper tropical troposphere, the main influence on the total diabatic heating is longwave cooling. Only in the NH troposphere is there a region where a reduction in shortwave heating slightly offsets the reduction in longwave cooling (between 500 to 300 hPa).

Figure 3.9 depicts the mean difference in black carbon aerosol (BC). Blues indicate regions where BC is decreasing, and reds indicate regions where BC is increasing. BC has been classified as an absorbing aerosol (AA, as defined in sec. 1.7.3). BC can absorb incoming shortwave radiation and burn off clouds, also known as the semi-direct effect. BC is considered to contribute to climate warming, though the exact magnitude of this effect is still uncertain (Menon et al., 2002).

The BWma1850 climatology of BC peaks in the high latitudes, which initially may seem counterintuitive. Around 1850, Europe, the UK, and North America were going through rapid industrialization. Together these regions likely produced more than 50% of the global BC emissions. BC emissions were about 1000 Gg yr^{-1}, with the majority coming from biofuels and a smaller portion arising from coal consumption (Bond et al., 2007).

There is decreased BC throughout most of the atmosphere, with the largest

decreases occurring towards the North Pole. Relating this to figure 3.7e, the decreases in BC appear to decrease the shortwave heating in the NH. Overall, these decreases are approximately -20% to -60%.

Figure 3.10 shows the mean difference in primary organic matter aerosol (POM). Blues indicate regions where POM is decreasing, and reds indicate regions where POM is increasing. POM, as opposed to BC, is not strictly defined as an

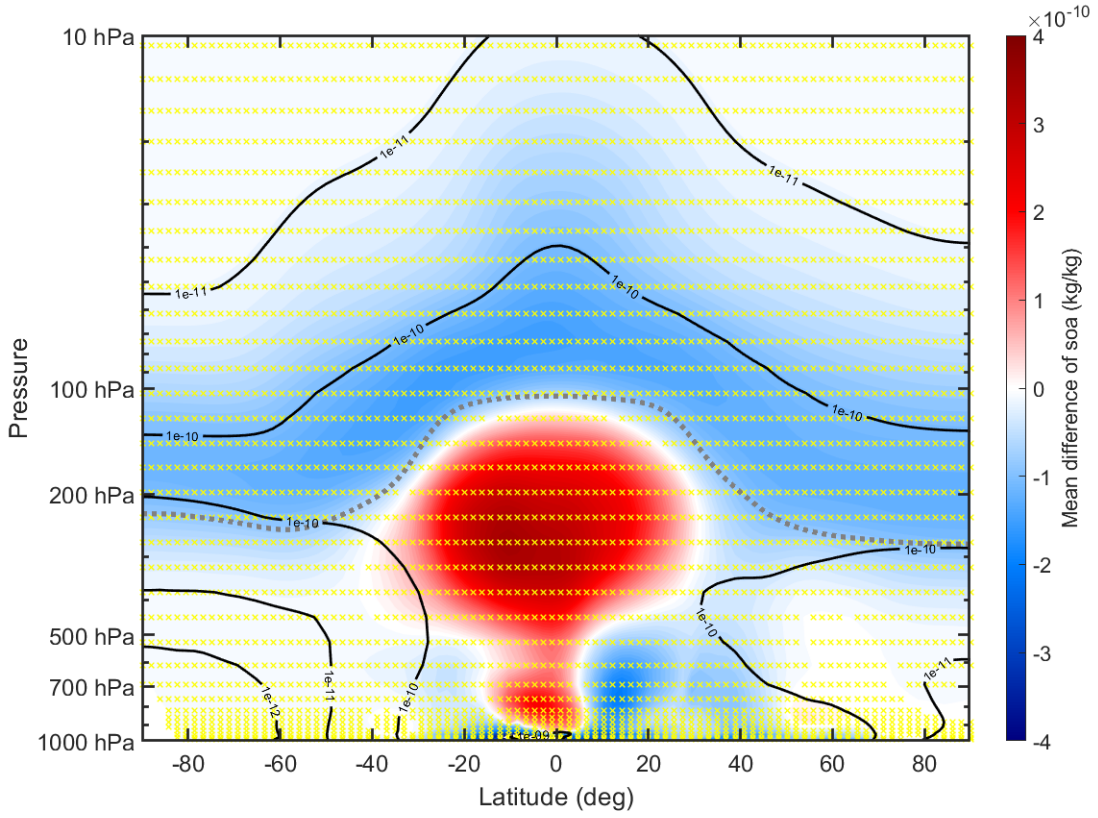

Figure 3.11: Annual mean difference (BW1850 - BWma1850) in secondary organic aerosol (SOA) (kg kg^{-1}) - The black contours indicate the BWma1850 climatology of SOA, with contours 1×10^{-10}, 1×10^{-11}, and 1×10^{-12} kg kg^{-1}. Yellow indicates areas with statistically significant differences. The gray dotted line represents the BWma1850 climatology of the tropopause.

AA. This largely has to do the POM definition. They are considered aerosols that are directly emitted from diesel and gasoline exhaust, and biomass burning (both anthropogenic and natural). They can then act as nuclei for SOA, or they can become internally mixed with black carbon. They can also be internally mixed with sulfate aerosol, which typically scatters more. So depending on the aging that occurs they can act more like absorbing aerosols, or more like scattering aerosols (Song et al., 2007). In the context of this study, it appears POM influence occurs in combination with BC.

Just like in fig. 3.10, there are reductions in POM throughout most of the model. The decreases in POM are larger in the NH than in the SH. These decreases in POM are about -30% to -80%. In combination with the BC changes (figure 3.10e), they help describe why there is a hemispherical difference in shortwave tropospheric heating (fig. 3.7e). Figures 3.9 and 3.10 help describe the difference in shortwave heating, the following figure appears to be the main driver of chemical differences between the configurations.

Figure 3.11 is the mean difference in secondary organic aerosol (SOA). Blues indicate regions where SOA is decreasing, and reds indicate regions where SOA is increasing. The VBS set of chemistry added to WACCM6 significantly impacts the aerosol loading of SOA. Pure SOAs typically scatter incoming radiation, and increases in SOA burden represent a negative radiative forcing in future climate scenarios (Zhu et al., 2017). That being said, SOAs are also known to be absorbing aerosols if

interally mixed with BC, and can enhance the direct aerosol effect (Zhang et al., 2018). Indirect effects of SOA on cirrus clouds have also been examined by Zhu et al. (2020) with a large uncertainty, and they estimate a 0.02 +/- 0.04 W m^{-2} historical radiative forcing due to increased cirrus cloud formation. Those are the radiative influences of SOA, but they also significantly impact the chemistry in the atmosphere. Understanding how aerosol parameterization influences the fraction of absorbing SOA versus scattering SOA is crucial.

The largest increases (1×10^{-10} kg kg^{-1} to 3×10^{-10} kg kg^{-1}) of total SOA are seen in the tropics between 35°S to 30°N from 500 hPa to 150 hPa. These increases amount to a 300 % increase in SOA. The VBS mechanism for SOA formation leads to a large consumption of various radical species (OH, NO_3, NO, NO_2 and Cl). BVOCs and VOCs do consume ozone as well, though not as readily as the previously mentioned radicals. Reductions in these chemical species can influence the HOx, NOx, and ClOx catalytic cycles described in sec. 1.8. It appears that ozone in the troposphere has a longer lifetime due to reduced chemical destruction.

Moderate SOA increases (up to 50% enhancement) occur in the lower troposphere between 45°S to 35°S, 15°S to 5°S, 23°N to 27°N, and 50°N to the North pole. They are not easily visible in the figure due to the over saturation of the tropical increase. Elsewhere in the troposphere reductions in SOA of up to

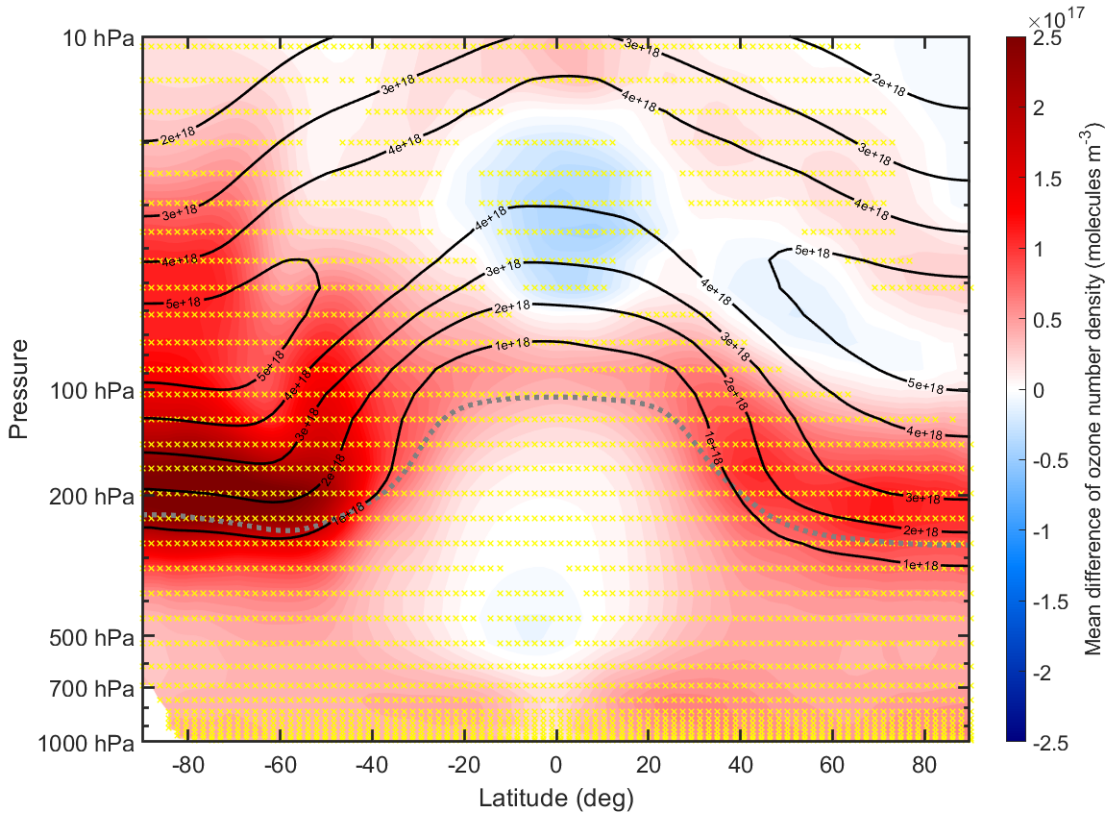

Figure 3.12: Annual mean difference (BW1850 - BWma1850) in ozone (molecules m^{-3}) - The black contours indicate the BWma1850 climatology of ozone (molecules m^{-3}), contours 1×10^{18} molecules m^{-3}. Yellow dots indicates areas with statistically significant differences. The gray dotted line represents the BWma1850 climatology of the tropopause.

-80% are present. In the lower troposphere, though the SOA plot doesn't show increases everywhere, there are still IVOC reactions occurring which contribute to the formation of ozone. This reaction is described in section 1.6.2.

The changes in SOA result in a number of chemical changes in the troposphere and in the stratosphere. The difference in ozone can be partially explained by SOA chemistry occurring in the BW1850 configuration.

Figure 3.12 is the mean difference in ozone number density. Blues indicate regions where ozone is decreasing, while reds indicate regions where ozone is increasing. Dynamical and chemical changes between the configurations leads to the pattern of ozone seen in this figure.

Ozone is decreasing by about 0.5×10^{17} molecules m^{-3} in the mid-stratosphere over the tropics. The mechanisms involved here are currently being investigated, but it does appear to influence the pattern of ozone heating indicated by figure 3.12. The decreases in ozone reduce temperature, and the dynamical cooling in this area further cools the region.

There is also a very slight decrease in ozone between the 20°S to 10°N in the mid-troposphere of about 0.1×10^{17} molecules m^{-3}. This can be related to the changes in SOA (figure 3.15), due to the increased SOA production in this region. Ozone readily reacts with BVOC/VOCs, though this is the only part of the troposphere that experiences a decrease in ozone.

In the NH lower stratosphere, between 20°N to 90°N, there are increases in ozone of about 1.5×10^{17} molecules m^{-3} (about 5 to 10%).

In the SPS and upper troposphere, there are increases of ozone between 1.5×10^{17} to 3.0×10^{17} molecules m^{-3}. This translates to about a 3 % increase of ozone in the SPS with between a 10-20 % increase of ozone in the upper troposphere. Warming (see fig. 3.7b) in the SPS likely leads to fewer PSCs forming meaning fewer heterogeneous removal reactions (see sec. 1.9.5). The ozone does lead to slightly more

ozone heating, as indicated by figure 3.7e, but as discussed above this is likely not the

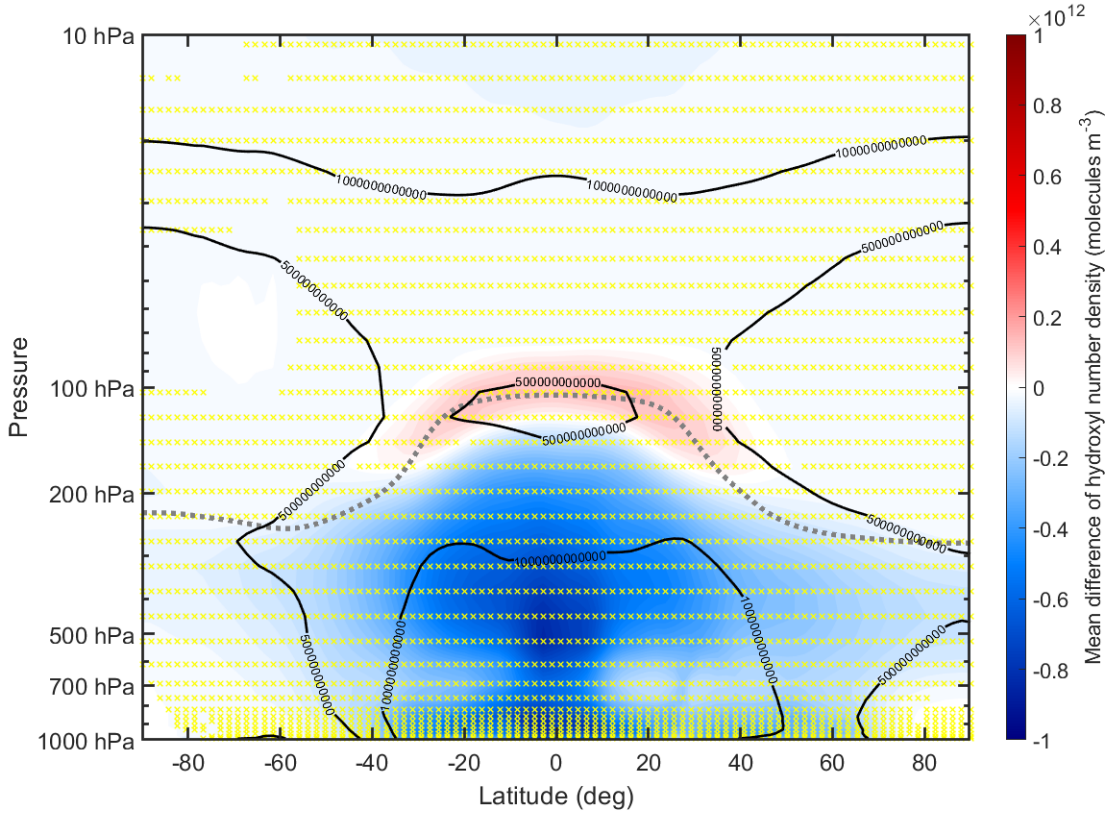

Figure 3.13: Annual mean difference (BW1850 - BWma1850) in OH (molecules m^{-3}) - The black contours indicate the BWma1850 climatology of hydroxyl (molecules m^{-3}), contours 1×10^{11}, 5×10^{11}, 1×10^{12}, and 5×10^{12}. Yellow indicates areas with statistically significant differences. The gray dotted line represents the BWma1850 climatology of the tropopause.

primary cause of warming in the SPS.

Ozone increases in the NH are confined to the tropopause layer near 200 hPa, and there is little ozone change, and even decreases in the stratosphere around 100 hPa. The SH in contrast has increases throughout the stratosphere.

This difference in ozone between hemispheres is partially due to the partitioning of HNO_3 in the gas and condensed phases (Nitric Acid Trihydrate (NAT)) (seen in figure 3.19a & b), and STS ($H_2SO_4/HNO_3/H_2O$ solution) , caused by dynamical warming in the SPS.

Figure 3.13 depicts the mean difference in number density of hydroxyl radical. Blues indicate regions where hydroxyl is decreasing, while reds indicate regions where hydroxyl is increasing. The changes seen in hydroxyl represent an example of how the inclusion of the VBS oxidation reduces the total pool of radicals. There are two main sources of OH in the troposphere. The lesser source of OH radicals comes from reaction SR5 (see sec. 1.9.2). The larger source of atmospheric OH comes from OH recycling from its reaction products (Li et al., 2018). OH is highly reactive with many atmospheric species, so it is difficult to model. As well, the exclusion of HONO chemistry in both configurations may be playing a significant role in the resultant OH.

There are large decreases (20% to 66%) in OH throughout the troposphere, with one region of slight increase around the tropical tropopause. The reduction in hydroxyl, can partially explain the increase in ozone. Referring back to section 1.9.2, we can see how reactions SR5 to SR7 results in ozone removal. If there is less hydroxyl present, than this pathway is less active. The inclusion of the VBS chemistry leads to greater consumption of OH. Looking to figure 3.11, the region with the maximum decrease in hydroxyl is also the region with the largest production of SOA. Without

as much hydroxyl present the lifetime of ozone throughout most of the troposphere and lower stratosphere is increased due to reduced chemical destruction. This is just one example of the consumption of atmospheric oxidizers due to the BVOC/VOC oxidation treatment. Other chemical species, like CLOx and NOx, are also reduced further increasing ozone's lifetime in the troposphere and stratosphere.

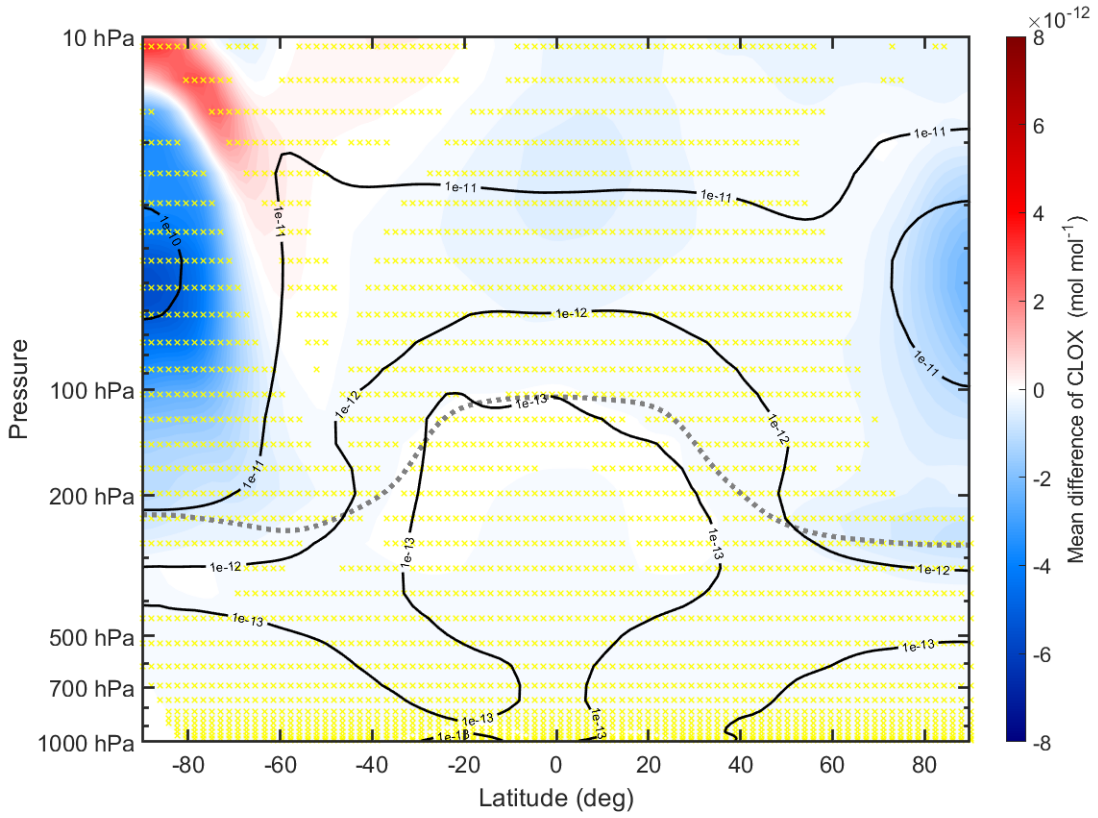

Figure 3.14: Annual mean difference (BW1850 - BWma1850) in ClOx (mol mol^{-3}) - The black contours indicate the BWma1850 climatology of ClOx (mol mol^{-1}), contours 1×10^{10}, 1×10^{11}, 1×10^{12}, and 1×10^{13}. Yellow indicates areas with statistically significant differences. The gray dotted line represents the BWma1850 climatology of the tropopause.

Figure 3.14 is the mean difference in ClOx. Blues indicate regions where

ClOx is decreasing, while reds indicate regions where ClOx is increasing. ClOx is

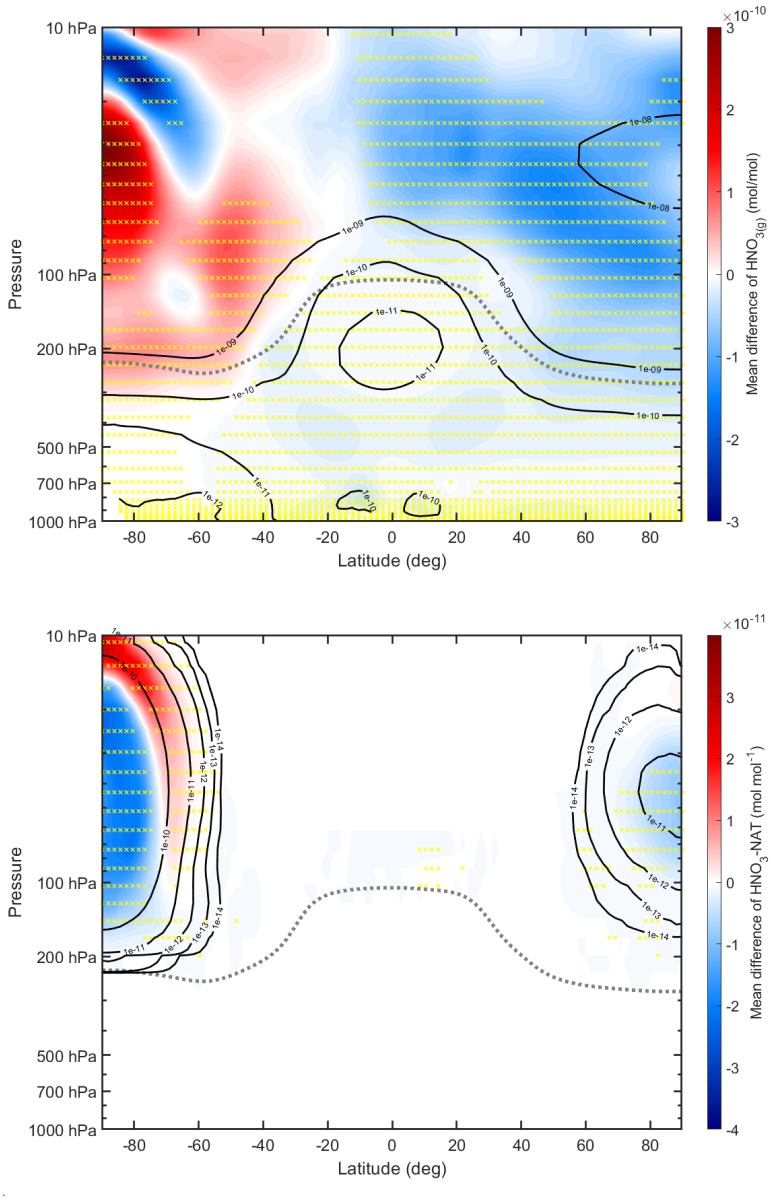

Figure 3.15: (a) HNO_3 gas and (b) HNO_3 NAT mean differences (BW1850 - BWma1850) - The black contours indicate the BWma1850 climatology of HNO_3 gas and HNO_3 NAT, with contours 1×10^{-8}, 1×10^{-9}, 1×10^{-10}, 1×10^{-11}, and 1×10^{-12} for HNO_3 gas and contours 1×10^{-10}, 1×10^{-11}, 1×10^{-12}, 1×10^{-13}, and 1×10^{-14} for HNO_3 NAT. Yellow indicates areas with statistically significant differences. The gray dotted line represents the BWma1850 climatology of the tropopause.

the sum of Cl, ClO, HOCl, $2Cl_2$, $2Cl_2O_2$, and OClO. This figure is an example of a feedback that occurs on ozone formation due to the warming in the SPS. From section 1.9.4, reactions SR20 through SR28 show the impact that these species have on ozone destruction. The ClOx catalytic destruction cycle is an important pathway currently due to it's connection to CFCs. Still even in this experiment, with emissions fixed to 1850 (before CFCs), any natural emissions of Cl atoms can influence ozone distribution. In the BW1850 case, much of the naturally occurring methyl halogens are being consumed in the tropopshere before they can impact the SPS ozone.

There are minor decreases in ClOx throughout most of the troposphere and stratosphere. The largest decreases in ClOx occurs in the SPS, where there is a reduction of ClOx by about 6×10^{-12} to 8×10^{-12} mol mol^{-1}. This is associated with the dynamical warming that occurs in the SPS (see figures 3.7b and 3.5). The ClOx catalytic loss cycle is connected to PSCs and HNO_3 as seen by reaction SR32 in section 1.9.5. With the increase in temperature in the SPS fewer HNO_3-PSCs form, meaning fewer heterogeneous reactions that contribute to ozone loss. Futhermore, the pool of Cl (from biomass burning, fungal species, etc.) is reduced due to the increased consumption of this species due to SOA chemistry. This figure in combination with figure 3.15 shows how the dynamical warming leads to a positive feedback in ozone production in the SPS.

Figure 3.15a is the mean difference in HNO_3 gas. Figure 3.15b is the mean difference in HNO_3 NAT. Blues indicate regions where HNO_3 gas and HNO_3 NAT are

decreasing, and reds indicate regions where HNO_3 gas and HNO_3 NAT are increasing. The influence of these species on ozone destruction was described in section 1.9.5.

Figure 3.15a shows an increase of HNO_3 in the gas phase in the SPS, with an associated decrease in HNO_3 NAT in the condensed phase. This does not occur in the NPS, with both species reduced here. The hemispheric difference in stratospheric ozone can be partially explained with figures 3.15a & 3.15b. The dynamical warming,

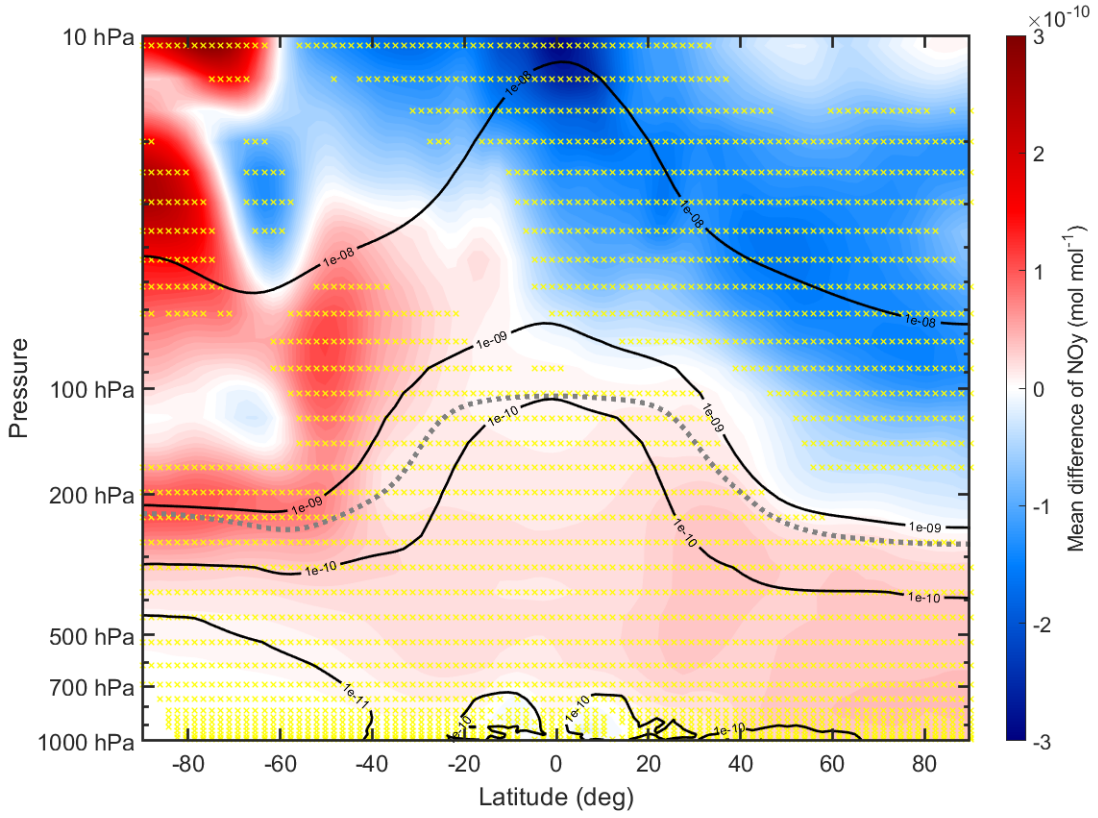

Figure 3.16: Annual mean difference (BW1850 - BWma1850) in NOy (mol mol^{-3}) - The black contours indicate the BWma1850 climatology of NOy, with contours 1×10^{-8}, 1×10^{-9}, 1×10^{-10}, and 1×10^{-11}. Yellow dots indicates areas with statistically significant differences. The gray dotted line represents the BWma1850 climatology of the tropopause.

seen in figure 3.7b, leads to warmer temperatures in the SPS. Typically HNO_3-NAT PSCs form in temperatures below 195 K, with the more destructive type II PSC forming in temperatures below 190 K (Finlayson-Pitts et al., 1999). With a warmer SPS, fewer PSCs of these types can form. This leads to reduced ozone destruction. A related quantity NOy (figure 3.16), which includes HNO_3, has influences on cloud formation and relates back to the changes in tropospheric temperature (figure 3.5).

Figure 3.16 is the mean difference in NOy. Blues indicate regions where NOy is increasing, and reds indicates regions where NOy is decreasing. NOy is the total nitrogen, consisting of; N, NO, NO_2, NO_3, $2N_2O_5$, HNO_3, HO_2NO_2, organic nitrates, and NH_4NO_3. The key constituent in this is the organic nitrate. In the analysis, it was not possible to separate organic nitrates so this is the best proxy. A species which is typically considered part of the total nitrogen budget that is not included in both configurations is HONO. There may be a bias due to the exclusion of this species. HONO can impact the pool of NO_X, impacting the NO_3 budget and hence organic nitrate formation.

The VBS mechanism also applies to organic nitrate. BVOC/VOC reacts with a number of nitrate species to form organic nitrates. Just like SOA, these organic nitrates can condense into aerosol.

Organic nitrates aerosols' impacts were discussed in sec. 1.8.3, and have a negative radiative effect as the surface. They do not act efficiently as CCN (Ng et al., 2017). Focusing on the changes in the troposphere, there are increases in NOy

throughout with more NOy occurring in the Northern Hemisphere. It is possible that a portion of the differences in NOy arise from the organic nitrate component. There is a strong spatial correspondence between the shortwave heating changes (see fig. 3.7e) and the longwave cooling changes (see fig. 3.7c), below 700 hPa and between 60°S to 5° and 10°N to near the North Pole. This suggests that the changes seen in figure 3.8, the total diabatic heating, are potentially influenced by increased organic

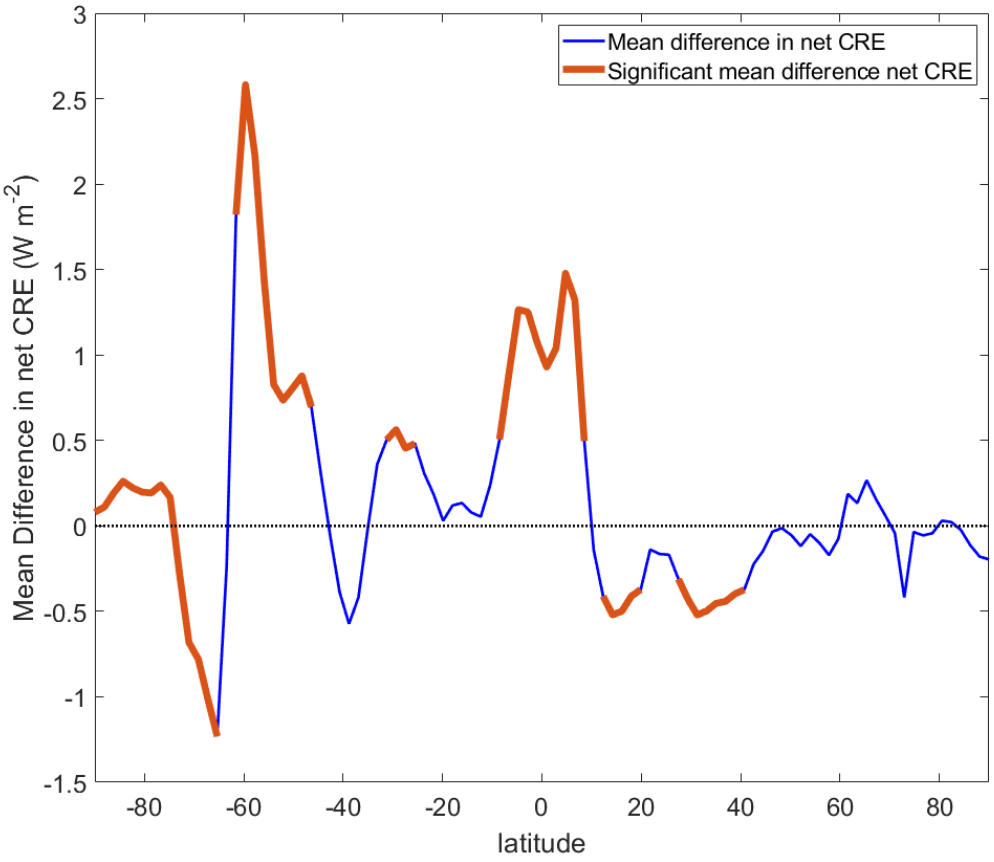

Figure 3.17: Annual mean difference (BW1850 - BWma1850) in net cloud radiative effect (W m^{-2}) - The blue indicates the mean difference in CRE, while the red sections of the line are where the zonal net CRE is statistically significant. The gray dotted line is the zero-line.

nitrate in the NH. This tropospheric cooling then results dynamical changes, which includes the equatorial jet shifts. The resultant dynamical heating changes (fig. 3.7b) end up being quantitatively greater than the changes in latent heating (fig. 3.7d). It is another reason why there is a hemispheric difference in atmospheric temperature.

Beyond the chemical and dynamical changes seen in previous figures, there are changes in cloud distribution as well. These changes arise from and potentially feed back on the dynamical changes.

Figure 3.17 shows the zonal mean difference in CRE. As mentioned regarding figure 3.4, high clouds tend to trap outgoing longwave radiation (thus heating the surface), while low clouds tend to reflect incoming shortwave radiation (thus cooling the surface). The net CRE is a sum of the longwave cloud radiative effect and the shortwave cloud radiative effect. Positive values indicate regions where clouds have a warming effect, while negative values indicate regions clouds have a cooling effect. If there is a decrease in low cloud and/or an increase in high cloud, the net CRE change will be positive. If there is an increase in low cloud and/or a decrease in high cloud, the net CRE change will be negative.

There are minor decreases to the net CRE in the subtropical NH, larger increases in the equatorial region and over most of the SH. There is an absolute minimum (approx. 1.8 W m^{-2}) in the mean difference of net CRE around 65°S. This reduction in the net CRE is largely due to reduced sea ice around Antarctica. Figure 3.4 shows the spatial distribution of this negative CRE.

Immediately adjacent to this minimum, at around 60°S, there is an absolute maximum (2.7 W m^{-2}) in the mean difference of the net CRE. This band of increased net CRE appears due to the reduction in cloud fraction between New Zealand and South America, shown in figure 3.4. The reduction in upper-level zonal winds, seen in figure 3.6, results in changes to baroclinic instability with reduced cyclogenesis and increased anticyclogenesis in the SH.

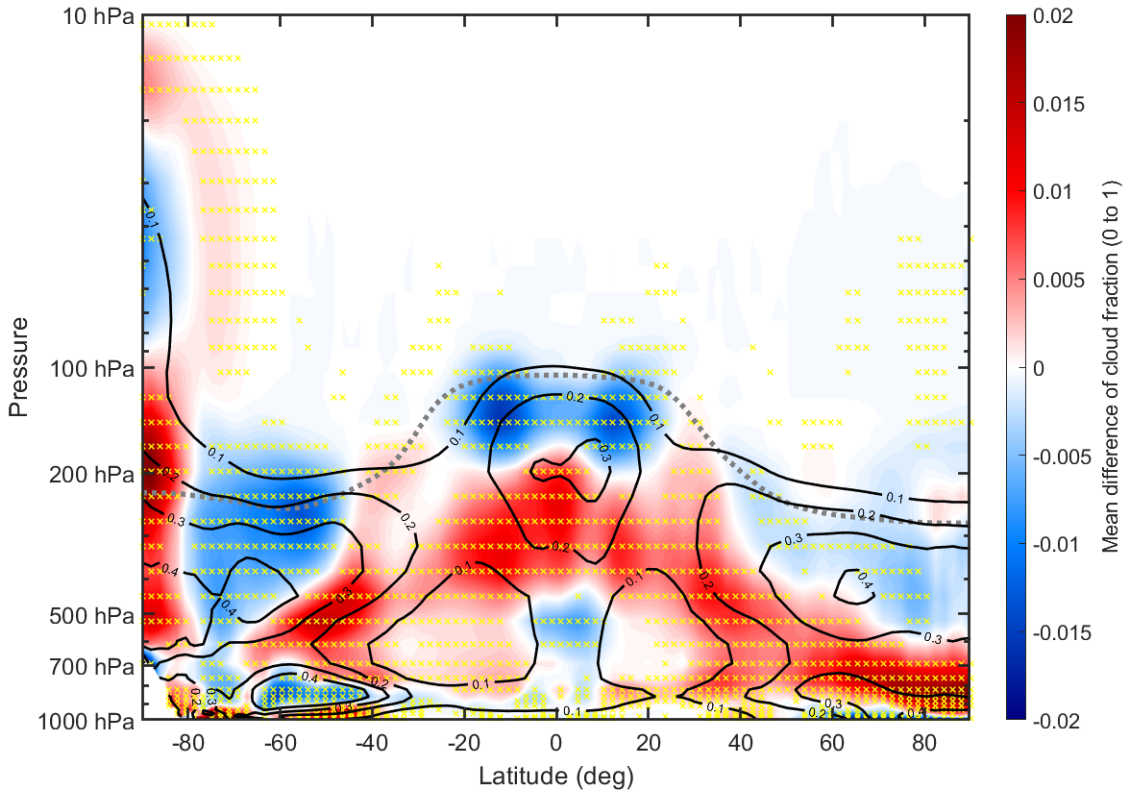

Figure 3.18: Annual mean difference (BW1850 - BWma1850) in zonal cloud fraction (0 to 1) - The black contours indicate the BWma1850 climatology of cloud fraction, with contours 0.1, 0.2, 0.3, and 0.4. Yellow dots indicates areas with statistically significant differences. The gray dotted line represents the BWma1850 climatology of the tropopause.

A secondary maximum in CRE occurs near the equator (0.9 to 1.5 W m^{-2}). This band of increased net CRE occurs around the ITCZ over the Pacific Ocean, as was shown in figure 3.4. CRE increases occur between the South pole to 75°S, 63°S to 45°S, and 38°S to 10°N. CRE decreases occur between, 75°S to 63°S, 10°N to 45°N.

Figure 3.18 is the mean difference in zonal cloud fraction. Blues indicate regions where the cloud fraction is increasing, and reds indicate regions where the cloud fraction is decreasing.

In the SPS there are minor decreases (0.005) in cloud fraction that are partially related to the reduction in PSCs due to warming in this region. That being said, there is an increase (0.02) in lower stratospheric ice cloud (not HNO_3 PSCs). This increase extends down into the troposphere.

From 80°S to 45°S between 500 hPa and 200 hPa, there is a broad region of decrease (0.005 to 0.01) in cloud fraction. This likely arised due to the changes in zonal wind, seen in figure 3.6, combined with localized tropospheric cooling.

In the lower troposphere (surface to 700 hPa), between 65°S and 40°S, there is a decrease (0.005 to 0.01) in cloud fraction. Weaker near-surface winds in this region decrease the sea salt spray into the lower troposphere (fig. 3.20). Sea salt is extremely hygroscopic, so any reductions in sea salt aerosol results in reduced clouds. This is one dynamical feedback on cloud formation.

From 45°S all the way to the North pole there are moderate increases (0.005 to 0.015) in the cloud fraction in the mid to upper troposphere. Tandon et al. (2017)

ran a simulation (with no CCN and cloud phase purely from temperature) with the opposite tropospheric (warming troposphere) temperature response seen in this experiment. This resulted in a similar structure, but with opposite sign, to what is seen in fig. 3.18. This is further evidence that much of the cloud structure is due to the localized tropospheric cooling response. Localized tropospheric cooling results in changes to circulation that modify cloud patterns.

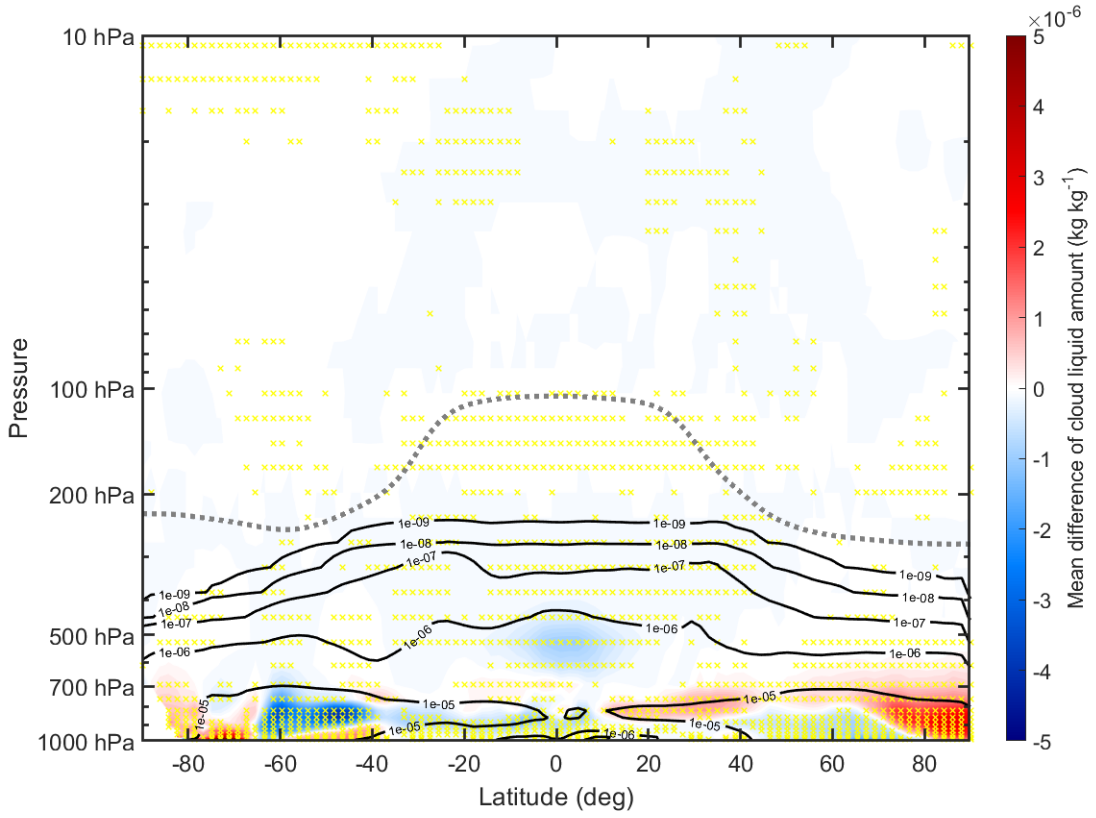

Figure 3.19: Annual difference (BW1850 - BWma1850) in cloud liquid amount (kg kg^{-1}) - The black contours indicate the BWma1850 climatology of cloud liquid, with contours 1×10^{-5}, 1×10^{-6}, 1×10^{-7}, 1×10^{-8}, and 1×10^{-9} kg kg^{-1}. Yellow dots indicate areas with statistically significant differences. The gray dotted line represents the BWma1850 climatology of the tropopause.

Referring to the changes in shortwave heating (figure 3.7e), there is a cooling influence of cloud in the Northern Hemisphere. Figure 3.19, the cloud liquid changes, also indicates an increase of cloud in the NH lower troposphere.

Figure 3.19 is the mean difference in cloud liquid amount. Blues indicate regions where cloud liquid is increasing, and reds indicate regions where cloud liquid is decreasing. Changes in cloud liquid are due to a number of factors; dynamical

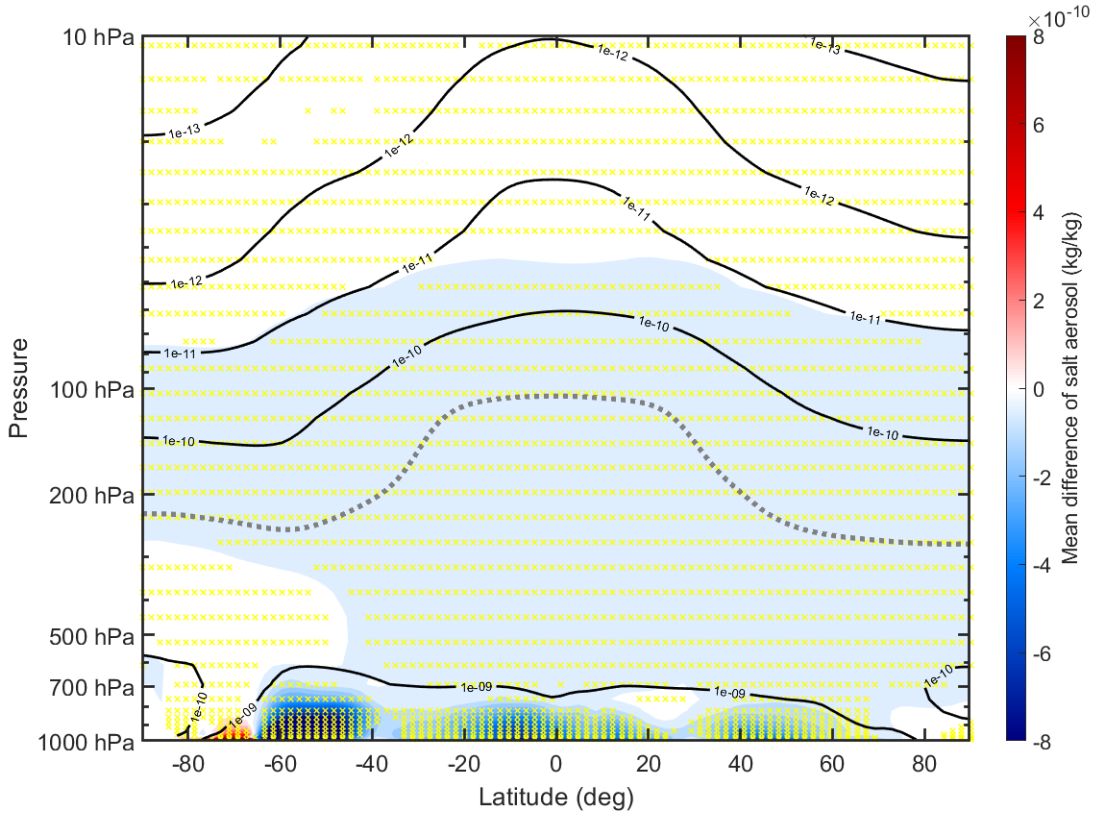

Figure 3.20: Annual mean difference (BW1850 - BWma1850) in sea salt (kg kg $^{-1}$) - The black contours indicate the BWma1850 climatology of salt aerosol, with contours 1×10^{-9}, 1×10^{-10}, 1×10^{-11}, 1×10^{-12}, and 1×10^{-13}. Yellow dots indicate areas with statistically significant differences. The gray dotted line represents the BWma1850 climatology of the tropopause.

changes, CCN changes, etc. As the changes in cloud liquid are mostly confined to the lower troposphere, the changes in cloud liquid indicate changes in low cloud's ability to reflect shortwave radiation. More cloud liquid in the lower troposphere results in more shortwave reflection back to space.

Generally, there are decreases in cloud liquid in the SH, with larger increase in the NH. The decrease (increase) in cloud liquid in the SH (NH) is associated with the positive (negative) change in CRE throughout most of the SH (NH).

Between 85°S and 65°S, there are increase in cloud liquid amount of about 2×10^{-6} to 3×10^{-6} kg kg^{-1}. The area of increase is related to figure 3.4, and the changes to sea ice. Decreases in Antarctic sea ice leads to more exposed sea surface, which increases lower tropospheric sea salt spray.

As previously shown in figure 3.18, there is a dynamical influence on the amount of sea salt aerosol that enters the lower tropopshere between 65°S and 40°S. This reduction in sea salt spray may decrease the liquid water content of clouds. Although, it is possible that the reduced baroclinicity (and increased anticyclogensis) in the SH is a driver or the primary driver of changes to liquid water amount.

Increases in cloud liquid amount in the NH may be partially due to increases in organic nitrates here (this needs further investigation). As well, these changes in cloud liquid appear to influence the total diabatic heating pattern (fig. 3.8).

Figure 3.20 is the mean difference in salt aerosol. Blues indicate regions where salt aerosol is decreasing, and reds indicate regions in which salt aerosol is increasing.

Throughout most of the troposphere salt aerosol decreases. The only region where it increases is between 85°S and 65°S. This is due to a reduction in sea ice, leading to more exposed ocean surfaces.

The largest reduction (1×10^{-8}) occurs between 65°S and 45°S in the lower troposphere. The reduced wind stress at the sea surface likely arises due to the weakened polar vortex, leading to fewer mid-latitude cyclones (due to changes in vorticity advection), which reduces the 10-m winds overall.

There is an area of increased salt aerosol over the Arctic ocean (75°N to the North Pole). It appears that this is also due to a slight reduction in sea ice in this area, due to adiabatic warming (see 3.2).

4 | Conclusions and Future Directions

4.1 Conclusions

The changes seen in this study can be summarized as follows:

- Changes in NOy (fig. 3.16), specifically organic nitrates, may influence tropospheric cooling seen in fig. 3.5. These organic nitrates are known cool the surface. Organic nitrates influence on clouds was not directly assessed in this work, and will need to be further investigated. Regardless, the inclusion of the VBS may increases the amount of organic nitrates in the atmosphere.

- There are reductions in POM (fig. 3.10) and BC (fig. 3.9) in the NH that contribute to a reduction in shortwave heating (3.7e). The reductions in POM are about -30% to -80% and reductions in BC are about -20% to -60%. The mechanism for this reduction requires further investigation, though it may be due to wet and dry deposition, or from the POM/BC aerosol being coated in another aerosol type leading to them being placed in a different aerosol bin. These changes further contribute to the hemispheric asymmetry.

- The tropospheric cooling that occurs results in equatorward shifts of the mid-latitude jets. The dynamical changes that result from these changes in the jets amplifies tropospheric cooling in some regions, while counteracting it in other regions. The overall energetic balance is between changes in longwave cooling (3.7c) and changes in dynamical heating (3.7b), qualitatively. One example of this is how poleward energy transport (PET) is weakened (in the SH) (see fig. A4), so dynamical heating must increase in the tropics at some altitudes to balance this longwave reduction. In the NH, PET is increased.

- The change in ozone in the SPS is likely a result of the dynamical warming that occurs there due to changes in the zonal wind. Zonal wind reduces (due to a localized reduction in the meridional temperature gradient in the SH), which leads to increased PVA in the SH, resulting in more descent and adiabatic warming. Ozone increases likely are not a major influence to the temperature changes seen, but are rather a consequence. This is said to highlight the fact ozone is not playing a major role in dynamics, but changes seem to be due to the temperature response. This temperature response also acts to reduce HNO_3-PSCs which further amplifies ozone in the SPS.

- The changes in SOA in the troposphere, along with NOy, seem to be the major chemical difference in the experiment. Increased production of SOA, increased production of IVOCs, and increased production of organic nitrates work to consume many radicals. This pool of radicals is then reduced, resulting in a longer

chemical lifetime for ozone. This is one reasons for elevated ozone throughout the troposphere. This reduction in radicals may also slightly influence the ozone in the stratosphere, but to a much lesser extent. It should be mentioned that reactions TR1, TR2, and TR3 (see sec. 1.8.2) is the main production pathway for tropospheric ozone. It is just that once this ozone is produced, it's lifetime is increased in the BW1850 case.

- There needs to be more investigations into the role aerosols (including SOAs and organic nitrates) are playing in cloud formation and other semi-direct and direct effects. Sulfate aerosols, seen in the appendix A10, shows a large reduction in sulfate aerosol in the tropical stratosphere. This may be playing a minor role in the energy balance, but it has not been fully assessed yet. Other parameters, such as wet deposition of aerosols, were not available for both configurations. These processes will have to be explored in future simulations.

4.2 Future work

Beyond the previously mentioned future areas of research, there is a need to see these results with human emissions. When human emissions are included in climate models a number of tropospheric chemical pathways become more productive. SOAs formed by BVOC oxidation and have significantly different chemical properties depending on the number of oxidation reactions occurring during aerosol aging. SOAs

can act as CCN or potentially inhibit cloud formation depending on hygroscopicity and meteorological conditions (Ng et al., 2017).

The same configurations of CESM2 used in this research with some key differences. Human emissions, from the National Emissions Inventory, will be implemented into two model runs of BWma1850 and BW1850 configurations. These runs will have a global resolution of 2-degrees. Once there is sufficient output from the two new configurations, global climatological parameters will be compared to locate regions where there is a statistically significant difference. These "regions of interest" will be identified for a more granular regional analysis.

In these regions of interest, a Regional-CESM (R-CESM) configuration will be run. R-CESM is a new regional modelling framework based on the CESM2 framework (Fu et al., 2021). A regional model allows smaller scale features to be represented. As an example, look at fig. 3.11 there is significantly more production of SOAs over the Amazon Forest. This occurs without significant human emissions in the model. Shrivastava et al. (2019) ran WRF-Chem simulations over the Amazon Forest nearby the Brazilian city of Manaus. Human emissions were turned on in one simulation and off in the other. When human emissions were turned on, organic aerosol production increased by 60-200 %. This simulation was on a 2-km nested grid resolution, which is necessary to capture the boundary between land types. Nested R-CESM runs over the Amazon Forest will be used to assess whether these increases in organic aerosols results in changes to the global energy budget.

Finally, in situ observations of aerosol composition in a number of these regions of interest will be performed using an Aerosol Mass Spectrometer (AMS). The AMS can differentiate the fraction of different organic fragments such as; CxHy, CxHyOz, CxHyNp, and CxHyOzNp (DeCarlo et al., 2006). AMS observations will be contrasted with 1-D column outputs from the R-CESM simulations in the regions of interest. This is to determine which components of MAM4 can be improved. Currently many climate models get their empirical SOA yields from chamber studies, which tend to underestimate SOA production due to wall losses (Shrivastava et al., 2017). More real-world observations of SOA yields could be used to improve the yield coefficients and chemical aging mechanisms implemented in the aerosol model. Improving these aerosol models will increase our ability to model future climate scenarios and their impacts on cloud formation.

Bibliography

Ackerman, A. S., Toon, O., Stevens, D., Heymsfield, A., Ramanathan, V, & Welton, E. (2000). Reduction of tropical cloudiness by soot. *Science*, *288*(5468), 1042–1047.

Albrecht, B. A. (1989). Aerosols, cloud microphysics, and fractional cloudiness. *Science*, *245*(4923), 1227–1230.

Andrews, D. G., & McIntyre, M. (1978). An exact theory of nonlinear waves on a lagrangian-mean flow. *Journal of fluid Mechanics*, *89*(4), 609–646.

Ayres, B., Allen, H., Draper, D., Brown, S., Wild, R., Jimenez, J., Day, D., Campuzano-Jost, P, Hu, W. d., De Gouw, J, et al. (2015). Organic nitrate aerosol formation via no 3+ biogenic volatile organic compounds in the southeastern united states. *Atmospheric Chemistry and Physics*, *15*(23), 13377–13392.

Bond, T. C., Bhardwaj, E., Dong, R., Jogani, R., Jung, S., Roden, C., Streets, D. G., & Trautmann, N. M. (2007). Historical emissions of black and organic carbon aerosol from energy-related combustion, 1850–2000. *Global biogeochemical cycles*, *21*(2).

Bretherton, C. S., Widmann, M., Dymnikov, V. P., Wallace, J. M., & Bladé, I. (1999). The effective number of spatial degrees of freedom of a time-varying field. *Journal of climate*, *12*(7), 1990–2009.

Brown, H., Liu, X., Feng, Y., Jiang, Y., Wu, M., Lu, Z., Wu, C., Murphy, S., & Pokhrel, R. (2018). Radiative effect and climate impacts of brown carbon with the community atmosphere model (cam5). *Atmospheric Chemistry and Physics*, *18*(24), 17745–17768.

Butchart, N. (2014). The brewer-dobson circulation. *Reviews of geophysics*, *52*(2), 157–184.

Butler, A. H., Thompson, D. W., & Heikes, R. (2010). The steady-state atmospheric circulation response to climate change–like thermal forcings in a simple general circulation model. *Journal of Climate*, *23*(13), 3474–3496.

Canadell, J. G., Le Quéré, C., Raupach, M. R., Field, C. B., Buitenhuis, E. T., Ciais, P., Conway, T. J., Gillett, N. P., Houghton, R., & Marland, G. (2007). Contributions to accelerating atmospheric co2 growth from economic activity, carbon intensity, and efficiency of natural sinks. *Proceedings of the national academy of sciences*, *104*(47), 18866–18870.

Cappa, C. D., & Wilson, K. R. (2012). Multi-generation gas-phase oxidation, equilibrium partitioning, and the formation and evolution of secondary organic aerosol. *Atmospheric Chemistry and Physics*, *12*(20), 9505–9528.

Cerully, K., Bougiatioti, A, Hite Jr, J., Guo, H, Xu, L, Ng, N., Weber, R, & Nenes, A. (2015). On the link between hygroscopicity, volatility, and oxidation state of ambient and water-soluble aerosols in the southeastern united states. *Atmospheric Chemistry and Physics*, *15*(15), 8679–8694.

Chen, G., Lu, J., & Sun, L. (2013). Delineating the eddy–zonal flow interaction in the atmospheric circulation response to climate forcing: Uniform sst warming in an idealized aquaplanet model. *Journal of the atmospheric sciences*, *70*(7), 2214–2233.

Danabasoglu, G., Lamarque, J.-F., Bacmeister, J, Bailey, D., DuVivier, A., Edwards, J., Emmons, L., Fasullo, J., Garcia, R, Gettelman, A., et al. (2020). The community earth system model version 2 (cesm2). *Journal of Advances in Modeling Earth Systems*, *12*(2), e2019MS001916.

DeCarlo, P. F., Kimmel, J. R., Trimborn, A., Northway, M. J., Jayne, J. T., Aiken, A. C., Gonin, M., Fuhrer, K., Horvath, T., Docherty, K. S., et al. (2006). Field-deployable, high-resolution, time-of-flight aerosol mass spectrometer. *Analytical chemistry*, *78*(24), 8281–8289.

Dobson, G. M. B. (1956). Origin and distribution of the polyatomic molecules in the atmosphere. *Proceedings of the Royal Society of London. Series A. Mathematical and Physical Sciences*, *236*(1205), 187–193.

Feng, Y, Ramanathan, V, & Kotamarthi, V. (2013). Brown carbon: A significant atmospheric absorber of solar radiation? *Atmospheric Chemistry and Physics*, *13*(17), 8607–8621.

Finlayson-Pitts, B. J., & Pitts Jr, J. N. (1999). *Chemistry of the upper and lower atmosphere: Theory, experiments, and applications*. Elsevier.

Finlayson-Pitts, B., & Pitts Jr, J. (1993). Atmospheric chemistry of tropospheric ozone formation: Scientific and regulatory implications. *Air & Waste*, *43*(8), 1091–1100.

Forster, P., Ramaswamy, V., Artaxo, P., Berntsen, T., Betts, R., Fahey, D. W., Haywood, J., Lean, J., Lowe, D. C., Myhre, G., et al. Changes in atmospheric constituents and in radiative forcing. chapter 2. In: *Climate change 2007. the physical science basis*. 2007.

Frierson, D. M., Held, I. M., & Zurita-Gotor, P. (2006). A gray-radiation aquaplanet moist gcm. part i: Static stability and eddy scale. *Journal of the atmospheric sciences*, *63*(10), 2548–2566.

Fry, J. L., Draper, D. C., Barsanti, K. C., Smith, J. N., Ortega, J., Winkler, P. M., Lawler, M. J., Brown, S. S., Edwards, P. M., Cohen, R. C., et al. (2014). Secondary organic aerosol formation and organic nitrate yield from no3 oxidation of biogenic hydrocarbons. *Environmental science & technology*, *48*(20), 11944–11953.

Fu, D., Small, J., Kurian, J., Liu, Y., Kauffman, B., Gopal, A., Ramachandran, S., Shang, Z., Chang, P., Danabasoglu, G., et al. (2021). Introducing the new regional community earth system model, r-cesm. *Bulletin of the American Meteorological Society*, *102*(9), E1821–E1843.

Gettelman, A, Mills, M., Kinnison, D., Garcia, R., Smith, A., Marsh, D., Tilmes, S, Vitt, F, Bardeen, C., McInerny, J, et al. (2019). The whole atmosphere community climate model version 6 (waccm6). *Journal of Geophysical Research: Atmospheres*, *124*(23), 12380–12403.

Goldstein, A., Yee, L., & Kreisberg, N. (2020). *Investigating secondary aerosol processes in the amazon through molecular-level characterization of semi-volatile organics* (tech. rep.). Univ. of California, Berkeley, CA (United States).

Guenther, A., Jiang, X., Heald, C. L., Sakulyanontvittaya, T, Duhl, T. a., Emmons, L., & Wang, X. (2012). The model of emissions of gases and aerosols from nature version 2.1 (megan2. 1): An extended and updated framework for modeling biogenic emissions. *Geoscientific Model Development*, *5*(6), 1471–1492.

Haase, S., & Matthes, K. (2019). The importance of interactive chemistry for stratosphere–troposphere coupling. *Atmospheric Chemistry and Physics*, *19*(5), 3417–3432.

Hartmann, D. L. (2015). *Global physical climatology* (Vol. 103). Newnes.

Hodzic, A., Kasibhatla, P. S., Jo, D. S., Cappa, C. D., Jimenez, J. L., Madronich, S., & Park, R. J. (2016). Rethinking the global secondary organic aerosol (soa) budget: Stronger production, faster removal, shorter lifetime. *Atmospheric Chemistry and Physics*, *16*(12), 7917–7941.

Hoesly, R. M., Smith, S. J., Feng, L., Klimont, Z., Janssens-Maenhout, G., Pitkanen, T., Seibert, J. J., Vu, L., Andres, R. J., Bolt, R. M., et al. (2018). Historical (1750–

2014) anthropogenic emissions of reactive gases and aerosols from the community emissions data system (ceds). *Geoscientific Model Development*, *11*(1), 369–408.

Holton, H. G. J., James R. (2013). *Introduction to dynamic meteorology*. Elsevier.

Höpfner, M., Luo, B. P., Massoli, P., Cairo, F., Spang, R., Snels, M., Di Donfrancesco, G., Stiller, G., Von Clarmann, T., Fischer, H., et al. (2006). Spectroscopic evidence for nat, sts, and ice in mipas infrared limb emission measurements of polar stratospheric clouds. *Atmospheric chemistry and physics*, *6*(5), 1201–1219.

Huang, H., Gu, Y., Xue, Y., Jiang, J., & Zhao, B. (2019). Assessing aerosol indirect effect on clouds and regional climate of east/south asia and west africa using ncep gfs. *Climate dynamics*, *52*(9), 5759–5774.

Hurrell, J. W., Holland, M. M., Gent, P. R., Ghan, S., Kay, J. E., Kushner, P. J., Lamarque, J.-F., Large, W. G., Lawrence, D, Lindsay, K., et al. (2013). The community earth system model: A framework for collaborative research. *Bulletin of the American Meteorological Society*, *94*(9), 1339–1360.

Kärcher, B. (2018). Formation and radiative forcing of contrail cirrus. *Nature communications*, *9*(1), 1–17.

Kasahara, A. (1974). Various vertical coordinate systems used for numerical weather prediction. *Monthly Weather Review*, *102*(7), 509–522.

Keeble, J, Braesicke, P, Abraham, N., Roscoe, H., & Pyle, J. (2014). The impact of polar stratospheric ozone loss on southern hemisphere stratospheric circulation and climate. *Atmospheric Chemistry and Physics*, *14*(24), 13705–13717.

Koch, D, & Del Genio, A. (2010). Black carbon semi-direct effects on cloud cover: Review and synthesis. *Atmospheric Chemistry and Physics*, *10*(16), 7685–7696.

Kramer, L. J., Crilley, L. R., Adams, T. J., Ball, S. M., Pope, F. D., & Bloss, W. J. (2020). Nitrous acid (hono) emissions under real-world driving conditions from vehicles in a uk road tunnel. *Atmospheric Chemistry and Physics*, *20*(9), 5231–5248.

Li, M., Karu, E., Brenninkmeijer, C., Fischer, H., Lelieveld, J., & Williams, J. (2018). Tropospheric oh and stratospheric oh and cl concentrations determined from ch4, ch3cl, and sf6 measurements. *NPJ Climate and Atmospheric Science*, *1*(1), 1–7.

Liu, H., Guo, J., Koren, I., Altaratz, O., Dagan, G., Wang, Y., Jiang, J. H., Zhai, P., & Yung, Y. L. (2019). Non-monotonic aerosol effect on precipitation in convective clouds over tropical oceans. *Scientific reports*, *9*(1), 1–7.

Liu, S., Aiken, A. C., Gorkowski, K., Dubey, M. K., Cappa, C. D., Williams, L. R., Herndon, S. C., Massoli, P., Fortner, E. C., Chhabra, P. S., et al. (2015). Enhanced light absorption by mixed source black and brown carbon particles in uk winter. *Nature communications*, *6*(1), 1–10.

Liu, X, Ma, P.-L., Wang, H, Tilmes, S, Singh, B, Easter, R., Ghan, S., & Rasch, P. (2016). Description and evaluation of a new four-mode version of the modal aerosol module (mam4) within version 5.3 of the community atmosphere model. *Geoscientific Model Development*, *9*(2), 505–522.

Liu, X., & Wang, J. (2010). How important is organic aerosol hygroscopicity to aerosol indirect forcing? *Environmental Research Letters*, *5*(4), 044010.

Mahilang, M., Deb, M. K., & Pervez, S. (2021). Biogenic secondary organic aerosols: A review on formation mechanism, analytical challenges and environmental impacts. *Chemosphere*, *262*, 127771.

Manabe, S., & Bryan, K. (1969). Climate calculations with a combined ocean-atmosphere model. *J. atmos. Sci*, *26*(4), 786–789.

Manabe, S., Bryan, K., & Spelman, M. J. (1975). A global ocean-atmosphere climate model. part i. the atmospheric circulation. *Journal of Physical Oceanography*, *5*(1), 3–29.

Meinshausen, M., Vogel, E., Nauels, A., Lorbacher, K., Meinshausen, N., Etheridge, D. M., Fraser, P. J., Montzka, S. A., Rayner, P. J., Trudinger, C. M., et al. (2017). Historical greenhouse gas concentrations for climate modelling (cmip6). *Geoscientific Model Development*, *10*(5), 2057–2116.

Menon, S., Hansen, J., Nazarenko, L., & Luo, Y. (2002). Climate effects of black carbon aerosols in china and india. *Science*, *297*(5590), 2250–2253.

Mitchell, J. F., Johns, T., Gregory, J. M., & Tett, S. (1995). Climate response to increasing levels of greenhouse gases and sulphate aerosols. *Nature*, *376*(6540), 501–504.

Molina, M. J., & Rowland, F. S. (1974). Stratospheric sink for chlorofluoromethanes: Chlorine atom-catalysed destruction of ozone. *Nature*, *249*(5460), 810–812.

Ng, N. L., Brown, S. S., Archibald, A. T., Atlas, E., Cohen, R. C., Crowley, J. N., Day, D. A., Donahue, N. M., Fry, J. L., Fuchs, H., et al. (2017). Nitrate radicals and biogenic volatile organic compounds: Oxidation, mechanisms, and organic aerosol. *Atmospheric chemistry and physics*, *17*(3), 2103–2162.

Ott, R. L., & Longnecker, M. T. (2015). *An introduction to statistical methods and data analysis*. Cengage Learning.

Penner, J. E., Zhou, C., Garnier, A., & Mitchell, D. L. (2018). Anthropogenic aerosol indirect effects in cirrus clouds. *Journal of Geophysical Research: Atmospheres*, *123*(20), 11–652.

Phillips, N. A. (1956). The general circulation of the atmosphere: A numerical experiment. *Quarterly Journal of the Royal Meteorological Society*, *82*(352), 123–164.

Pincus, R., & Baker, M. B. (1994). Effect of precipitation on the albedo susceptibility of clouds in the marine boundary layer. *Nature*, *372*(6503), 250–252.

Rhein, M., Steinfeldt, R., Kieke, D., Stendardo, I., & Yashayaev, I. (2017). Ventilation variability of labrador sea water and its impact on oxygen and anthropogenic carbon: A review. *Philosophical Transactions of the Royal Society A: Mathematical, Physical and Engineering Sciences*, *375*(2102), 20160321.

Rhew, R. C., Miller, B. R., & Weiss, R. F. (2000). Natural methyl bromide and methyl chloride emissions from coastal salt marshes. *Nature*, *403*(6767), 292–295.

Schwantes, R. H., Teng, A. P., Nguyen, T. B., Coggon, M. M., Crounse, J. D., St. Clair, J. M., Zhang, X., Schilling, K. A., Seinfeld, J. H., & Wennberg, P. O. (2015).

Isoprene no3 oxidation products from the ro2+ ho2 pathway. *The Journal of Physical Chemistry A*, *119*(40), 10158–10171.

Shrivastava, M., Andreae, M. O., Artaxo, P., Barbosa, H. M., Berg, L. K., Brito, J., Ching, J., Easter, R. C., Fan, J., Fast, J. D., et al. (2019). Urban pollution greatly enhances formation of natural aerosols over the amazon rainforest. *Nature communications*, *10*(1), 1–12.

Shrivastava, M., Cappa, C. D., Fan, J., Goldstein, A. H., Guenther, A. B., Jimenez, J. L., Kuang, C., Laskin, A., Martin, S. T., Ng, N. L., et al. (2017). Recent advances in understanding secondary organic aerosol: Implications for global climate forcing. *Reviews of Geophysics*, *55*(2), 509–559.

Song, C., Zaveri, R. A., Alexander, M. L., Thornton, J. A., Madronich, S., Ortega, J. V., Zelenyuk, A., Yu, X.-Y., Laskin, A., & Maughan, D. A. (2007). Effect of hydrophobic primary organic aerosols on secondary organic aerosol formation from ozonolysis of α-pinene. *Geophysical Research Letters*, *34*(20).

Srivastava, D., Vu, T. V., Tong, S., Shi, Z., & Harrison, R. M. (2022). Formation of secondary organic aerosols from anthropogenic precursors in laboratory studies. *npj Climate and Atmospheric Science*, *5*(1), 1–30.

Stein, T. (2021). Carbon dioxide peaks near 420 parts per million at mauna loa observatory.

Tandon, N. F., & Cane, M. A. (2017). Which way will the circulation shift in a changing climate? possible nonlinearity of extratropical cloud feedbacks. *Climate Dynamics*, *48*(11), 3759–3777.

Tritscher, I., Pitts, M. C., Poole, L. R., Alexander, S. P., Cairo, F., Chipperfield, M. P., Grooß, J.-U., Höpfner, M., Lambert, A., Luo, B., et al. (2021). Polar stratospheric clouds: Satellite observations, processes, and role in ozone depletion. *Reviews of geophysics*, *59*(2), e2020RG000702.

Twomey, S. (1974). Pollution and the planetary albedo. *Atmospheric Environment (1967)*, *8*(12), 1251–1256.

Wang, H., Easter, R. C., Zhang, R., Ma, P.-L., Singh, B., Zhang, K., Ganguly, D., Rasch, P. J., Burrows, S. M., Ghan, S. J., et al. (2020). Aerosols in the e3sm version 1: New developments and their impacts on radiative forcing. *Journal of Advances in Modeling Earth Systems*, *12*(1), e2019MS001851.

Wex, H., Stratmann, F., Topping, D., & McFiggans, G. (2008). The kelvin versus the raoult term in the köhler equation. *Journal of the Atmospheric Sciences*, *65*(12), 4004–4016.

Xie, M., Chen, X., Hays, M. D., Lewandowski, M., Offenberg, J., Kleindienst, T. E., & Holder, A. L. (2017). Light absorption of secondary organic aerosol: Composition and contribution of nitroaromatic compounds. *Environmental science & technology*, *51*(20), 11607–11616.

Xu, L., Guo, H., Boyd, C. M., Klein, M., Bougiatioti, A., Cerully, K. M., Hite, J. R., Isaacman-VanWertz, G., Kreisberg, N. M., Knote, C., et al. (2015a). Effects of anthropogenic emissions on aerosol formation from isoprene and monoterpenes in the southeastern united states. *Proceedings of the National Academy of Sciences*, *112*(1), 37–42.

Xu, L., Suresh, S., Guo, H., Weber, R. J., & Ng, N. L. (2015b). Aerosol characterization over the southeastern united states using high-resolution aerosol mass spectrometry: Spatial and seasonal variation of aerosol composition and sources with a focus on organic nitrates. *Atmospheric Chemistry and Physics*, *15*(13), 7307–7336.

Zhang, Y., Favez, O., Canonaco, F., Liu, D., Močnik, G., Amodeo, T., Sciare, J., Prévôt, A. S., Gros, V., & Albinet, A. (2018). Evidence of major secondary organic aerosol contribution to lensing effect black carbon absorption enhancement. *npj Climate and Atmospheric Science*, *1*(1), 1–8.

Zhu, J., & Penner, J. E. (2020). Indirect effects of secondary organic aerosol on cirrus clouds. *Journal of Geophysical Research: Atmospheres*, *125*(7), e2019JD032233.

Zhu, J., Penner, J. E., Lin, G., Zhou, C., Xu, L., & Zhuang, B. (2017). Mechanism of soa formation determines magnitude of radiative effects. *Proceedings of the National Academy of Sciences*, *114*(48), 12685–12690.

Ziemann, P. J., & Atkinson, R. (2012). Kinetics, products, and mechanisms of secondary organic aerosol formation. *Chemical Society Reviews*, *41*(19), 6582–6605.

5 | Appendix

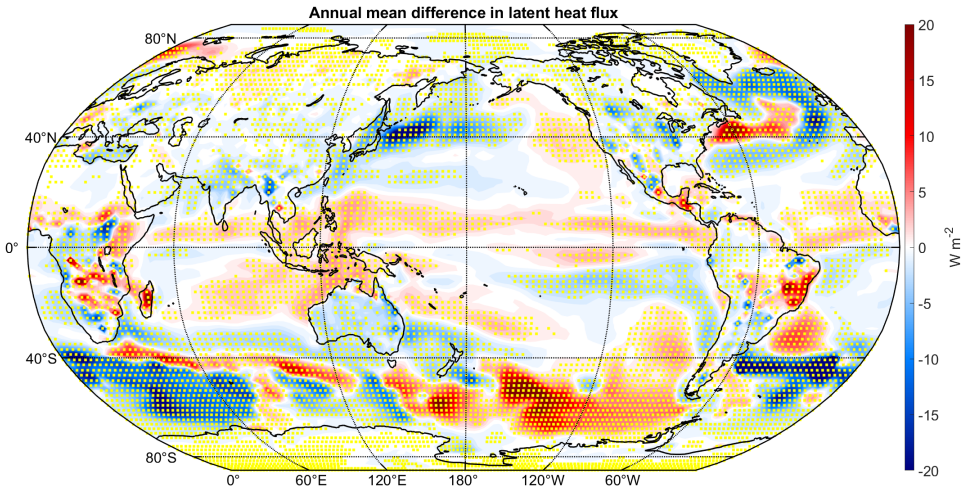

Figure A1: Annual mean difference (BW1850 - BWma1850) in latent heat flux (W m^{-2}) - Yellow dots indicate regions where there is a statistically significant mean difference.

Figure A1 is the mean difference in surface latent heat flux, with reds indicating increases in latent heat and blues indicating decreases in latent heat. Latent heat arises from the energy transfer during the phase change of a substance, with water being the main source of latent heat exchange on Earth. When water evaporates

it takes energy from the surrounding environment, cooling the environment. When water condensates it releases energy into the surrounding environment, warming the environment. Changes in latent heating indicate whether there is more or less evaporation occurring in a region.

Between 150°E and 60°W, there is an increase in latent heating south of 40°S. This is associated with fig. 3.1 where we see an increase in surface temperature here. Between 120°E moving west to 60°W, there is a decrease in latent heating south of

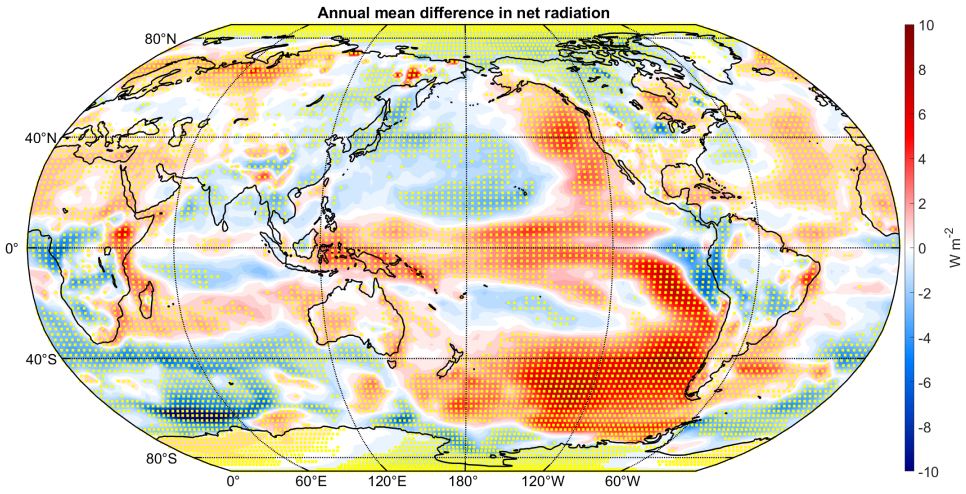

Figure A2: Annual mean difference (BW1850 - BWma1850) in TOA net radiation (W m^{-2}) - Yellow dots indicate regions where there is a statistically significant mean difference.

40°S. This is associated with fig. 3.1 where we see a decrease in surface temperature.

In the tropics generally there are increases in latent heating, with one region of decrease in latent heating between 180° longitude and 60°W.

Off the coast of Japan in the northwestern Pacific Ocean, there are decreases

in latent heating that are associated with cooler surface temperatures seen in fig. 3.1. These are also associated with increases in total cloud fraction and decreases in the net CRE, see fig. 3.4. There is a similar pattern off the coast of eastern North America.

Figure A2 is the mean difference in top of the atmosphere net radiation, with reds indicating increases and blues indicating decreases in net radiation. The net radiation is calculated by subtracting the outgoing longwave radiation at the top of the atmosphere by the absorbed shortwave radiation at the top of the atmosphere.

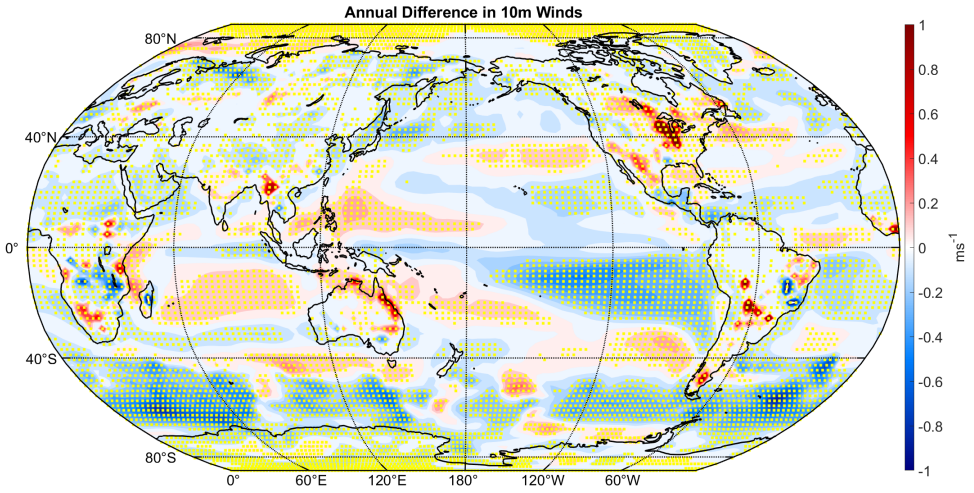

Figure A3: Annual mean difference (BW1850 - BWma1850) in 10-m winds (m s^{-1}) - Yellow dots indicate regions where there is a statistically significant mean difference.

The climatology of this quantity is described in sec. 1.5.1 by fig. 1.9.

There are increases in the net radiation between 150°E and 60°W and south of 40°S. Between 120°E moving west to 60°W, there is a decrease in net radiation south

of 40°S. In the equatorial Pacific Ocean, there are increases in net radiation, that then extend up the western North American coast. Off the coast of Japan extending to Hawaii there are decreases in net radiation. In the northern Atlantic Ocean there are increases in net radiation. Increases are also seen in Siberia, the Sahara, the USA below 40°N, Quebec, and the Madagascar region. Decreases are seen in Sub-saharan Africa, the northern Andes mountains, and the Prarie provinces of Canada.

These changes in net radiation roughly match up with changes seen in the net CRE (see fig. 3.4) over the oceans, while changes on land do not always have

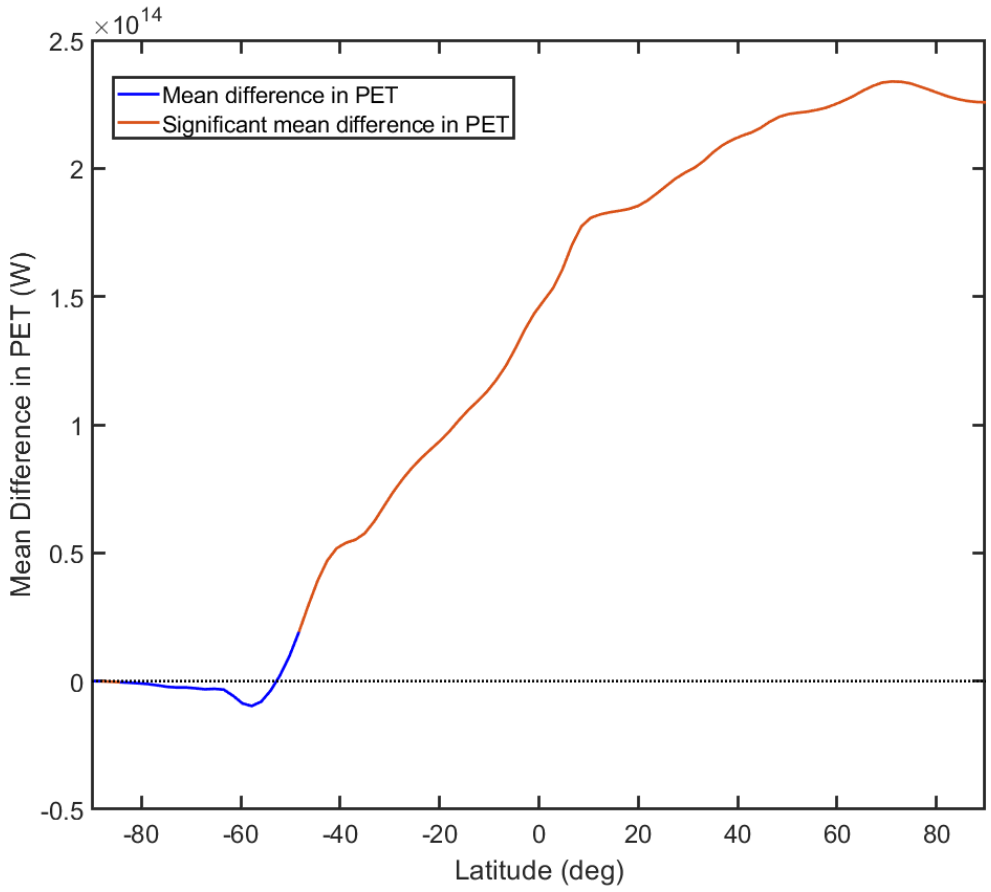

Figure A4: Annual mean difference (BW1850 - BWma1850) in poleward energy transport (PET) (Watts) - The blue indicates the mean difference in PET, while the red sections of the line are where the zonal PET is statistically significant. The gray dotted line is the zero-line.

such a correspondence.

Figure A3 is the mean difference in 10 metre winds, with reds indicating increases in 10-m winds and blues indicating decreases in 10-m winds. These change in surface winds are related to fig. 3.2 and fig. 3.6, where reductions in mid-latitude cyclones (especially in the Southern Ocean) appear to reduce surface winds.

The main point of interest in this figure is the decrease in 10-m winds

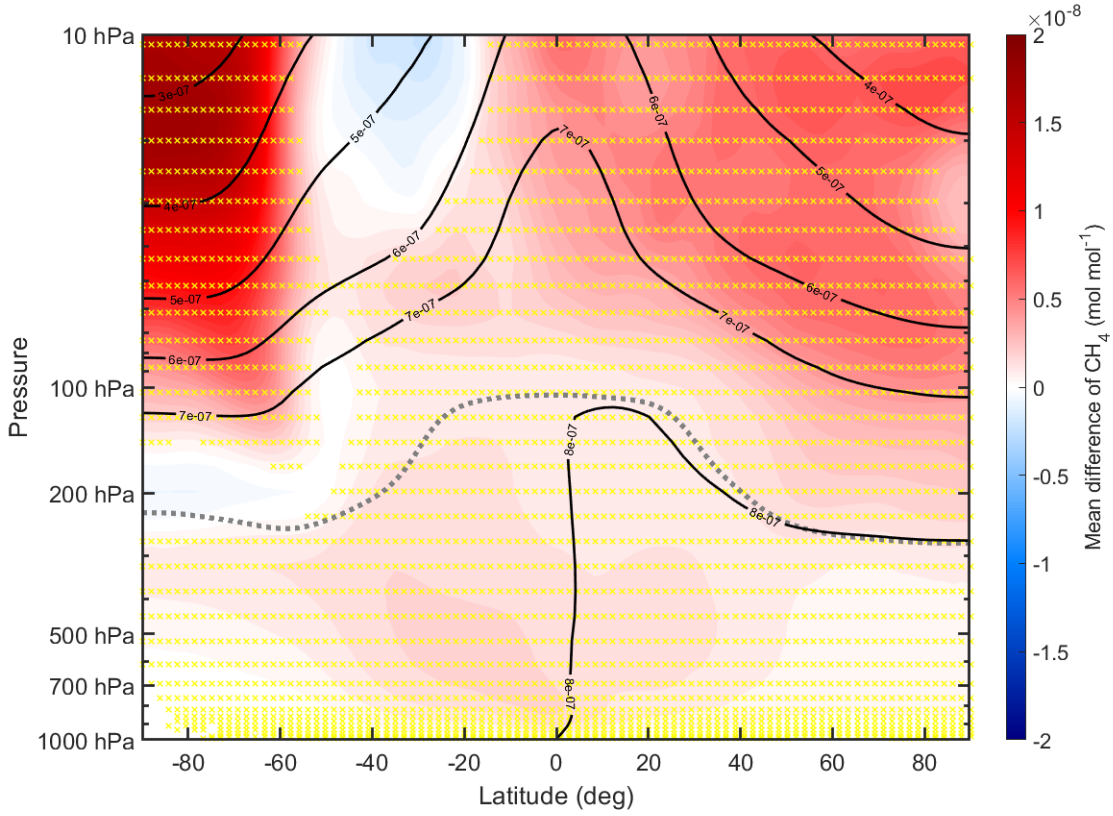

Figure A5: Annual mean difference (BW1850 - BWma1850) in CH_4 (mol mol^{-1}) - The black contours indicate the BWma1850 climatology of methane (mol $mol^{-1)}$, with a contour interval of 1×10^{-7} mol mol^{-1}. Yellow dots indicate regions where there is a statistically significant mean difference. The gray dotted line represents the BWma1850 climatology of the tropopause.

throughout the Southern Ocean. Here surface stress is lowered, which reduces the amount of sea salt spray that enters the lower troposphere (see fig. 3.20). This intern influences cloud liquid amount in this area (see fig. 3.19).

Figure A4 represents the mean difference in poleward energy transport (PET). PET was described in sec. 1.5.2, and is specifically calculated with eqn. 1.12. In the SH, negative/positive values would indicate more/less energy transport to the South

Pole. In the NH, negative/positive values would indicate less/more energy transport to the North Pole.

The changes seen in fig. A4 are related to the changes seen in fig. 3.7f (dynamical + latent heating). The positive (poleward) changes seen in the NH imply warming in the troposphere (towards the poles), which agrees with fig. 3.7f. The positive (equatorward) changes in PET in the SH suggest cooling, which corresponds to the dynamical + latent cooling seen in much of the SH troposphere.

Figure A5 represents the mean difference of methane mole fraction, with reds indicating increases in methane and blues indicating decreases in methane. Methane is about 25 times more potent than carbon dioxide as a GHG. This means changes in methane abundance can have an influence on longwave absorption in the atmosphere.

In the troposphere there are minor increases in methane that are under 0.25%. Aside from the minor, non-significant, decrease, there are increases in methane throughout the stratosphere. The largest increases are in the SPS (around 5%). The driver for changes in methane are currently being investigated.

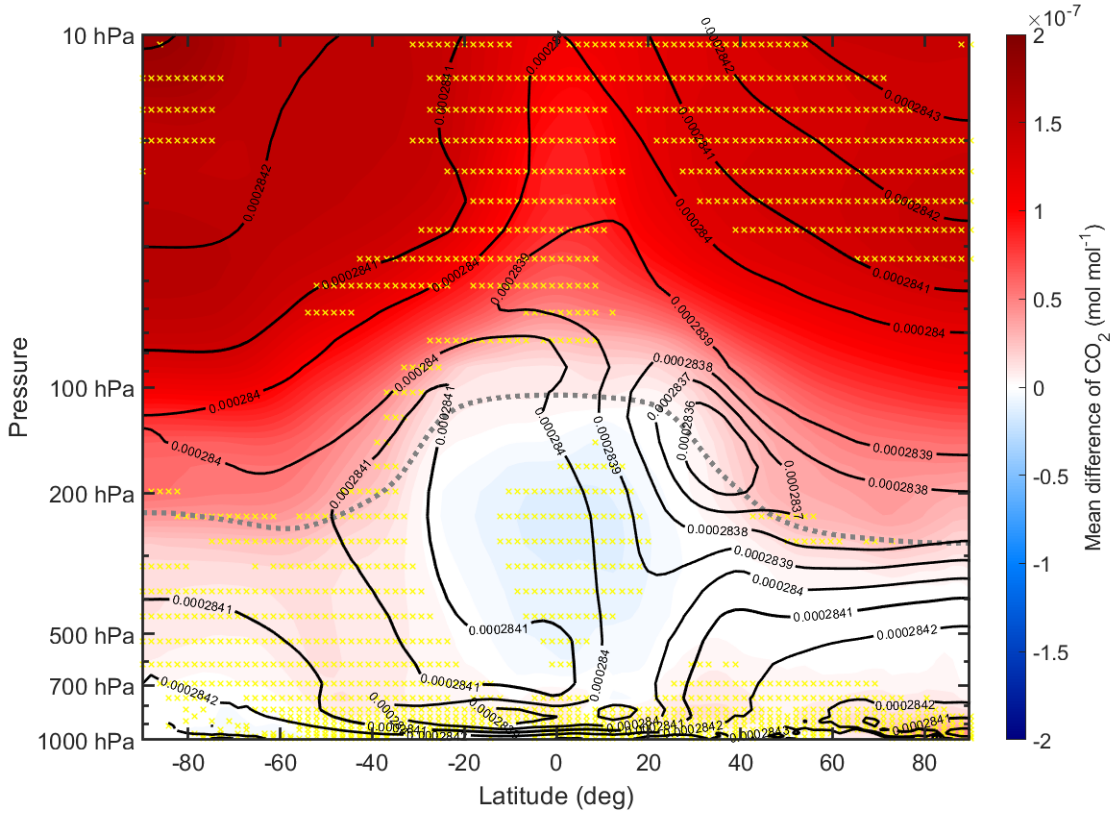

Figure A6: Annual mean difference (BW1850 - BWma1850) in CO_2 (mol mol^{-1}) - The black contours indicate the BWma1850 climatology of carbon dioxide (mol mol^{-1}), with a contour interval of 1×10^{-6} mol mol^{-1}. Yellow dots indicate regions where there is a statistically significant mean difference. The gray dotted line represents the BWma1850 climatology of the tropopause.

Figure A6 represents the mean difference of carbon dioxide mole fraction, with reds indicating increases in carbon dioxide and blues indicate decreases in carbon dioxide. Carbon dioxide is the most widely talked about GHG relating to anthropogenic emissions, and is the driver of human caused climate change. Since 1850 carbon dioxide levels have risen from 280 ppm to nearly 420 ppm by 2021. (Canadell et al., 2007; Stein, 2021)

There is a region of minor decreases in carbon dioxide in the tropical troposphere, and minor increases elsewhere in the troposphere. These changes are far under a 1 % absolute difference. In the stratosphere there are increases throughout, though the magnitude of change is still low. The changes in carbon dioxide are still being investigated.

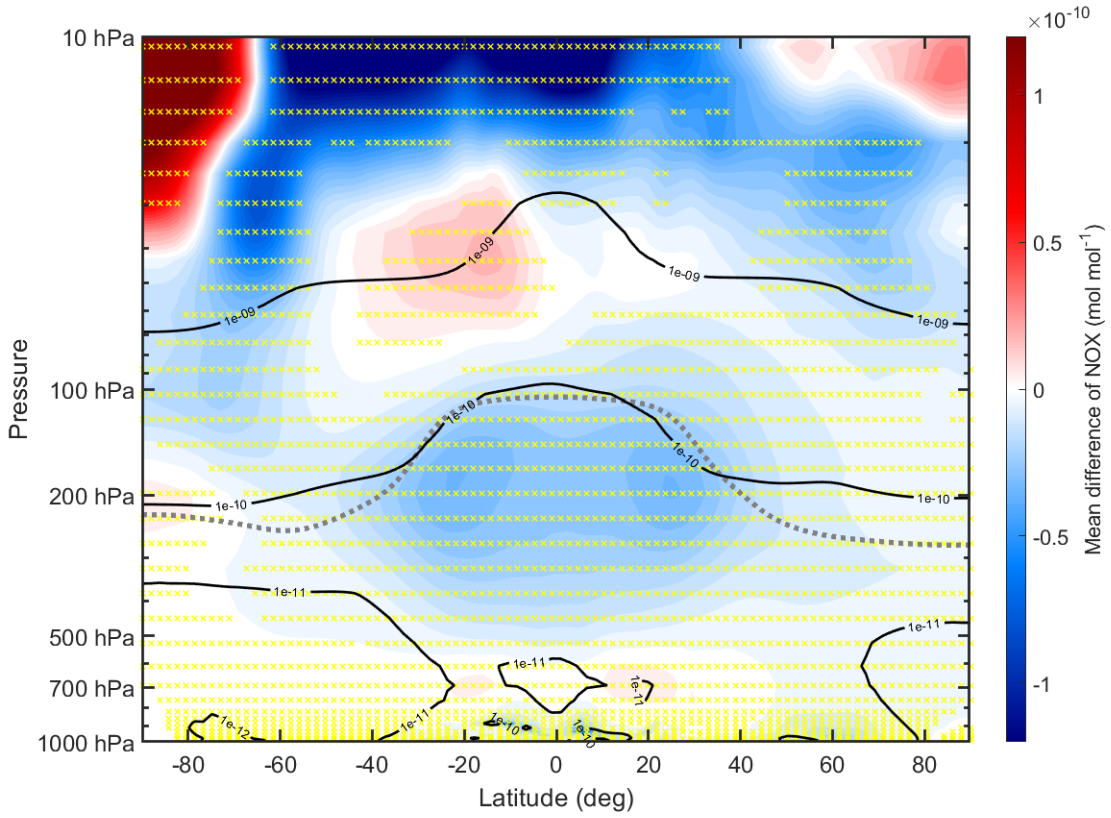

Figure A7: Annual mean difference (BW1850 - BWma1850) in NO_X (mol mol^{-1}) - The black contours indicate the BWma1850 climatology of NO_X (mol mol^{-1}), with contours of 1×10^{-12}, 1×10^{-11}, 1×10^{-10}, and 1×10^{-9} mol mol^{-1}. Yellow dots indicate regions where there is a statistically significant mean difference. The gray dotted line represents the BWma1850 climatology of the tropopause.

Figure A7 is the mean difference in NO_X, with reds indicating increase in

NO_X and blues indicating decreases in NO_X. NO_X in this context is the sum of N + NO + NO_2. Changes in NO_X are connected to a number of chemical processes in the atmosphere, including those talked about in sec. 1.9.3.

In the lower troposphere, from the South Pole to about 40°N there are minor increases in NO_X. Elsewhere in the troposphere there are decreases in NO_X, which roughly match up to the regions where SOA is increasing (see fig. 3.11). In the

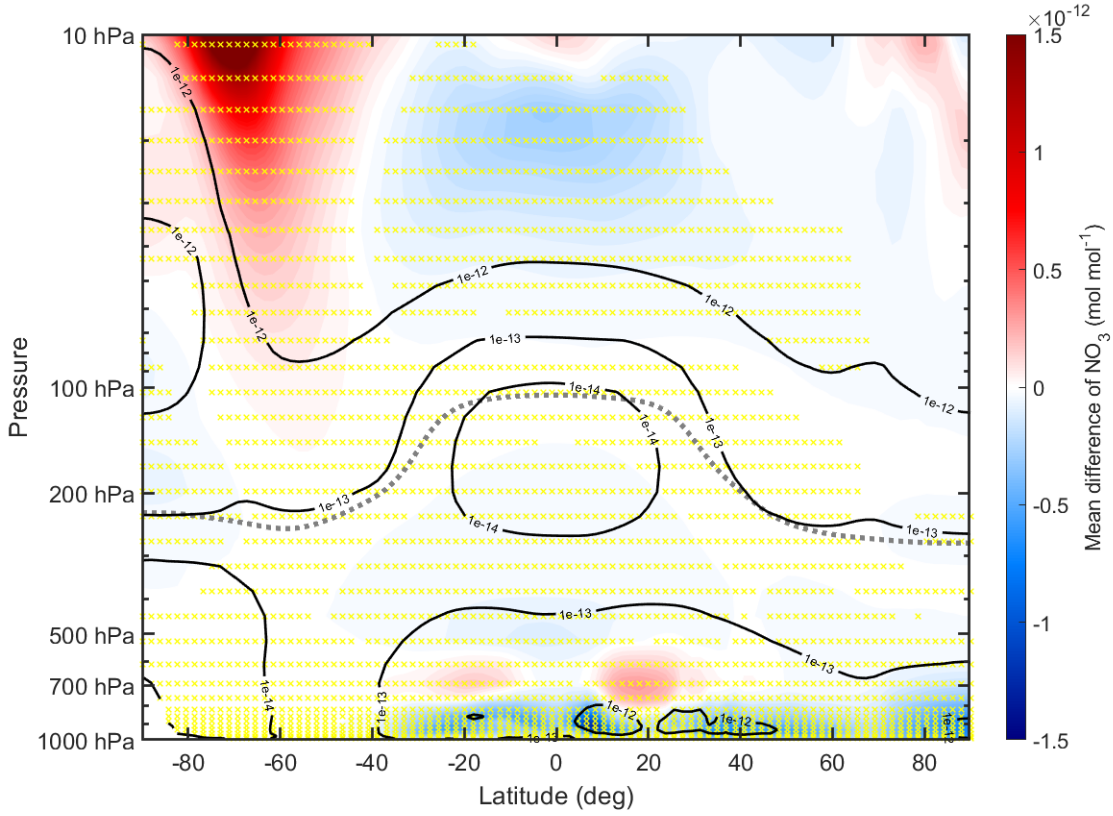

Figure A8: Annual mean difference in (BW1850 - BWma1850) NO_3 (mol mol^{-1}) - The black contours indicate the BWma1850 climatology of NO_3 (mol mol^{-1}), with contours of 1×10^{-14}, 1×10^{-13}, and 1×10^{-12} mol mol^{-1}. Yellow dots indicate regions where there is a statistically significant mean difference. The gray dotted line represents the BWma1850 climatology of the tropopause.

SPS, there are decrease in NO_X until about 30 hPa where NO_X increases significantly. Immediately to the North of this area is a region of decreased NO_X in the stratosphere. These changes to NO_X need more investigation.

Figure A8 is the mean difference in NO_3, with reds indicating increases in NO_3 and blues indicating decreases in NO_3. NO_3 is known as the nighttime radical, as opposed to hydroxyl which is most active during the day. NO_3 reactions with

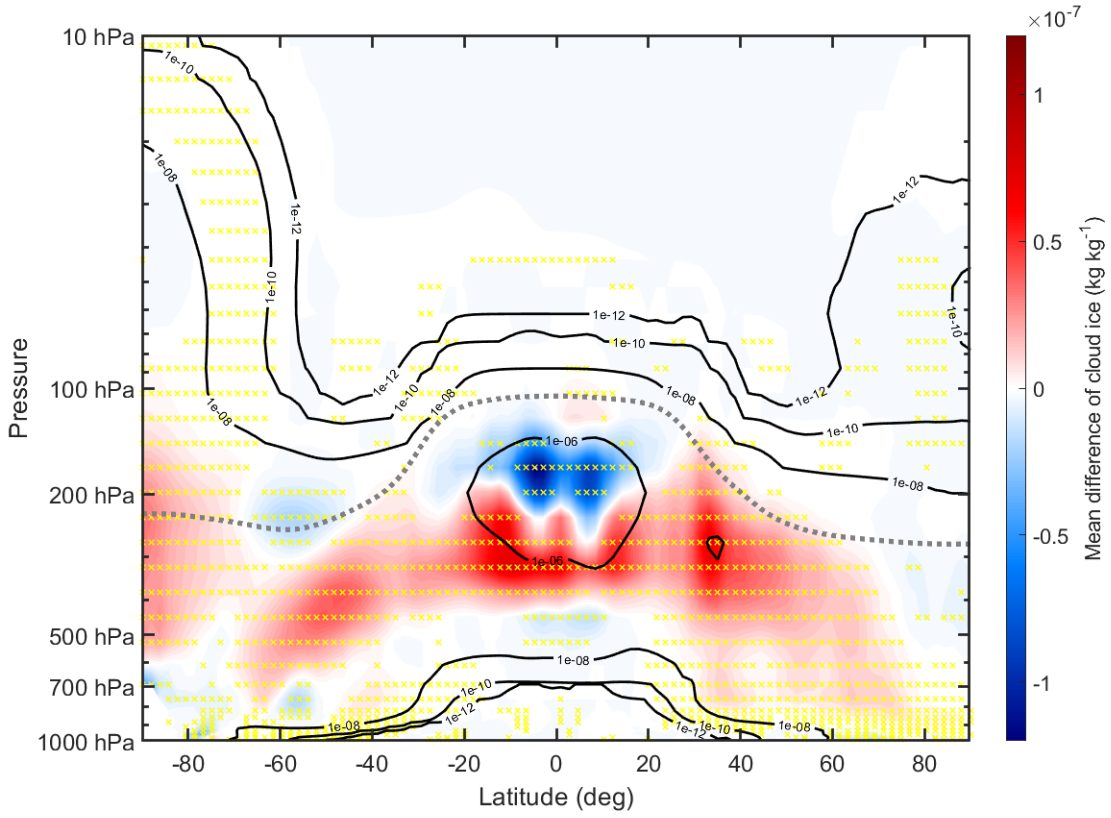

Figure A9: Annual mean difference (BW1850 - BWma1850) in cloud ice amount (kg kg^{-1}) - The black contours indicate the BWma1850 climatology of cloud ice amount (kg kg^{-1}), with contours of 1×10^{-12}, 1×10^{-10}, 1×10^{-8}, and 1×10^{-6} kg kg^{-1}. Yellow dots indicate regions where there is a statistically significant mean difference. The gray dotted line represents the BWma1850 climatology of the tropopause.

BVOCs produce SOA and organic nitrates.

In the tropical troposphere there are decreases in NO_3 that roughly line up with the increases in SOA (see fig. 3.11). As well, there are decreases in NO_3 in the lower troposphere from 40°S to the North Pole. These decreases may be associated with increases in organic nitrates.

In the SPS there is an area of increased NO_3 above 100 hPa to 10 hPa. There

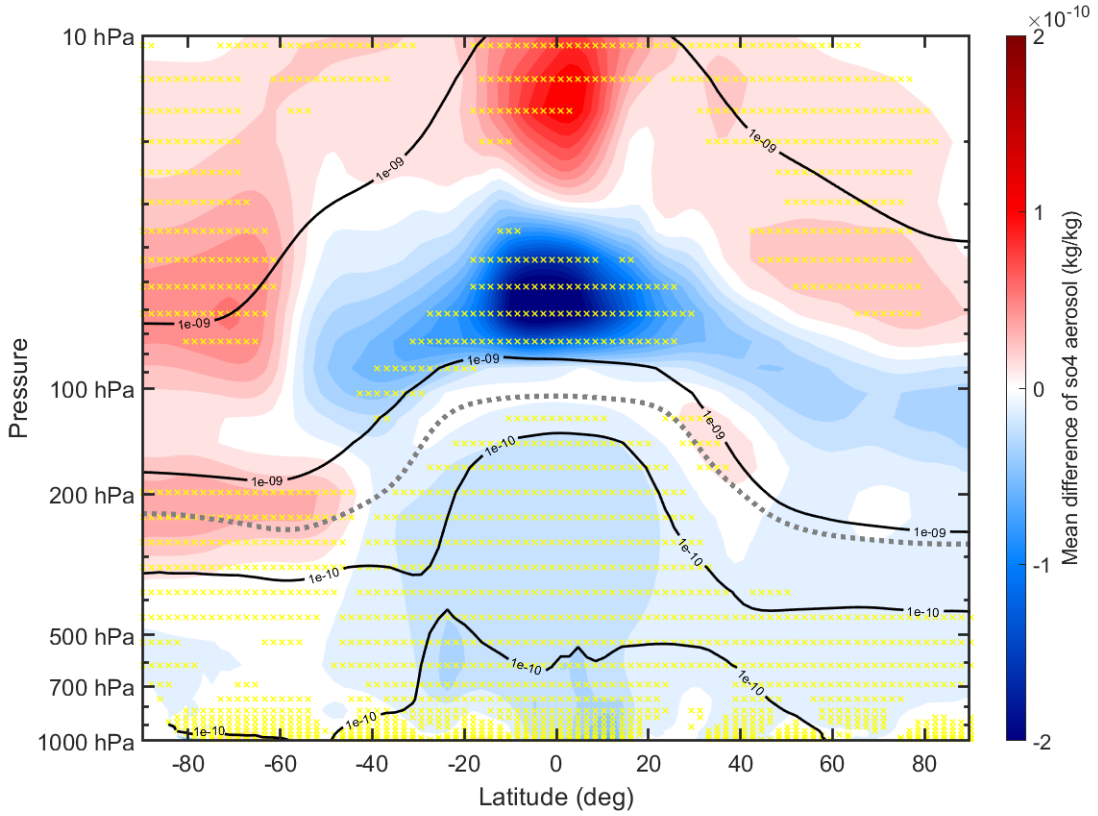

Figure A10: Annual mean difference (BW1850 - BWma1850) in sulfate aerosol (kg kg^{-1}) - The black contours indicate the BWma1850 climatology of sulfate aerosol (kg kg^{-1}), with contours of 1×10^{-10}, and 1×10^{-9} kg kg^{-1}. Yellow dots indicate regions where there is a statistically significant mean difference. The gray dotted line represents the BWma1850 climatology of the tropopause.

are decreases in NO_3 in the tropical stratosphere. These changes appear to have some correspondence to the temperature changes seen in fig. 3.5. The influences on NO_3 changes need to be further investigated.

Figure A9 represents the mean difference in cloud ice amount, with reds indicating increases in cloud ice amount and blues indicating decreases in cloud ice amount. Changes in cloud ice amount can influence how clouds scatter/absorb radiation.

Throughout the mid to upper troposphere there are increases in cloud ice amount. There is a significant region of decreased cloud ice amount in the upper tropical troposphere. The changes in cloud ice are partially attributed to the aerosol changes in the model, but need to be further investigated.

Figure A10 is the mean difference in sulfate aerosol, with reds indicating increases in sulfate aerosol and blues indicating decreases in sulfate aerosol. Increases in sulfate aerosol (primarly from volcanic eruptions and biomass burning) can lead to surface cooling, while decreases in sulfate aerosol can lead to surface warming.

It is unclear how the changes in sulfate aerosol are influencing the differences between the models. There is a reduction of sulfate aerosol in much of the troposphere. There is an increase in the SPS, and a large decrease in the tropical stratosphere. The influence of these sulfate changes on this simulation need further investigation.